STUDIES OF FUEL CELL ANODE ELECTROCATALYSIS

A Thesis

Presented to the Faculty of the Graduate School

of Cornell University

In Partial Fulfillment of the Requirements for the Degree of

Doctor of Philosophy

by

Eric Daniel Rus

August 2011

STUDIES OF FUEL CELL ANODE ELECTROCATALYSIS

Eric Daniel Rus, Ph.D.

Cornell University 2011

Several aspects of anode catalysis for proton exchange membrane fuel cells are addressed in this work, including mechanistic studies of alternative fuels, development of instrumentation for analysis of new materials, and fuel cell testing of novel materials. The electrooxidation of dimethoxymethane (DMM) at platinum was studied using differential electrochemical mass spectrometry (DEMS) and *in situ* FTIR spectroscopy. The effects of specific anion adsorption, concentration, and potential upon the product distribution were investigated. Methyl formate and CO_2 were detected as products, and the former was found to be more prevalent under all conditions tested. DEMS and FTIR measurements on ^{13}C – labeled DMM revealed that the CO_2 originated preferentially from the methyl carbons. The electrooxidation of two structurally related acetals, 1,1 – dimethoxyethane and 2,2 – dimethoxypropane was also investigated.

The development of a combined scanning DEMS – scanning electrochemical microscope (SECM) instrument is presented. This instrument will be used as a supplement to ongoing screening of combinatorial libraries of fuel cell anode catalysts, by providing spatial resolution of product formation across the composition spread.

Fuel cell testing results for a $Pt/Ti_{0.7}W_{0.3}O_2$ catalyst, of interest for CO tolerance, are described. Preliminary results for the fuel cell testing of alkaline anion exchange membrane fuel cells are also presented.

BIOGRAPHICAL SKETCH

The author grew up in Lindenhurst and Oakdale on Long Island, NY. He has been interested in electrochemistry since junior high school, when he experimented with electroplating in his spare time. He attended Connetquot High School in Bohemia, NY and graduated in the class of 2002. He was inspired to further his studies of chemistry by his AP chemistry teacher, James McConnell. He did his B.S. studies at the State University of New York at Stony Brook, and graduated in the class of 2006. There, he worked in the lab of Professor Stephen A. Koch, where he synthesized and characterized iron and ruthenium – cyanide complexes to mimic the active site of the hydrogenase enzyme. Eric attended graduate school in the Department of Chemistry and Chemical Biology at Cornell University starting in the summer of 2006, and joined the group of Professor Héctor D. Abruña later that year. He received his M.S. in January of 2009 and his Ph.D. in August 2011.

ACKNOWLEDGMENTS

First of all, I would like to thank my advisor Professor Héctor D. Abruña for giving me the opportunity to work in his lab. He has provided an environment where I could independently explore, and for his constant support, encouragement and enthusiasm. He has also brought together an extremely talented and knowledgeable research group from whom I learned a great deal. I am also grateful for the help he has given me in my job search. I would like to thank my special committee members Professor Francis J. DiSalvo and Professor Melissa A. Hines for their support and advice.

Special thanks to Dr. Hongsen Wang for getting me started in the lab. He is THE world's expert on DEMS, and taught me all of the ins and outs of running the DEMS. I also appreciate that he shared his immense knowledge of electrocatalysis with me. He has also been very good about thinking of ways out of dead ends.

Anna Legard and Michele Tague have helped with preparing and testing combinatorial samples, and John Gregoire for helping me add the emergency motor stop to the SDEMS program. Dr. Joaquín Rodríguez-López and Nicole Ritzert taught me a great deal about the preparation of ultramicroelectrodes and scanning electrochemical microscopy. I would also like to thank Nicole for her machine shop – related help, and for designing and building the three point leveling table for the scanning DEMS.

Henry A. Kostalik has been an excellent collaborator on the alkaline membrane fuel cell work. I would also like to thank him for his help in the small scale purification of the isotopically labeled dimethoxymethane. Dr. Paul Mutolo has helped us out with problems with

the fuel cell test stations several times. I would like to thank Chinmayee Subban for providing the $Pt/Ti_{0.7}W_{0.3}O_2$ samples.

I would like to thank all of the members of the lab who have provided friendship and help throughout my time at Cornell. In particular I would like to thank, Michele Tague and David Finkelstein who have been with me the whole way through. I shall miss the lab, and hope to keep in contact with those I have met here.

I would also like to thank my family for their constant moral support. I would not have made it as far as I have without them. I would also like to thank them for taking care of the pets while I have been away.

We are grateful to Dr. Allison Fisher and Motorola for the donation of a large amount of fuel cell testing equipment and materials for membrane electrode assembly preparation. This material is based upon work supported as part of the Energy Materials Center at Cornell (EMC^2), an Energy Frontier Research Center funded by the U.S. Department of Energy, Office of Science, Office of Basic Energy Sciences under Award Number DE-SC0001086. The International Precious Metals Institute also provided monetary support though the Gemini Graduate Student Award.

TABLE OF CONTENTS

CHAPTER 1

Introduction

1.1 ADVANTAGES AND CHALLENGES OF FUEL CELLS

Fuel cells hold the promise of being a highly energy efficient means of converting chemical energy directly to electrical energy. They are not limited by the Carnot cycle as heat engines are, meaning they can achieve significantly higher efficiencies. The conversion of chemical energy to electrical energy is direct, and does not require the number of moving parts a heat engine does. Possible applications for these devices are for automotive traction, portable electronics, and emergency backup power. Fuel cells offer advantages over secondary batteries in terms of not requiring long charging times, though some time is still required for refueling. Fuel cells can also offer energy densities superior to those of batteries.

It should be noted that fuel cells are not an energy source, as production of the fuel is an energy intensive process. Hydrogen can be produced by the electrolysis of water, or by reformation from organic species, such as hydrocarbons or alcohols. Organic fuels, such as methanol and dimethoxymethane are derived from natural gas. Ethanol can be produced from biomass, but this is also energy intensive process. None the less, the high efficiency and high energy density fuel cells offer, are still attractive. There are, however, materials related obstacles which must be overcome before this technology becomes practical. Several of these obstacles relate to electrocatalytic processes.

The fuel cell consists of two electrodes, the anode at which a fuel is oxidized, and the cathode at which an oxidant is reduced. The electrodes are separated by an ionically conductive but electronically insulating membrane, which is generally Nafion ®, in the case of proton exchange membrane fuel cells. The overall performance of the cell is determined by both the anode and the cathode. Ideally, the electrode reactions would reach a mass transport limited rate

at small overpotentials. In reality, these electrochemical reactions have finite kinetics. As the load placed on the fuel cell is increased, both electrodes shift their potentials, the anode more positive, and the cathode more negative, in order to drive the reactions at a higher rate, i.e. to increase the current.

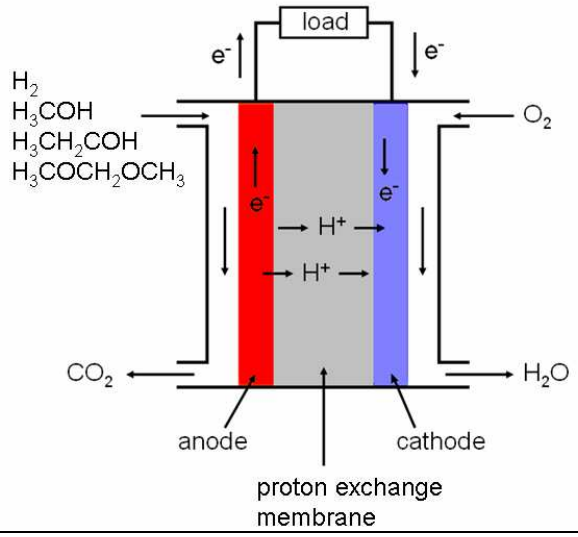

Figure 1.1: Simplified diagram of a PEM or DAFC fuel cell.

There are several types of fuel cells, including solid – oxide (SOFCs), molten – carbonate (MCFCs), phosphoric – acid (PAFCs), alkaline (AFCs), polymer electrolyte membrane (PEMFCs), and direct alcohol (DAFCs). The first three of these have primarily received attention for large scale stationary power generation.[1] The work presented in this thesis deals primarily with the last two of these, though some work with AFC membrane materials is also presented. The remainder of the introduction will refer PEM and DAFCs.

The electrooxidation of hydrogen at Pt is a relatively fast reaction, so the anode does not have to shift its potential by as a large an amount to increase its current significantly. This reaction is extremely sensitive to carbon monoxide contamination, however, and the anode must polarize to far more positive potentials to pass the same amount of current if this impurity is present. This results in a large cell voltage loss. Unfortunately, CO is a common contaminant in

H_2 feed streams produced by the steam reformation of organic precursors. Owing to the difficulties of transporting and handling large quantities of compressed H_2, reformation of organic liquids to H_2 at the point of use is often preferred.

Compared to the electrooxidation of clean H_2 at Pt, the oxygen reduction reaction (ORR) at Pt and other Pt – based catalysts, is a very slow reaction. The development of durable catalysts at which the onset of the ORR occurs at more positive potentials is currently an intense area of investigation.

In the case of direct fuel cells, which utilize small organic molecules (SOMs) without first reforming them to H_2, the kinetics of the anode reaction are slow. The thermodynamic potential of methanol, for example, is +0.017 V vs NHE, but even at the best catalyst, PtRu,[2] the onset of electrooxidation does not occur until about 0.5 V at room temperature. Even when methanol does begin to oxidize, the process can be far from complete, yielding large amounts of formic acid and formaldehyde. Ethanol and ethylene glycol have also received attention as possible fuels, but their electrooxidation tends to be even less complete than that of methanol, owing to the difficulty of breaking C – C bonds near room temperature.

While electrochemical methods yield a great deal of information about how a catalyst will perform, identification of the products of an electrochemical reaction is not necessarily straight forward. For this reason, it is useful to employ *in situ* spectroscopic techniques, which allow chemical species to be identified with little time delay between their production and detection. It is desirable to have as short a time delay as possible, so that secondary chemical or physical processes, such as hydrolysis or evaporation, are avoided. We have employed two such techniques, differential electrochemical mass spectrometry (DEMS) and *in situ* FTIR spectroscopy.

1.2 DIFFERENTIAL ELECTROCHEMICAL MASS SPECTROMETRY (DEMS)

The first *in situ* use of mass spectroscopy to track the products of electrochemical reactions was developed by Bruckenstein and Gadde.[3] In that work, the interface between the vacuum chamber and electrochemical cell consisted of a glass frit, in which Pt powder was dispersed, and was then treated with a Teflon dispersion. In that experimental setup, the chamber containing the mass spectrometer was closed off from the vacuum pump during detection, leading to accumulation of electrogenerated species in the chamber. The response of the spectrometer was, therefore, the integral of the rate of product formation, or the quantity of product formed.

The DEMS technique was developed by Wolter and Heitbaum.[4] In this setup, the mass spectrometer chamber was pumped continuously and efficiently during the measurement, making the response of the spectrometer proportional to the rate of product formation. This made the response the derivative of the integrating signal from Bruckenstein's apparatus. The term "differential" referred to this characteristic, and not to differential pumping of the vacuum chamber, as is sometimes stated. To add to the confusion, some DEMS systems are actually differentially pumped, while others, including the ones used in this work, are not. We continue to use this term to be consistent with the body of literature, but simply "electrochemical mass spectrometry" might be a better name.

In the original DEMS cell, the working electrode was prepared by painting a catalyst suspension onto a Teflon membrane to form the working electrode. In later work, the electrode was prepared by sputtering Pt onto the membrane. This cell configuration has a high collection efficiency for electrogenerated species, and a very short time delay from generation to detection. One drawback of this configuration is the passive diffusion conditions, which are subject to ill defined convective effects on the time scale of the experiment. For particularly volatile reactants,

a transport of species into the vacuum chamber can contribute to the formation of the depletion region in solution, and may do so more rapidly than the electrochemical reaction. Cells with better defined solution phase mass transport were developed in the 1990's.[5,6] Some of these were flow cells, though a rotating rod electrode DEMS cell was also developed.[7]

An interesting recent development in DEMS instrumentation is a combined DEMS – ATR – FTIR flow cell, which could be used for direct detection of solution species and surface adsorbed species under well defined mass transport conditions.[8] Another recent development is an electrospray ionization mass spectrometer coupled to an electrochemical cell, which utilized an online organic phase extraction and chemical derivatization system. It allowed for the detection of formic acid and formaldehyde, which are not readily detectable with the typical DEMS setup, due to the overlap of their fragments with other species, and their lower volatility.[9] Most recently, we have developed a dual – band electrode channel – flow DEMS cell, which can be thought of as the DEMS analog to a rotating ring – disk electrode.[10] This cell contains a second, detecting, electrode (downstream) in addition to mass spectrometric detection, and can also be used for detection of less volatile reaction products if a selective material is chosen for the detecting electrode.

Most of the DEMS work in the literature relates to fuel cell electrocatalysis, but it has also been employed in the study of nitrate reduction,[11] photoelectrochemical processes,[12,13] reactions occurring at Li-ion battery materials,[5,6] processes related to electroless deposition and electroplating,[5,14] and water oxidation.[15] The development of DEMS techniques and applications have been reviewed in detail elsewhere.[16]

1.3 *In situ* FTIR SPECTROSCOPY

While the DEMS technique has many advantages, one drawback is that it cannot directly detect electrode – adsorbed species, but only the products of their oxidation or reduction. Less volatile and more hydrophilic species can also be difficult to detect with DEMS. *In situ* FTIR spectroscopy is a complement to DEMS in that it is possible to detect some adsorbed species.

Much of the work published in the literature, and that presented in this thesis, make use of an external reflection configuration, in which a thin layer of solution is kept between the working electrode and a prism. The infrared beam passes through the solution before reflecting from the working electrode, allowing observation of both adsorbed and solution species (see chapter II). The thin layer configuration, however can be a disadvantage in terms of poor mass transport and a large cell resistance. One modification that has been used to ameliorate the former problem is the drilling of a hole through the prism, through which solution is infused, refreshing the solution in the thin layer.[17,18]

In situ FTIR spectroscopy can also be carried out using an ATR – FTIR configuration.[8,19,20] In this setup, a thin layer of metal is deposited on a high refractive index material, typically Si. This thin layer then serves as the working electrode. This setup is advantageous in terms of its sensitivity and selectivity for surface – adsorbed species and its lower cell resistance and better mass transport characteristics than the thin – layer external reflectance configuration. One disadvantage of this configuration is that it is limited to materials which are readily deposited onto Si.

Most of the electrochemical *in situ* FTIR work in the literature focuses on the adsorption and electrooxidation of CO and small organic molecules on noble metal electrodes, both out of fundamental interest and in relation to fuel cell applications. There has also been some use of *in*

situ FTIR in the area of battery related materials, particularly for the breakdown of solvents at the battery active materials.[21,22]

1.4 OVERVIEW

In the work described herein, the focus has been primarily upon electrocatalysis at the fuel cell anode. The methodology employed in this work is described in chapter II. In chapter III, a mechanistic study of dimethoxymethane electrooxidation, a promising candidate for direct use in a direct fuel cell, is reported. The effects of mass transport, anion adsorption, and fuel concentration are considered. Differential electrochemical mass spectrometry (DEMS) and *in situ* FTIR were used in identifying and quantifying the products of this reaction. In chapter IV, the relation between structure and electrochemical reactivity is investigated with two acetals structurally related to DMM.

In an effort to discover better catalysts for small organic molecule electrooxidation, we have developed a scanning DEMS system to augment our capabilities in screening combinatorial libraries for activity. Initial screening is carried out with a high throughput fluorescence assay method to rapidly identify active compositions. The SDEMS can then be used to for a more in depth analysis of active regions, allowing products to be unambiguously identified and spatially mapped. This development of this instrument is described in chapter V.

In the final three chapters, testing of materials under device operating conditions are discussed. First, general procedures in MEA preparation and testing are reviewed. Then, the testing of a CO – tolerant catalyst / support material is discussed. Finally, fuel cell testing of alkaline anion exchange membrane materials is discussed.

1.5 REFERENCES

(1) Srinivasan, S. *Fuel cells: from fundamentals to applications*; Springer: New York, NY, 2006.

(2) Wang, H.; Alden, L. R.; DiSalvo, F. J.; Abruña, H. D. *Langmuir* **2009**, *25*, 7725-7735.

(3) Bruckenstein, S.; Gadde, R. R. *Journal of the American Chemical Society* **1971**, *93*, 793-794.

(4) Wolter, O.; Heitbaum, J. *Ber. Bunsen-Ges. Phys. Chem. Chem. Phys.* **1984**, *88*, 2-6.

(5) Vaskelis, A.; Jusys, Z. *Anal. Chim. Acta* **1995**, *305*, 227-231.

(6) Jusys, Z.; Massong, H.; Baltruschat, H. *J. Electrochem. Soc.* **1999**, *146*, 1093-1098.

(7) Fujihira, M.; Noguchi, T. *J. Electroanal. Chem.* **1993**, *347*, 457-463.

(8) Heinen, M.; Chen, Y. X.; Jusys, Z.; Behm, R. J. *Electrochim. Acta* **2007**, *52*, 5634-5643.

(9) Zhao, W.; Jusys, Z.; Behm, R. J. *Anal. Chem.* **2010**, *82*, 2472-2479.

(10) Wang, H.; Rus, E.; Abruña, H. D. *Anal. Chem.* **2010**, *82*, 4319-4324.

(11) Dima, G. E.; de Vooys, A. C. A.; Koper, M. T. M. *J. Electroanal. Chem.* **2003**, *554*, 15-23.

(12) Bogdanoff, P.; Alonso-Vante, N. *Berichte der Bunsengesellschaft für physikalische Chemie* **1993**, *97*, 940-943.

(13) Bogdanoff, P.; Friebe, P.; Alonso-Vante, N. *J. Electrochem. Soc.* **1998**, *145*, 576-582.

(14) Jusys, Z.; Liaukonis, J.; Vaskelis, A. *Journal of Electroanalytical Chemistry and Interfacial Electrochemistry* **1991**, *307*, 87-97.

(15) Macounova, K.; Makarova, M.; Franc, J.; Jirkovsky, J.; Krtil, P. *Electrochem. Solid-State Lett.* **2008**, *11*, F27-F29.

(16) Baltruschat, H. *J. Am. Soc. Mass Spectrom.* **2004**, *15*, 1693-1706.

(17) Roth, J. D.; Weaver, M. J. *Journal of Electroanalytical Chemistry and Interfacial Electrochemistry* **1991**, *307*, 119-137.

(18) Paulissen, V. B.; Korzeniewski, C. *J. Electroanal. Chem.* **1993**, *351*, 329-335.

(19) Osawa, M.; Yoshii, K.; Ataka, K.-i.; Yotsuyanagi, T. *Langmuir* **1994**, *10*, 640-642.

(20) Hatta, A.; Chiba, Y.; Suëtaka, W. *Appl. Surf. Sci.* **1986**, *25*, 327-332.

(21) Imhof, R.; Novak, P. *J. Electrochem. Soc.* **1998**, *145*, 1081-1087.

(22) Novak, P.; Panitz, J. C.; Joho, F.; Lanz, M.; Imhof, R.; Coluccia, M. *J. Power Sources* **2000**, *90*, 52-58.

CHAPTER 2

Methodology

2.1 ELECTROCHEMICAL INSTRUMENTATION

2.1.1 Potentiostats

Measurements were carried out on several potentiostats. Most frequently, an EG&G PAR 173 Potentiostat / Galvanostat was utilized. An EG&G PAR 175 Universal Programmer was connected to the summing amplifier of the PAR 173 to generate potential steps and triangular waveforms for cyclic voltammetry. Also used was a Pine AFRDE5 bipotentiostat, which performed particularly well for fuel cell testing experiments. For meaurements requiring sensitivity for low currents, an Ensman Instruments EI-400 bipotentiostat was used. For rotating disk electrode (RDE) voltammetry, an AFMSRX analytical rotator was used. Data were recorded from these potentiostats via their analog outputs using LabWindows or LabVIEW software.

2.1.2 Working Electrodes: Disk Electrodes

Disk electrodes were prepared by inserting a cylinder of electrode material into the end of a hollowed out Teflon rod (ϕ = 12.5 mm). Electrical contact was made to the back side of the disk with carbon fiber wool. A stainless steel cap was then pressed into the back of the Teflon rod, and fixed in place using epoxy. These electrodes could be used for either DEMS or rotating disk electrode measurements.

In several measurements, a glassy carbon (Sigradur G, HTW Hochtemperatur-Werkstoffe GmbH) disk electrode was used to support a nanoparticle film. The glassy carbon (GC) was polished with successively finer sandpaper, and finally with ϕ = 1µm diamond paste (METADI-Buehler) on a polishing cloth with extender fluid. To functionalize the GC surface, and increase its hydrophilicity, the electrode was then sonicated in aqueous 3 M KOH for 20 minutes.

Nanoparticle inks were prepared with 8 mg of supported catalyst, 4.0 mL water, 1.0 mL isopropanol, 20 µL of Nafion (5 wt. %) solution. To ensure thorough mixing, the suspension was sonicated for 10 to 20 minutes, or until no solid remained on the bottom of the vial. A 20 µL aliquot of the suspension was then deposited on the GC disk and allowed to air dry. The Nafion in this ink served namely to make the film cohesive and adherent it to the GC surface. It may make a minor contribution to ionic conductivity in the film as well.

2.1.3 Working Electrodes: Microelectrodes

Microelectrodes were fabricated by sealing Pt wire (ϕ = 25 µm) in borosilicate glass capillary tubing. The tubing was cleaned first by sonnication in water, and then in acetone. One end of the capillary was sealed in a flame, and a 10 to 15 mm length of the Pt wire was inserted into the tubing, and knocked down to the bottom. The end of the tubing was heated in the center of a resistively heated coil of nichrome wire. The open end of the capillary was held by tubing, connected to a diaphragm pump; the vacuum helped the glass to collapse and seal on the wire more rapidly. As the glass sealed, the capillary was gradually lowered through the coil. A about 3 to 5 mm of Pt wire was left exposed in the tube. The open end of the tube was pressed into silver epoxy, and a 30 gauge insulated Cu wire was the pushed through the epoxy plug and down to contact the Pt wire. After curing the epoxy, the larger diameter wire in the back of the electrode was further secured using heat shrink tubing. The sealed end of the tube was broken off to expose the Pt wire. The end was then abraded with progressively finer grades of sandpaper.

A well sealed microelectrode should give a sigmoidal – steady state response, with low background capacitance, for a redox mediator with fast electron transfer kinetics, such as ferrocene methanol. If solution containing the redox species entered a void between the wire and

glass, the response of the redox species would resemble that of an adsorbate due to an unintentional thin layer cell configuration. For scanning electrochemical microscope tips, the end of the electrode was beveled at about a 45^{o} angle, leaving a glass sheath of about 2 to 10 times the diameter of the wire at the end of the tip.

2.1.4 The Cyclic Voltammogram of Pt

The main features in the cyclic voltammogram of Pt are the hydrogen adsorption/desorption peaks in the low potential range, and the surface oxide formation and reduction at more positive potentials (figure 2.1). The peak at about +0.125 V is associated with hydrogen adsorption on the (110) plane, while that at about +0.275 V corresponds to the (100) plane. The peak intermediate between the two, and only visible in the anodic sweep may be due to absorption of H_2 into the lattice, and is associated with the (110) plane. This peak is generally only visible when the surface is very clean. It is not visible as a distinct peak, but hydrogen adsorption on the Pt (111) plane occurs as a broad feature underlying the other peaks. The spike in reduction current at +0.05 V is due to the reduction of H^+ to H_2.

The feature beginning at about +0.88 V in the anodic sweep corresponds to the formation of Pt surface oxide, and the peak centered at about +0.82 V in the cathodic sweep corresponds to reduction of this oxide. In a clean H_2SO_4 solution, the open circuit potential of the Pt electrode is usually about +0.88 V, being determined by the formation/reduction of the surface oxide.

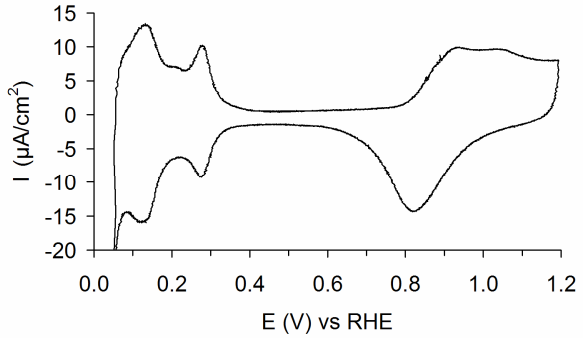

Figure 2.1: Cyclic voltammogram of a polycrystalline Pt electrode in 0.1 M H_2SO_4 at 10 mV/s. The electrode diameter was 6 mm and the roughness factor was 1.4.

2.1.5 Surface Area Normalization

A conversion factor of 210 μC/cm^2 is often used to calculate the microscopic electrochemical surface area of a Pt electrode. This is based upon the calculated surface atom densities of the three low index planes, the (111), (100), and (110), using the lattice parameter for a bulk crystal. It is expected that the low index planes will be preferentially exposed due to their lower surface energy than higher index planes. Taking the average of the charges associated with each low index plane would yield a value of 199 μC/cm^2, but a value of 210 μC/cm^2 has often been employed in the literature.[1] Some assumptions are implicit in this method. The atomic spacing at the surface may differ from that of the bulk, especially for nanoparticles. Depending upon the preparation of the electrode, certain crystal planes may be exposed preferentially, though this would be apparent in the relative heights and sharpness of the peaks in the cyclic voltammogram.

Table 2.1: Diagrams of the low index surfaces of a face centered cubic crystal. The lattice parameter of Pt was taken to be 0.392 nm.

Plane	(111)	(100)	(110)
Surface structure	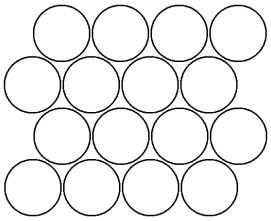	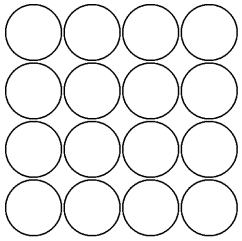	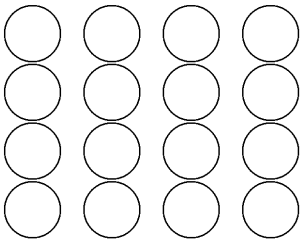
Surface atomic density (a = lattice parameter)	$\frac{4}{\sqrt{3}}\frac{1}{a^2}$	$2\frac{1}{a^2}$	$\sqrt{2}\frac{1}{a^2}$
Pt surface atom density ($x10^{15}$ atoms/cm^{-2})	1.50	1.30	0.920
Charge of a monolayer ($\mu C/cm^2$)	241	208	147
Coordination	9	8	6

It is also assumed that aside from double layer charging current, no other processes contribute to the charge passed over this potential range. It has recently been suggested that this conversion factor should be revised to 200 $\mu C/cm^2$ for $HClO_4$ solutions and 230 $\mu C/cm^2$, to take into account additional charge due to (bi)sulfate adsorption in the later case.[2]

There may also be difficulties in separating H adsorption current from H_2 evolution current at the lower end of the potential range. This can be especially problematic in cases where H_2 is actively transported away from the electrode surface. This can lower the H_2 concentration at the surface, which shifts the onset of H_2 evolution to more positive potentials via a Nernstian shift. This has been noted in CVs collected in fuel cells,[3] and in the original DEMS configuration, in which the Pt electrode is deposited directly on the membrane.[4] It has been suggested that even under passive transport conditions, a monolayer coverage is not achieved until potentials within the H_2 evolution range. This is based upon electrochemical impedance

measurements, which allowed for the separation of H adsorption and H_2 evolution currents in the overlapping range.[5]

2.1.6 Reference Electrode

The reference electrode employed most frequently in this work is the reversible hydrogen electrode (RHE). It consists of a Pt wire sealed at the top of a glass tube, containing analyte-free supporting electrolyte, and with the head space filled with H_2 gas. The RHE is charged with H_2 electrochemically prior to use, with either a battery or a power supply. Its potential generally remained stable for at least one day, though it can remain stable for several days if the rate at which H_2 leaks and rate of O_2 diffusion into the electrode are slow enough, and the solution is clean enough. The potential of the RHE is determined by the equilibrium:

$$H^+ + e^- \rightleftharpoons \tfrac{1}{2} H_2$$

It is similar to the standard hydrogen electrode (SHE), though the activities of H^+ and H_2 are not strictly maintained at unity. The potential of the RHE relates to that of the SHE as:

$$E_{RHE} = E_{SHE} - \frac{RT}{F}\ln[\frac{a_{H^+}}{(P_{H_2})^{1/2}}] \approx E_{SHE} + 0.059V \cdot pH$$

(T = 298 K)

The reference electrode was generally kept in a separate compartment, which was connected to the rest of the cell via a plastic capillary tube filled with supporting electrolyte. A stop cock prevented the solution from flowing out of the vessel, but provided sufficient ionic conductivity to connect it to the rest of the cell. This setup prevents species from the working electrode chamber from affecting the potential of the reference electrode. This setup is possible as the reference electrode draws very little current, making the ohmic drop in the capillary negligible.

2.1.7 Counter Electrodes

A coiled Pt wire was generally employed as a counter electrode. In the case of the combinatorial work, a Au counter electrode was used to avoid contamination from Pt dissolution. A graphite rod was also used in some cases to avoid contamination with catalytic metals.

2.2 DEMS

2.2.1 Vacuum System

Two DEMS systems were used over the course of this work, though only the more recent system is described in detail here (figure 2.2). All of the chamber, gauge and pump components were obtained from Pfeiffer Vacuum. The vacuum chamber was pumped by two turbomolecular pumps, a TMU 261YP at 210 L/s and TMU 071YP at 60 L/s. The effective pumping speeds were reduced by about 30% due to the use of splinter shields to protect the turbo pumps. The turbo pumps were backed by a DUO 010M rotary vane pump, at 3.3 L/s. The presence of oil vapors in the vacuum chamber were evident in spectra collected prior to connecting the chamber to the membrane inlet system, but after carrying out measurements, their presence was masked by far more prevalent residual gasses, namely H_2O.

Pressures were measured using a combined PKR 251 combined Pirani / Cold-Cathode gauge. When the chamber was closed, a pressure of 2 to 3 x 10^{-8} was routinely attained. When the chamber was opened to the membrane inlet, with water covering the membrane, the pressure was usually in the range of 0.9 x 10^{-4} mbar to 1.2 x 10^{-4} mbar. The pressures trended towards the higher range when solutions containing large amounts of highly volatile species were used. If the membrane was exposed to gas, i.e. a bubble, the chamber pressure could reach the 10^{-3} mbar range. This range is deleterious to the filament and electron multiplier, and care should be taken

to avoid extended pressure excursions. The secondary electron multiplier generally should not be used above 10^{-5} mbar, so it was generally not used.

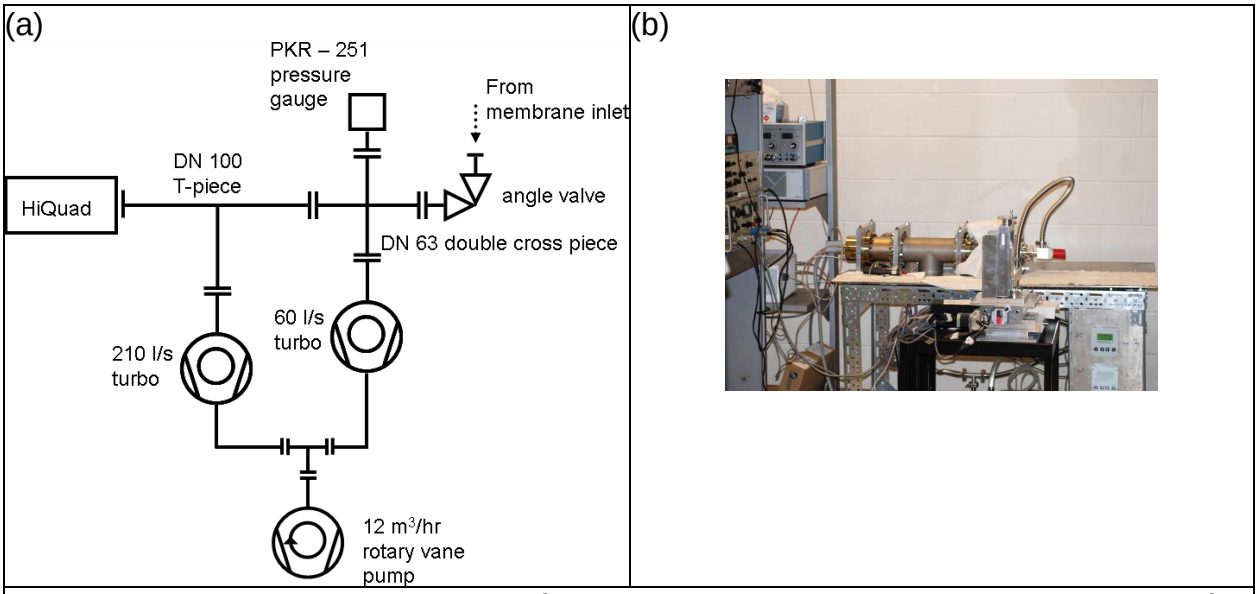

Figure 2.2: Schematic diagram of the DEMS vacuum system (a), and a photograph of the system with the scanning probe inlet attached (b).

The system utilized a Pfeiffer HiQuad QMA 410 quadrupole mass analyzer, with a mass range from 1 to 128 amu. Ionization was carried out via electron impact ionization, using a cross beam yttrium oxide – coated iridium filament, as this material is more tolerant of the relatively high O_2 and H_2O partial pressures present in the system than is tungsten. The ionization energy was set to 70 eV or 100 eV in cases where higher yields of doubly ionized CO_2 were desirable. Detection was carried out using either a Faraday cup without any amplification, or with a dynode secondary electron multiplier for amplification. The amplified signal was, of course larger, but in many cases had a signal to noise ratio inferior to that obtained without amplification. The mass spectrometer was operated through a computer, which controlled the spectrometer through the QC 700 control unit.

Mass spectrometric currents were measured via analog outputs on the QC 700. The analog outputs of the mass spectrometer and of the potentiostat were both recorded by the same

LabVIEW program (see appendix). This program also converted the mass spectrometer output voltages into currents on the fly.

2.2.2 Consistency of results between old and new DEMS

An earlier DEMS, with a Transpector 2.0 residual gas analyzer with an H100M sensor (Inficon), was also used for some experiments. This instrument did not have a convenient means of interfacing with other software, and did not have analog outputs, so it was necessary to manually match the x-axes for the electrochemical and mass spectrometric data after the measurement. A comparison of the same experiments performed on the two different instruments revealed discrepancies in terms of product ratios and the shape of the mass spectrometric cyclic voltammograms. In the case of the dimethoxymethane measurements in H_2SO_4 and $HClO_4$ solutions, covered in chapter III, the Transpector showed the onset of CO_2 production to be about 0.2 V more negative than the HiQuad. In chloride containing solutions, the Transpector also showed additional peaks (figure 2.3). In some cases, the Transpector showed several times more CO_2 being produced relative to methyl formate than the HiQuad did. The additional peaks observed in the m/z = 22 signal shown in figure 2.3c correspond to potentials at which large amounts of methyl formate (MF) were being produced. Based on a comparison with *in situ* FTIR results, it was concluded that the Transpector was not effectively filtering masses and the much larger partial pressure of MF was giving rise to a spurious CO_2 signal. It may also be that the ion source or electron multiplier was somehow converting MF to CO_2^{++}. Though it did not seem to have a significant effect on the shape of the methyl formate MSCV, it was also found that plots of methyl formate concentration vs. mass spectrometric current had a slight deviation from linearity for the Transpector, with the slope decreasing at low [MF].

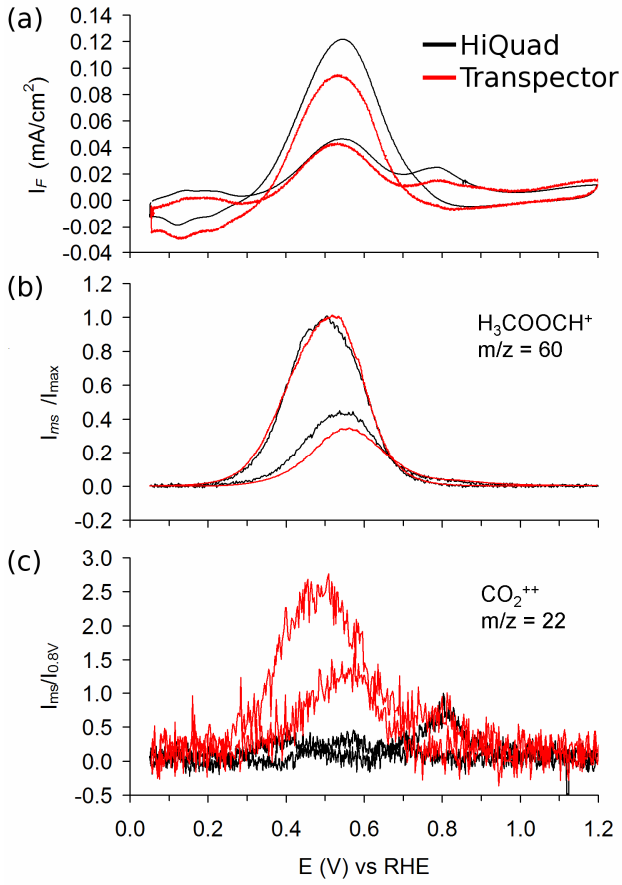

Figure 2.3: Comparison of data obtained with the HiQuad and Transpector mass spectrometers for 0.05 M DMM electrooxidation at Pt/C 50% in 0.2 M $HClO_4$ with 0.5 mM HCl. The Faradaic currents (a) are similar, though there was a higher solution O_2 concentration in the case of the measurement on the Transpector. The m/z = 60 mass spectrometric currents (b) are also quite similar, but the m/z = 22 mass spectrometric currents (c) show additional peaks at lower potentials. The currents in (b) were normalized to the maximum, but the currents in (c) were normalized to the peak at +0.8 V.

2.2.3 DEMS Flow Cell

The DEMS cell used in much of the work presented here is based upon a design originally reported by Jusys, Massong, and Baltruschat, who originally used it for a combined electrochemical quartz crystal microbalance – DEMS setup.[6] The cell consists of two compartments, connected by six capillaries in a radial arrangement (figure 2.4). There is a solution inlet at the center of the upper (working electrode) chamber, and a solution outlet at the center of the lower (membrane inlet) chamber. This cell configuration can also be used with a

second, detecting electrode in place of the membrane inlet.[7] The walls of the working electrode and membrane inlet chambers were formed by gaskets, cut from either Teflon or silicone rubber sheet, and were 0.25 mm thick prior to compression of the cell. Compression was necessary to prevent leakage, and was achieved with a metal plate on top of the working electrode, and a second below the membrane inlet, connected by threaded rods on opposite ends of the cell.

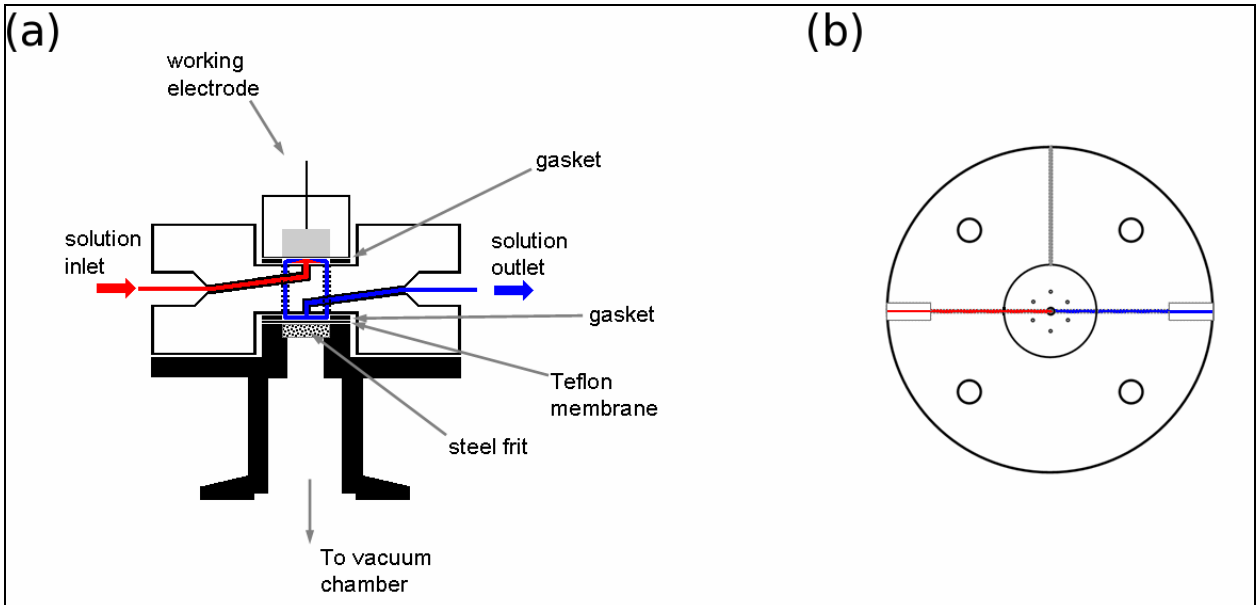

Figure 2.4: Cross sectional (a) and overhead (b) views of the DEMS flow cell used in this work. The red and blue traces indicate the flow path of the solution, with the former representing solution before it has passed over the working electrode, and the later after it has passed over the electrode.

The flow rate of the solution was controlled either by a syringe pump (model 210, KD Scientific), or using a clamp to constrict the tubing at the outlet of the cell (gravity – driven flow). Use of the syringe pump was avoided for mass transport limited systems, since the punctuated motion of its stepper motor caused oscillations in the Faradaic and mass spectrometric currents.

The rate at which a species permeates the membrane can be determined by mass transport in solution, or by transport in the membrane. For species which permeate the membrane very rapidly such as H_2, Ar, or CO_2, the response is limited by mass transport in solution. For species

which permeate the membrane slowly, such as methanol, the response is determined primarily by transport in the membrane.

The mass transport limited Faradaic current will scale as $u^{1/3}$, where u is the flow rate, for sufficiently high flow rates.[7] For a volatile species, the mass spectrometric current is also expected to scale as $u^{1/3}$,[8] though for the flow rate used for most of this work, 10 µL/s, the dependence was found to be closer to $u^{1/2}$.

2.2.4 Dual Band Electrode Channel Flow DEMS Cell

Though it was not used in the mechanistic studies described later in this work, we developed a new channel – flow DEMS cell.[9] This cell incorporates a second working electrode which can serve to amperometrically detect species generated at the first working electrode. This is advantageous, as some species, such as formic acid and formaldehyde are not readily detected mass spectrometrically. Conceptually, this can be thought of as the DEMS analogy to a rotating ring – disk electrode.

This cell consists of a rectangular channel, with two band electrodes across the floor, perpendicular to the direction of solution flow (figure 2.5). The detecting electrode lies down stream from the primary working electrode. The membrane inlet of the mass spectrometer lies between the two electrodes. The top and bottom of the cell were machined from Kel – F, and had ports for the solution inlet and outlet, the counter electrode, and the mass spectrometer inlet. The side walls of the channel were formed by a silicone rubber gasket. The counter electrode was placed directly across the channel from the working electrode to keep the cell resistance as low as possible.

The mass transport limited Faradaic current and mass spectrometric current for this cell scaled as $u^{1/3}$, as has been predicted and shown for laminar flow over a band electrode in a

rectangular channel.[10,11] Using ferrocyanaide reduction, the collection efficiency of the detecting electrode was shown to be about 20%, meaning this percentage of the ferrocyanide produced at the working electrode was reoxidized at the detecting electrode.[9] It should be noted, however, that the oxidation of small organic molecules (SOMs) is generally not mass transport limited, and the current response of the detecting electrode will not necessarily be directly proportional to the concentration of electrogenerated SOMs in solution. Furthermore, even if a selective material and potential are chosen for the detecting electrode, its response could still be complicated by the presence of other reactants and intermediates in solution. Even if these species are not oxidized at the detecting electrode potential, they can still poison it decreasing the observed current for a given concentration of analyte.

For preliminary testing of methanol and formaldehyde oxidation, nanoparticles of the ordered intermetallic PtPb were used as a formic – acid selective catalyst. This catalyst is highly active for formic acid electrooxidation,[12] and is selective for formic acid over methanol and formaldehyde in the +0.1 to +0.4V vs RHE range.

The time response of this cell is somewhat slower than the previously described flow cell owing to the larger cross sectional area of the flow path in the channel. This could be improved by using a thinner gasket, though at the expense of a higher cell resistance.

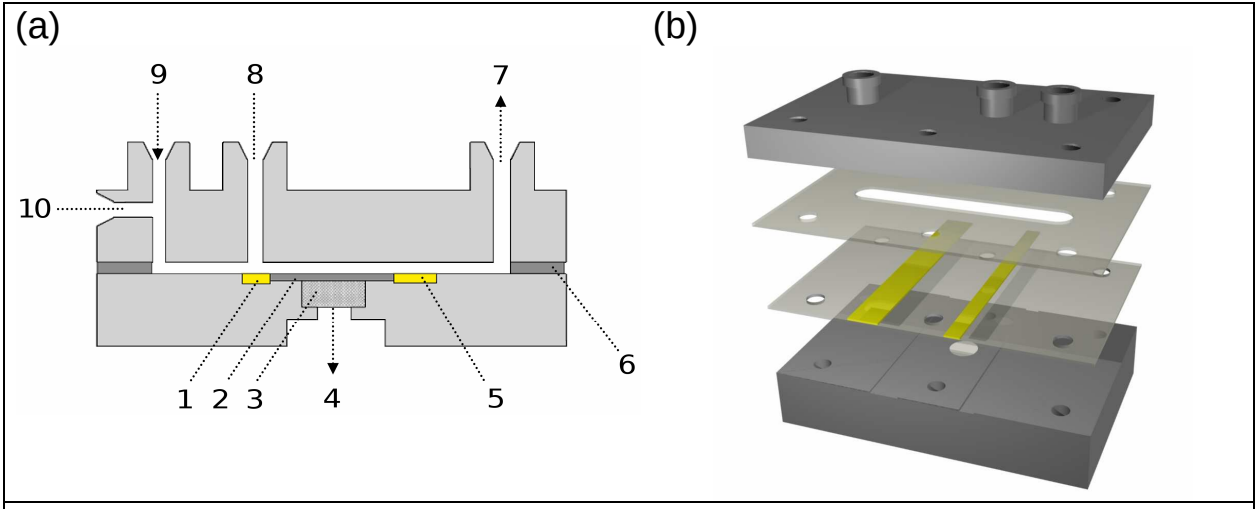

Figure 2.5: Cross section (a) and exploded (b) views of the dual band electrode channel flow DEMS cell. Labels: 1. working electrode; 2. porous Teflon membrane; 3. stainless steel frit; 4. connection to vacuum; 5. detecting electrode (PtPb/C); 6. silicone gasket; 7. solution outlet; 8. connection to counter electrode; 9. solution inlet; 10. connection to reference electrode

2.2.5 Calibration of the DEMS for Product Quantification

Data obtained with the DEMS can be made quantitative using appropriate calibration procedures. The response of the mass spectrometer varied linearly with the concentration of species in solution under the conditions tested. Calibration is carried out using electrochemical reactions involving a known number of electrons, and which are expected to produce only a single product. To calibrate for CO_2 (at m/z = 44 or 22), the stripping of adsorbed CO has often been used (figure 2.6). This method can be slightly problematic because of difficulties in integration of the peak in the Faradaic current. As the CO adlayer is stripped, there can be some additional current due to surface oxide formation and also anion adsorption, which add to the integrated charge. The benefit of this procedure is that it keeps the flow cell relatively clean. In another method of calibration for CO_2, formic acid can be used. If a slow linear potential sweep is used, the mass spectrometric current can be plotted against the Faradaic current. A straight line is obtained, the slope of which is the calibration constant (figure 2.7). The calibration constant is denoted K^* and is calculated as:

$$K^* = \frac{n \cdot Q_{ms}}{Q_F} \quad \text{or} \quad K^* = \frac{n \cdot I_{ms}}{I_F}$$

Here, n is the stoichiometric ratio of electrons to moles of CO_2 produced, which is 2 for the case of formic acid or CO oxidation to CO_2.[8,13] The mass spectrometric charge or current is given as Q_{ms} or I_{ms}, and the Faradaic charge or current is given as Q_F or I_F.

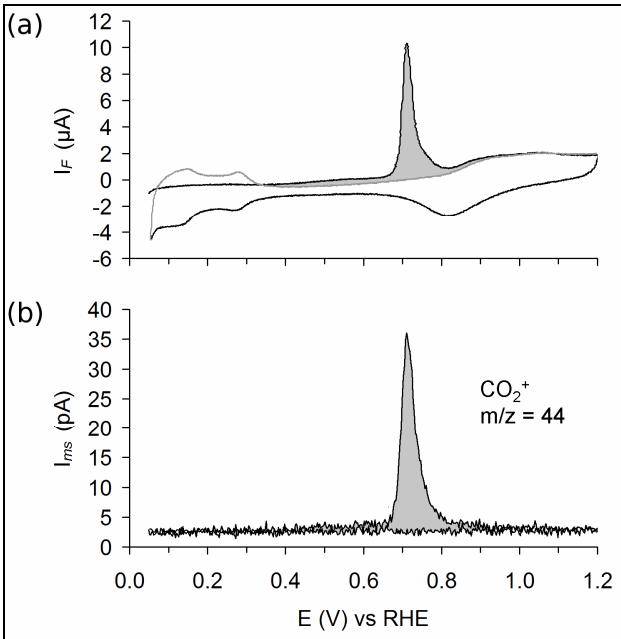

Figure 2.6: Determination of the calibration constant for CO_2^+, K^*_{44}, using the Fardaic (a) and mass spectrometric CO_2^+ (b) charges from CO stripping from a 3 mm polycrystalline Pt disk electrode. Scan rate: 10 mV/s; flow rate: 10 μL/s

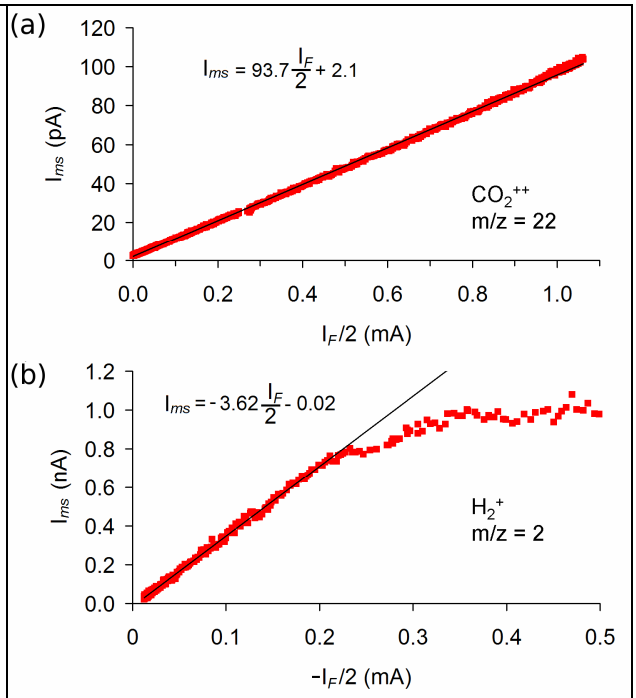

Figure 2.7: Calibration for CO_2^{++} (a) and H_2^+ (b) using a Pt/C nanoparticle film electrode. The deviation from linearity for the latter at higher currents is due to the low solubility of H_2 in water. The slope of the line is the calibration constant, K^*. Scan rate: 1 mV/s; flow rate: 10 μL/s

Another species that can be calibrated in this way is H_2, formed from the hydrogen evolution reaction. Again, it can be seen that a linear relation is obtained between the mass spectrometric current and Faradaic current. The trend becomes non linear at higher currents, likely due to excursions beyond the aqueous solubility limit of H_2. The calibration constant should be determined each time a measurement is run, as the sensitivity of the mass spectrometer

generally decreases over time due to degradation of the filament. For measurements taken during a close time period, the sensitivity is similar, and mass spectrometric currents can be compared directly. When the sensitivity of the instrument has changed significantly, the mass spectrometric current can be normalized to the calibration constant.

The calibration constant is generally used in determining the current efficiency of a process, which is denoted as A. This can be thought of as using the calibration constant to back – calculate the Faradaic current expected from the observed mass spectrometric current.

$$Q_{Fexpected} = \frac{n \cdot Q_{ms}}{K^*}$$

$$A = \frac{Q_{Fexpexted}}{Q_{Fobserved}} = \frac{\left(\frac{n \cdot Q_{ms}}{K^*}\right)}{Q_{Fobserved}} = \frac{n \cdot Q_{ms}}{K^* \cdot Q_{Fobserved}}$$

It should be noted that the value of n used in calculating A is not the same as that used for calculating K^*. It corresponds to the electron to CO_2 stoichiometric ratio for the reaction for which A is being calculated.[8,13] As an example, this would be 6 e^- per mole of CO_2 for methanol or ethanol. Current efficiency has occasionally been calculated incorrectly in the literature using the total number of electrons required for the conversion of a molecule to CO_2.

When it was not possible to exclusively generate a species electrochemically with a known number of electrons, another calibration procedure was used. To calibrate for methyl formate, for example, the relative sensitivity of the spectrometer towards methyl formate (MF) (m/z = 60) and CO_2 (m/z = 22) was determined by plotting ion current against the concentration of these species in several solutions. A CO_2 stock solution was prepared by bubbling the gas through water for at least 45 minutes, and assuming a saturation concentration of 0.037 M.[14] The relative sensitivity of the spectrometer, $K_{60/22}$, was calculated as the ratio of the slopes of these plots. For DMM oxidation, the MF to CO_2 product ratio was calculated as:

$$MF:CO_2 = \frac{Q_{ms60}}{K_{60/22} \cdot Q_{ms22}}$$

where Q_{ms60} and Q_{ms22} are the integrated mass spectrometric charges for methyl formate (MF) and CO_2. The MF calibration constant was taken to be:

$$K^*_{60} = K_{60/22} \cdot K^*_{22}$$

The MF current efficiency was then calculated as[15,16]:

$$A_{MF} = \frac{n \cdot Q_{ms60}}{K^*_{60} \cdot Q_F}$$

Calibration constants and current efficiencies calculated by this indirect method should be taken as approximate; the solution concentration profiles of the two species are expected to differ between solutions prepared directly from the analytes and those in which the species are electrochemically generated. The concentrations of electrogenerated species are likely not homogeneous throughout the solution by the time they reach the membrane inlet.

2.3 IN SITU FTIR SPECTROSCOPY

A Biorad Excalibur FTS3000 Fourier Transform infrared spectrometer with a liquid nitrogen-cooled MCT detector was used for the *in situ* FTIR measurements. The *in situ* FTIR cell utilized an external reflection configuration (figure 2.8). It consisted of a Teflon chamber with ports for the reference working and counter electrodes. The floor of the chamber was formed by a CaF_2 prism. This material was chosen due to its low solubility in aqueous solutions, the absence of absorption bands through most of the spectral range of interest, and a relatively low refractive index allowing an external reflection configuration. The infrared beam was set at a 60^o angle such that it would be normal to the prism surface, using a Pike specular reflectance accessory.

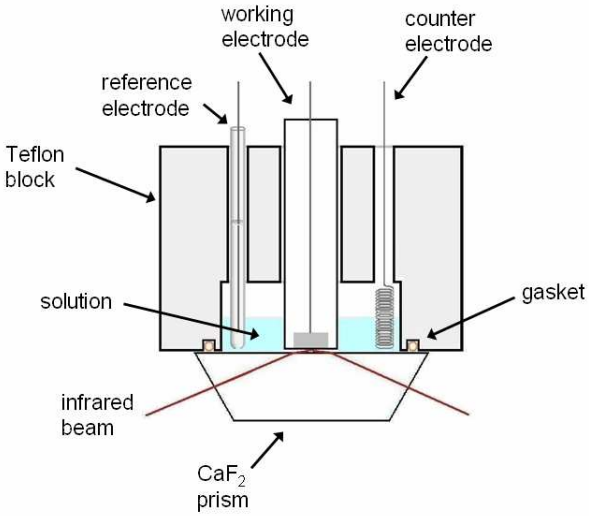

Figure 2.8: Diagram of the *in situ* FTIR spectroscopy cell.

The beam passes through the prism and the solution, reflects off of the working electrode surface, and then goes on to the detector. Hence, both species in solution and adsorbed on the electrode surface were detected. Under ideal conditions, polarized IR light would be used as this would have allowed for discrimination between solution species and surface – adsorbed species. Unfortunately, the attenuation of the IR beam was too great with the polarizer in place to make use of it.

2.4 FUEL CELL TESTING METHODOLOGY AND BENCHMARKS

2.4.1 Membrane Electrode Assembly Preparation

The Nafion 117 membrane used was pretreated by first boiling it in Millipore water for one hour, then boiling it in 3% vol H_2O_2 for one hour to remove organic impurities, and then boiled in 1 M H_2SO_4 for 1 hour to dissolve metal impurities and ensure that all of its sulfonate sites were in the acid form.[17] The as received Nafion was translucent with a brown tint, but this coloration was lost after the treatment with H_2O_2. The Nafion was stored in Millipore water prior to use. Typically, Nafion 112 (50 µm) would be used for a H_2 / O_2 fuel cell, rather than the

thicker Nafion 117 (180 µm), which is usually reserved for DMFCs. The thicker material was selected for ease of handling. A 2.25 cm x 2.25 cm (5 cm^2) serpentine flow field was used, and the Nafion was cut to a square extending approximately 1 cm beyond the active area on each side.

Membrane electrode assemblies were prepared via the catalyst coated membrane (CCM) method, as described in the "Hands – on fuel cell membrane & electrode assembly short course," at Nuvant Systems, Inc. (Crown Point, IN). Catalyst inks were prepared from 30 µL 5 wt. % Nafion solution in lower aliphatic alcohols (Sigma – Aldrich), 100 µL water, and 5 mg of catalyst (total weight, including support). This mixture was sonnicated until no catalyst remained on the bottom of the vial. The membrane was spread out on a vacuum gel drying table held at 55 to 60^{o} C. The catalyst – ionomer ink was applied to the membrane with a No. 1 red sable brush (McMaster Carr). The brush stroke direction was switched after each layer was applied to the membrane. After application of as much of the ink as possible to the membrane, it was allowed to cool to room temperature. It was then flipped, and the other catalyst layer was applied to the opposite side. The presence of Nafion in the ink is required as it provides ionic conductivity to the catalyst layer. For a catalytic site function in the fuel cell, it must have ionic conductivity with the membrane, electronic conductivity with the current collector, and must be supplied with reactants. This is known as the "triple – phase boundary."

PTFE gaskets (0.010 in., 254 µm) were cut with an open area the size of the flow field. Squares of gas diffusion layer material (ELAT GDL, LT-1400-W, ETek) were cut slightly smaller than the open area of the gasket. It was important that there be no overlap of the gasket and the GDL, as this could puncture the membrane, allowing reactant crossover. The cell was bolted together with a torque wrench in two increments, first to 30 in. lb., then 45 in lb. The six

bolts were tightened in a “star” pattern, in which consecutive bolts tightened were on opposite sides of the cell.

2.4.2 Fuel Cell Testing

Assembled fuel cells were connected to a Fuel Cell Technoologies test station, which handled gas humidification and mass flow control. It also contained a 6060B Agilent electronic load, which could operated in controlled cell voltage or current mode. It could also carry out electrochemical impedance spectroscopy (EIS) in controlled current mode. In general, galvanostatic experiments were avoided in this work, as they run the risk to taking the cell to destructive voltages if the cell cannot provide sufficient current by H_2 oxidation and O_2 reduction. It should be noted that the FCT test stations contain a National Instruments data acquisition card, which is used to measure the cell current and voltage at higher resolution and accuracy than the Agilent electronic load is able to.

For low currents, it was also possible to use a potentiostat for controlled voltage polarizations, connecting the working electrode lead to the cathode, and both the reference and counter leads to the anode. It would be possible to carry out the measurement with the connections reversed as well, but the signs of the voltages and currents would need to be reversed.

2.4.3 Electrochemical Impedance Spectroscopy (EIS)

In EIS, a small AC perturbation is applied to the electrochemical cell, and the frequency dependencies of the amplitude and phase for current and voltage are analyzed. The response of the cell is commonly modeled as a network of resistors and capacitors. For EIS measurements made in a three electrode configuration, the impedance of the counter electrode is usually made

negligible by using a counter with a much higher surface area than the working electrode. In the case of a fuel cell, anode and cathode typically have similar surface areas, so both electrodes may make significant contributions to the observed response. We have generally employed EIS only for determination of the high frequency real component of the impedance, which is the Ohmic resistance of the cell.

2.4.4 Fuel Cell Cyclic Voltammetry and CO Stripping

It is possible to obtain a cyclic voltammogram of an individual fuel cell electrode by employing a two electrode potentiostat configuration, in which one electrode acts as both the reference and counter, and the other as the working electrode. The requirement for this type of configuration is that the currents passed at the working electrode remain small enough that the potential of the reference/counter does not shift. This type of configuration is sometimes used for ultramicroelectrode measurements, in which the surface area of the working electrode is far smaller than that of the reference, and the currents passed are in the pA to nA range. The two electrode configuration is also used for Li – ion battery coin cells, in which Li metal is used as the reference/counter electrode.

In the case of fuel cells, the two electrode configuration is possible, since a fuel cell electrode with H_2 flowing over it might be able to pass currents in the 100 mA range before polarizing significantly, while the working electrode current might only be in the 10 to 100 mA range. If one desired to pass higher working electrode currents, it might be desirable to use a higher metal loading for the reference/counter. If the reference/counter does begin to shift potential from an inability to pass sufficient current, this will manifest itself as a positive shift in the anodic current features and a negative shift in cathodic current features. (It appears similar to the effects of ohmic drop.)

To configure the cell for cyclic voltammetry, H_2 at 50 to 100 sccm is used at the reference/counter, and N_2 at 10 sccm is used at the working. The low flow rate is used for the working to avoid a Nernstian shift of H_2 evolution, which could obscure the hydrogen adsorption/desorption peaks. At high flow rates, H_2 is removed from the diffusion layer, causing a Nernstian shift in H_2 evolution to more positive potentials.[3] At lower flow rates, too much H_2 accumulates in the diffusion layer, and the oxidation of electrogenerated H_2 can obscure the hydrogen desorption peaks in the anodic sweep. The preferable condition for this test is to fill the working electrode with liquid water, but the setup used for this work does not offer a facile means of accomplishing this.

Some fuel cells are prepared with a third electrode, intended to serve as a reference. It consists of a small piece of Pt wire pressed against the Nafion membrane on the anode side, outside of the active area. A number of papers have examined this type of reference, and determined it to be somewhat problematic due to its location relative to the electric fields in the cell.[18]

The setup for CO stripping is the same as that for cyclic voltammetry, but the electrode must first be dosed with CO, using CO – containing H_2, or CO diluted in N_2. For the H_2 – CO mixture, if the dosing potential is held more positive than open circuit (0 V), but below potentials at which CO begins to oxidize, the decay of the H_2 oxidation current can be taken as an indicator of the extent to which the surface is blocked. At 60 ^{o}C and 100 sccm 2% CO in H_2, about 20 to 35 minutes were necessary to cover the surface. After dosing, the electrode was then purged with N_2 for about 30 minutes to remove H_2 and free CO. (Much of the time spent purging the cell is due to the volume of the gas humidification bottles, and gasses dissolved in the water contained therein.) Under some conditions, it was difficult to maintain the CO coverage while

purging the cell. At 80°C, it appears that some CO is able to desorb, even at 0 V vs RHE. For PtRu and $Pt/Ti_{0.7}W_{0.3}O_2$ it appeared that there was some loss of CO coverage even at 60°C, possibly because desorption of CO from these materials is more rapid than from Pt.

2.4.5 Cell Polarization on a Model System

As a model or benchmark system, a fuel cell was prepared using ETek Pt/C 50% wt. at about 0.4 mg_{Pt}/cm^2 for both the anode and the cathode. These are not the conditions for an optimized fuel cell; the anode loading is relatively high, and the preferable cathode catalyst is PtCo. It has been reported that anode catalyst loadings as low as 0.05 mg_{Pt}/cm^2 are possible for CO – free H_2,[19] but preparation of an evenly dispersed catalyst layer would be very difficult with the setup and methods used here. The optimal cathode catalyst is PtCo, but for tests on already complicated anode materials, we preferred not to introduce and more elements into the cell than necessary.

The gas streams were set at approximately 100% relative humidity, which was accomplished by setting the gas humidifiers at a temperature 5° higher than the cell temperature. Generally, the gas flow rates were set to 50 sccm. Pure H_2 and pure O_2, rather than air, were used. The open circuit voltage of this cell is generally about 1.00 to 1.03 V, but is lower if there is excessive crossover of reactants. It is also lower at higher temperatures, possibly due to enhanced transport of reactants across the membrane. The cell performance is determined by both electrodes, though at these loadings, it is expected that its performance is primarily determined by the cathode.

A comparison of polarization curves at different temperatures is shown in figure 2.9a. Though the temperature increase improves the kinetics of the electrode reactions, the largest changes occur over the voltage range at which the current begins to reach is mass transport limit.

This is likely due to increases in the diffusion coefficients of H_2 and O_2 in Nafion with temperature.[20] Polarization curves with 100 ppm CO in the H_2 anode feed stream are shown in figure 2.9b. Increases in current are apparent over much of the voltage range. The increases at smaller polarizations may be due the higher rate of desorption of CO from the Pt surface at elevated temperatures. At larger polarizations, the increase is probably due to some CO electrooxidation in addition to desorption.

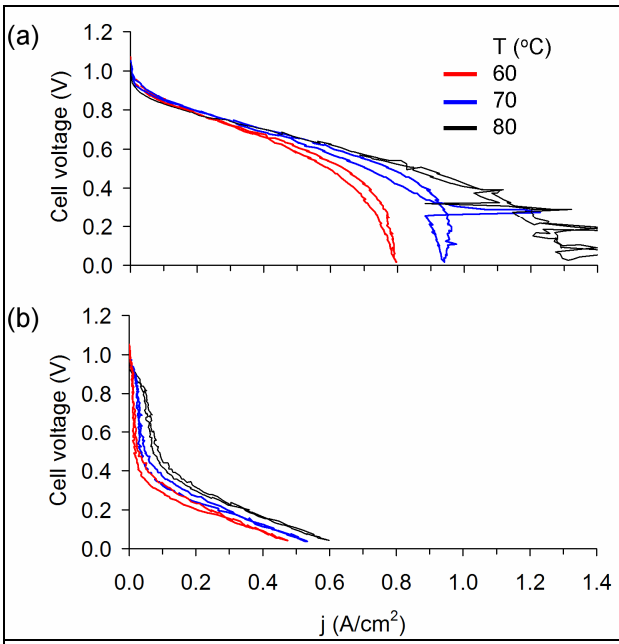

Figure 2.9: Controlled voltage polarizations for a cell prepared with 0.4 mg/cm^2 Pt/C 50% from ETek for both the anode and the cathode, at different temperatures, noted in the legend. In the data shown in (a) pure H_2 was used, while in (b), H_2 with 100 ppm CO was used. In (c), CO stripping from the anode is shown (cell operated in potentiostatic mode).

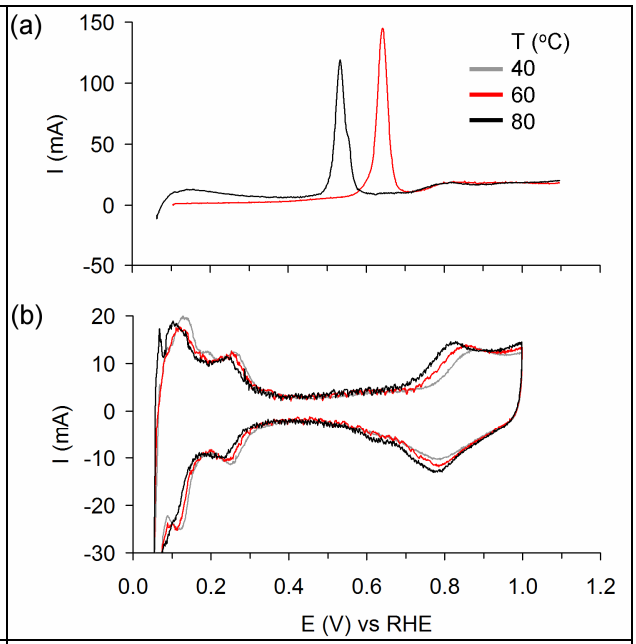

Figure 2.10: CO stripping from Pt/C 50% in the fuel cell (a), and cyclic voltammograms in the fuel cell (b) at different temperatures. (CO stripping at 40 °C not shown)

2.4.6 Cyclic Voltammetry and CO Stripping for a Model System

Examples of CO stripping voltammograms from Pt are shown in figure 2.9a. It can be seen that the peak shifts to lower potentials as the temperature increases, as would be expected.

In the cyclic voltammograms of the Pt/C electrode, there are slight changes with temperature. Some of the negative shifts may, in part, be due to shifts in the reference electrode potential with temperature. The hydrogen adsorption / desorption peaks become broader at higher temperatures, and shift closer to H_2 evolution. The surface oxide formation / reduction became slightly more reversible at higher temperatures.

2.7 REFERENCES

(1) Biegler, T.; Rand, D. A. J.; Woods, R. *Journal of Electroanalytical Chemistry and Interfacial Electrochemistry* **1971**, *29*, 269-277.

(2) Chen, Q.-S.; Solla-Gullón, J.; Sun, S.-G.; Feliu, J. M. *Electrochimica Acta*, *55*, 7982-7994.

(3) Carter, R. N.; Kocha, S. S.; Wagner, F.; Fay, M.; Gasteiger, H. A. *ECS Transactions* **2007**, *11*, 403-410.

(4) Nagel, T.; Bogolowski, N.; Samjeske, G.; Baltruschat, H. *Journal of Solid State Electrochemistry* **2003**, *7*, 614-618.

(5) Yoo, H. D.; Jang, J. H.; Ka, B. H.; Rhee, C. K.; Oh, S. M. *Langmuir* **2009**, *25*, 11947-11954.

(6) Jusys, Z.; Massong, H.; Baltruschat, H. *J. Electrochem. Soc.* **1999**, *146*, 1093-1098.

(7) Jusys, Z.; Kaiser, J.; Behm, R. J. *Electrochim. Acta* **2004**, *49*, 1297-1305.

(8) Baltruschat, H. *J. Am. Soc. Mass Spectrom.* **2004**, *15*, 1693-1706.

(9) Wang, H.; Rus, E.; Abruña, H. D. *Anal. Chem.* **2010**, *82*, 4319-4324.

(10) Elbicki, J. M.; Morgan, D. M.; Weber, S. G. *Anal. Chem.* **1984**, *56*, 978-985.

(11) Compton, R. G.; Unwin, P. R. *Journal of Electroanalytical Chemistry and Interfacial Electrochemistry* **1986**, *205*, 1-20.

(12) Casado-Rivera, E.; Volpe, D. J.; Alden, L.; Lind, C.; Downie, C.; Vázquez-Alvarez, T.; Angelo, A. C. D.; DiSalvo, F. J.; Abruña, H. D. *J. Am. Chem. Soc.* **2004**, *126*, 4043-4049.

(13) Wolter, O.; Heitbaum, J. *Ber. Bunsen-Ges. Phys. Chem. Chem. Phys.* **1984**, *88*, 2-6.

(14) Lide, D. R. *CRC Handbook of Chemistry and Physics*; 90 ed.; CRC Press (Taylor and Francis): Boca Raton, FL, 2009.

(15) Wang, H.; Alden, L.; DiSalvo, F. J.; Abruña, H. D. *Phys. Chem. Chem. Phys.* **2008**, *10*, 3739-3751.

(16) Wang, H.; Alden, L. R.; DiSalvo, F. J.; Abruña, H. D. *Langmuir* **2009**, *25*, 7725-7735.

(17) Lee, C. H.; Park, H. B.; Lee, Y. M.; Lee, R. D. *Ind. Eng. Chem. Res.* **2005**, *44*, 7617-7626.

(18) Eccarius, S.; Manurung, T.; Ziegler, C. *J. Electrochem. Soc.* **2007**, *154*, B852-B864.

(19) Gasteiger, H. A.; Panels, J. E.; Yan, S. G. *J. Power Sources* **2004**, *127*, 162-171.

(20) Parthasarathy, A.; Srinivasan, S.; Appleby, A. J.; Martin, C. R. *J. Electrochem. Soc.* **1992**, *139*, 2530-2537.

CHAPTER 3

Dimethoxymethane Electrooxidation at Platinum: A Mechanistic DEMS and *in situ* FTIR Spectroscopy Investigation*

3.1 INTRODUCTION

Dimethoxymethane (DMM) has recently been of interest as a promising alternative to methanol for direct oxidation in fuel cells, due to several attractive properties, including a high energy density and a low crossover rate.[1] Under some conditions, its electrooxidation onset potential at Pt is significantly more negative than that of methanol,[2] which is important since a direct methanol fuel cell might only have an open circuit voltage of 0.8 V.[3] Also promising is the fact that DMM is a C3 molecule with no C-C bonds. In the electrooxidation of multi-carbon fuels with C-C bonds, such as ethanol[4-6] and ethylene glycol,[7] much of the energy content is inaccessible due to the difficulty of breaking C-C bonds near room temperature.

Along these lines, the electrooxidation of several other multi-carbon compounds, also lacking C-C bonds, has been examined. Trimethoxymethane,[1,8,9] trioxane,[1] dimethyl ether,[10-12] and the polyoxymethylenedimethylether series ($CH_3O(CH_2O)_nCH_3$, n = 1 to 4)[13] have all been studied. While it is difficult to comment on the inherent activity of trimethoxymethane due to its rapid hydrolysis in aqueous solution, the others appear difficult to oxidize relative to methanol. DMM also undergoes hydrolysis in acidic solution, but it is a relatively slow reaction.

In the interest of elucidating the mechanism of DMM electrooxidation and possibly devising more effective electrocatalysts, several fundamental studies have been carried out. Miki et al. used an ATR-SEIRAS setup to study the adsorbed species formed during this reaction, and observed signals attributed to linear and bridge-bound CO, and also formate.[14] Kéranguéven et

* The content presented in this chapter is adapted in large part from: "A Mechanistic Differential Electrochemical Mass Spectrometry (DEMS) and in situ Fourier Transform Infrared Investigation of Dimethoxymethane Electrooxidation at Platinum"; Rus, E. D.; Wang, H.; Wang, D.; Abruña, H. D. *J. Phys. Chem. C* **2011**, doi: 10.1021/jp1120405

al. studied DMM oxidation at polycrystalline Pt, varying several parameters, including the scan rate in cyclic voltammetry, the presence of specifically adsorbing anions (including chloride and (bi)sulfate) and DMM concentration.[2] They also investigated DMM electrooxidation at the low index crystal planes of single crystal Pt using cyclic voltammetry, and found that the Pt (111) plane was the most active of the low index planes, both in terms of peak current and electrooxidation onset potential. With *in situ* FTIR spectroscopy, linear-bound CO was observed on the (100) and (110) planes, but not on the (111) plane.[15]

Most recently, Zhou et al. investigated the platinum – DMM system using *in situ* FTIR spectroscopy in an external reflection configuration. Aside from the species found in earlier studies, methyl formate (MF) was recognized as a major oxidation product. Based upon quantification of DMM consumption and product formation, a mechanism was proposed in which DMM is first oxidized at its central carbon to produce methanol and MF. In the potential region below approximately +0.55 V vs RHE, neither of these species is readily oxidized, so they accumulate in solution. At more positive potentials, the rate of methanol oxidation increases drastically, but MF oxidation is still slow, so MF and CO_2 accumulate.[16]

Herein, we report a study of DMM oxidation at carbon-supported Pt nanoparticles employing rotating disk electrode voltammetry, differential electrochemical mass spectrometry (DEMS) and *in situ* FTIR. The effects of solution convection, specific anion adsorption and of DMM concentration were investigated, and the MF and CO_2 produced were quantified. This work more closely approximates fuel cell conditions than some earlier fundamental studies in that a nanoparticulate catalyst was used under continuous flow conditions. DEMS and *in situ* FTIR measurements on an isotopically labeled DMM sample ($H_3{}^{13}COCH_2O{}^{13}CH_3$) are also reported, allowing carbon atoms to be traced from reactant to products.

3.2 EXPERIMENTAL METHODS

3.2.1 Reagents

Dimethoxymethane (reagent plus, 99%) was obtained from Sigma-Aldrich, and its freedom from methanol contamination was confirmed by its infrared spectrum. Formic acid (ACS grade) and hydrochloric acid (ACS reagent grade) were obtained from Mallinckrodt Chemicals. Extra pure sulfuric acid (99.999%), redistilled perchloric acid (99.999%), and Nafion 5% wt. solution in alcohols with 15-20% water were obtained from Sigma-Aldrich. Isotopically labeled methanol (^{13}C, 99%) was obtained from Cambridge Isotope Laboratories, Inc. and paraformaldehyde (95%) was obtained from Fluka. All solutions were made using ultra-pure water (18 MΩ cm), prepared with a Millipore Milli-Q Water System, and were deaerated with high purity argon (Airgas) prior to measurements. In order to avoid significant hydolysis and evaporation of the analyte, DMM and MF were added to the deaerated solutions immediately prior to beginning measurements. All measurements were carried out at 21 ± 1 ^{o}C.

3.2.2 DEMS Measurements

The apparatus and calibration procedures used in this work are described in detail in the methods chapter. An electron impact energy of 100 eV was used for ionization and a Faraday cup was used for ion detection. Formic acid (0.05 M) electrooxidation was used for calibration, as the only expected product is CO_2. Doubly ionized CO_2 was used in preference to the singly ionized form, as DMM significantly increased the m/z = 44 baseline. While DMM also contributed to the m/z = 22 baseline, the signal to baseline ratio was larger than for m/z = 44. It was not possible to track the production of methanol mass spectrometrically, due to the overlap of its peaks with those of MF and DMM.

3.2.3 Working Electrode preparation

A glassy carbon disk electrode (ϕ = 6 mm) was used for the DEMS and RDE measurements. A catalyst ink was prepared with platinum nanoparticles (~3 nm) supported on Vulcan XC-72 carbon with a 50% catalyst weight loading, obtained from E-TEK. Preparation of the GC electrode and ink are detailed in the methodology chapter. A 20 µL aliquot of the nanoparticle suspension was deposited on the GC electrode and allowed to air dry, giving a Pt loading of about 60 $\mu g/cm^2$. The catalyst was electrochemically cleaned by cycling its potential between +0.50 and +1.2 V at 50 mV/s in acidic solution until a stable and well-defined cyclic voltammogram was obtained. A platinum disk electrode (ϕ = 10 mm) embedded in glass was used for the infrared experiments. This electrode was polished to a mirror finish, and was electrochemically cleaned in the same manner as the nanoparticles, but with an upper potential limit of +1.4 V. For the nanoparticle film electrodes, the electrochemical surface area was determined to be about 8 cm^2 by integration of the hydrogen adsorption peaks. Current densities reported herein are normalized to the surface area determined by this method for each experiment.

3.2.4 In situ FTIR Parameters

The apparatus used for this work is described in the methodology chapter. Spectra were collected at an 8 cm^{-1} resolution, and 340 scans were co-added over a course of 120 s for measurements. Spectra are reported as $-\log_{10} \left| R/R_o \right|$, where R is the spectrum collected at a given potential and R_o is the spectrum collected at a reference potential of +0.05 V. Prior to collecting a reference spectrum, the working electrode was pulled back from the prism, and its potential stepped to +1.0 V for 10 s to oxidatively remove adsorbates, and then returned to

+0.050 V. After pressing the electrode against the prism, the reference spectrum was collected. The potential was then stepped to a value of interest, and spectra were collected.

3.2.5 Synthesis of ^{13}C-Labeled DMM

DMM with ^{13}C-labeled methyl carbons was synthesized via a small scale preparation based upon that of Baxter and Abbot,[17] with some modifications. A suspension of paraformaldehyde (0.5 g) in 10% vol. $^{13}CH_3OH_{(aq)}$ (2.0 mL) was heated at 75 ^{o}C for 2 hours. Another 1.0 mL of the $^{13}CH_3OH$ solution was added to the reaction mixture, and heating was continued for another 1 hour. After allowing the solution to cool to room temperature, 2.0 mL of $^{13}CH_3OH$ and 3.0 g anhydrous $CaCl_2$ were added to the mixture. After addition of a small amount of 6 M $HCl_{(aq)}$ (0.1 mL), the mixture was heated to 60^{o}C, with a distillation head on the reaction flask. About 0.5 mL of a clear liquid distilled over when the vapor temperature was about 36 to 40^{o}C. Methanol and DMM form an azeotrope with about 10% methanol.[18] The methanol impurity was removed by stirring the solution with sodium metal overnight, and subsequently vacuum transferring the product to another flask.

3.3 RESULTS AND DISCUSSION

3.3.1 Solution Convection Effects

Although previous studies of DMM electrooxidation have employed both active and passive transport conditions, there has not been an investigation of the effect of convection. Since both the DEMS flow cell used in this work and actual fuel cells utilize active transport conditions, inquiry along these lines should be of interest.

To qualitatively assess how convection would influence this system, cyclic voltammograms (CVs) were collected using a rotating disk Pt/C nanoparticle film electrode under quiescent conditions and with electrode rotation. The CVs obtained in H_2SO_4 and $HClO_4$

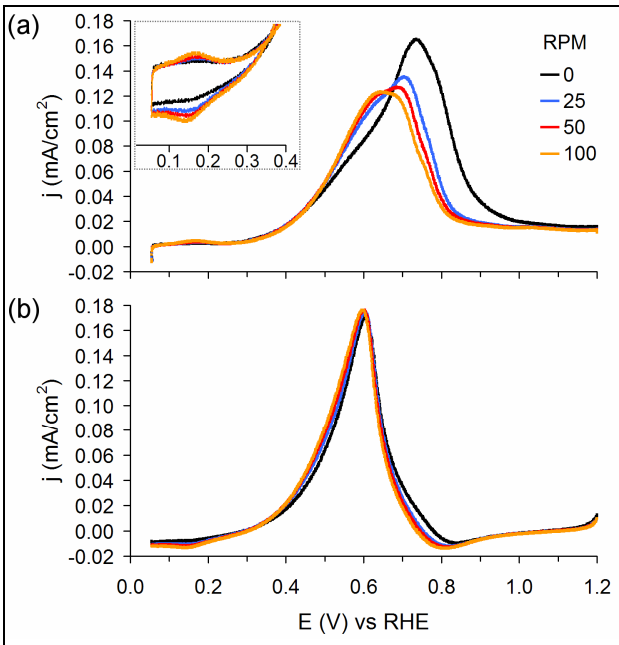

Figure 3.1: Cyclic voltammograms (2nd cycle) of Pt/C in 0.05 M DMM and 0.1 M H_2SO_4 at different rotation rates, noted in the legend. The anodic (a) and cathodic (b) sweeps have been separated for clarity. The inset in (a) is an expanded view of the low potential range. Scan rate: 10 mV/s

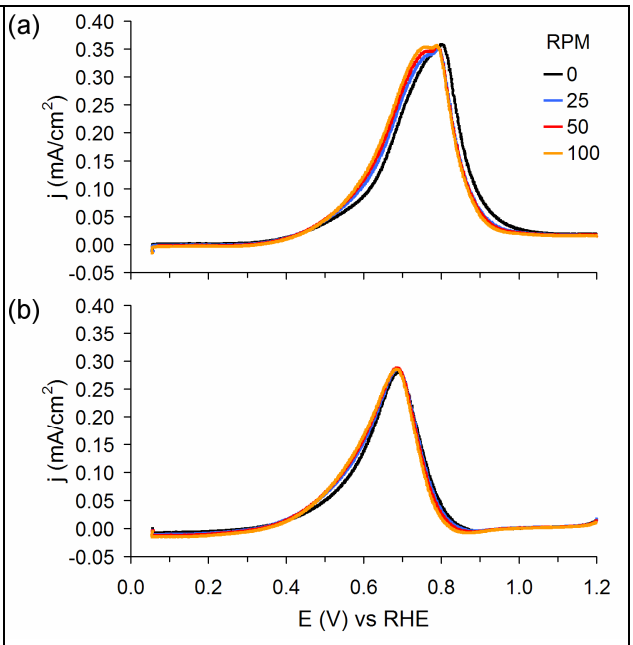

Figure 3.2: Cyclic voltammograms of Pt/C in 0.05 M DMM and 0.1 M $HClO_4$ at the rotation rates noted in the legend, with anodic (a) and cathodic (b) sweeps separated for clarity. Scan rate: 10 mV/s

are shown in figures 3.1 and 3.2, with the anodic and cathodic scans separated for clarity. Though DMM electrooxidation appears to be kinetically limited throughout the potential range,there are changes with varying rotation rate. In the +0.45 to +0.67 V range of the anodic sweep in H_2SO_4 solution and the +0.45 to +0.77 V range in $HClO_4$ solution, there is an increase in current with increasing rotation rate. At potentials beyond this range in H_2SO_4 solution, the trend is the opposite; in $HClO_4$, there is little change. Solution convection had a lesser effect on the cathodic sweeps in both supporting electrolytes.

The trends in both the high and low-potential ranges of the anodic sweep might be, in part, attributed to removal of DMM oxidation products from the diffusion layer under the enhanced transport conditions. Methanol and MF are known products of DMM oxidation,[16] and

can form CO_{ads} on Pt in the lower potential range.[19] If these products form CO_{ads} or other poisoning adsorbates more rapidly than DMM, their removal would lessen poison formation, thus increasing the number of surface sites available for DMM oxidation. There is a slight increase in the hydrogen adsorption-desorption current with increasing rotation rate, which also suggests less poisoning (figure 3.1, inset). The observed increase may also be due, in part, due to enhanced transport of DMM to the electrode surface.

At more positive potentials, the decrease in oxidation current with increasing rotation rate might also be attributed to the transport of products away from the surface. If the electrode was rotated over the low potential range only, and then held stationary in the more positive range, the peak anodic current still diminished and shifted to a more negative potential, as though rotation had continued over the entire range. This could indicate accumulation of products in the diffusion layer over the low potential range when the electrode is held stationary. Rotating the electrode for only a short burst in the more positive potential range caused the oxidation current to drop rapidly, and it did not rise again after rotation ceased. This suggests that the additional current for the stationary electrode is due primarily to solution species and not to adsorbate stripping.

Convection could also decrease the current in the high potential range if it facilitated the adsorption of (bi)sulfate. The low potential range behavior in H_2SO_4 solution suggests a lower coverage of poisoning adsorbates is formed during convection. This would leave more surface sites available for (bi)sulfate adsorption, which could then lower the oxidation current at more positive potentials. This explanation would be consistent with the negligible decrease in oxidation current at more positive potentials in $HClO_4$ solution, since ClO_4^- does not specifically adsorb. The observed behavior likely involves the interplay of loss of products from the

diffusion layer, and the relative surface coverages of (bi)sulfate and adsorbates formed from DMM and its oxidation products.

It does not appear that mass transport of (bi)sulfate plays a dominant role in the changes observed with solution convection. If the (bi)sulfate concentration is increased to 0.5 M or decreased to 0.005 M (in 0.19 M $HClO_4$), trends similar to those noted above are still observed.

3.3.2 Anion Adsorption Effects: (Bi)sulfate

In a PEM fuel cell, the Nafion membrane serves as the electrolyte, in which sulfonic acid groups are tethered to a perfluorinated ethylene backbone. For measurements with free anions, $HClO_4$ and H_2SO_4 are often used as proxies for Nafion. While perchlorate is considered to be a weakly interacting anion, (bi)sulfate specifically adsorbs, meaning there are bonding interactions between the anions and the surface beyond electrostatic attractions. These anions will preferentially adsorb on the surface in the presence of an excess of other, more weakly adsorbing anions. The adsorption strength of Nafion appears to lie between that of perchlorate and (bi)sulfate.[20] *In situ* FTIR experiments and DFT modeling suggest that both sulfonate and triflormethyl groups of Nafion adsorb on the Pt surface.[21]

The DMM electroxidation current observed in H_2SO_4 solution was significantly lower than that observed in $HClO_4$ solution over much of the potential range (figure 3.3a), as would be expected from the higher adsorption strength in the former case. This behavior is in agreement with previous observations for DMM,[2] as well as formic acid,[22] methanol,[23-26] and ethanol.[27] A comparison of the cyclic voltammograms recorded in these two supporting electrolytes shows that the hydride adsorption peaks become sharper in H_2SO_4 solution, showing that (bi)sulfate has already begun to adsorb in this potential range (figure 3.3d). The formation of the surface oxide is shifted to more positive potentials, due to competition with adsorbed (bi)sulfate.

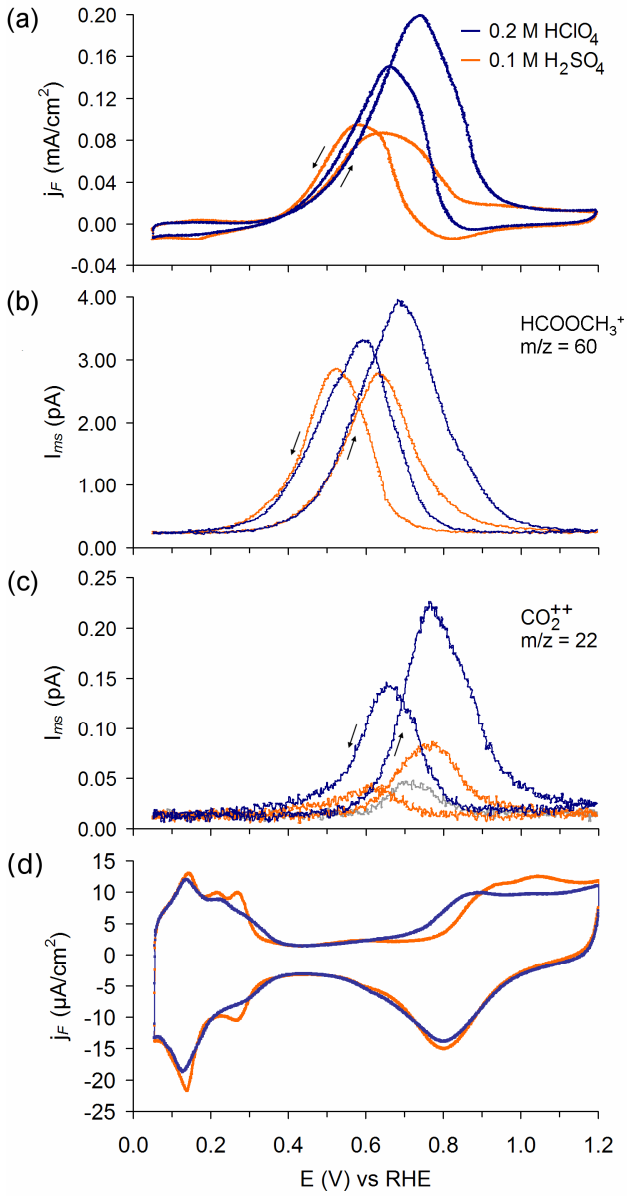

Figure 3.3: Simultaneously recorded cyclic voltammograms (a), and methyl formate and CO_2 mass spectrometric cyclic voltammograms (b,c, respectively) for 0.05 M DMM electrooxidation at Pt/C in 0.1 M H_2SO_4 and 0.2 M $HClO_4$. The second potential cycle is shown in each case. The light gray trace in (c) is CO_2 formed during an adsorbate stripping experiment. Cyclic voltammograms for the Pt/C electrode in DMM – free solutions are shown in (d). Scan rate: 10 mV/s; flow rate: 10 µL/s

A broad feature centered at about +0.57 V is also evident in H_2SO_4 solution, and may be related to the "butterfly" observed for the Pt (111) surface and stepped surfaces with large (111) terraces.[28] This feature was not observed for polycrystalline Pt, and may indicate some preferential exposure of (111) facets in these nanoparticles.

Not only are the peak Faradaic currents lower in H_2SO_4 solution, but also that the peak currents are shifted to more negative potentials (figure 3.3). In $HClO_4$ solution, the peak current in the anodic sweep approximately coincides with the onset of surface oxide formation observed in DMM – free supporting electrolyte, suggesting that blockage of the surface by oxide is responsible for the loss of activity at more positive potentials. In H_2SO_4 solution, however, the peak Faradaic current is attained at a potential at least 0.1 V below the onset of surface oxide formation. The negative shift in the peak position can likely be attributed to the increasing coverage of specifically adsorbed (bi)sulfate with increasing potential.[29]

It is interesting to note that in the potential range from the onset of electrooxidation up to about +0.55 V, there is little difference between the traces observed in the two solutions. Radiometric studies of (bi)sulfate adsorption on polycrystalline Pt have shown the anion coverage to have attained over half of its peak value by +0.55 V.[29] Studies on low index planes, however, have shown that the Pt (111) plane does not begin to adsorb (bi)sulfate until potentials more positive than the other low index planes.[29-31] The Pt (111) plane has also previously been shown to have the most negative onset potential for DMM electrooxidation of the low index planes, and is the most active in this low potential range.[15] In light of this information, the insensitivity to specifically adsorbing anions we observed in the low potential range would be consistent with a significant contribution from the Pt (111) plane to the activity in this range. Another possible explanation is that DMM, or products of its oxidation, effectively compete with

(bi)sulfate for surface sites in the low potential range, preventing it from attaining as high a coverage as it would in DMM-free solution.

The mass spectrometric methyl formate (MF) currents (figure 3.3b) also show little difference between the two supporting electrolytes in the low potential range. Production of MF tracked the Faradic current in a roughly linear manner over this range. In H_2SO_4 solution, the Faradaic current and MF mass spectrometric current attained their peak values in the anodic sweep at the same potential. In $HClO_4$, however, the peak Faradaic current was 0.05 V more positive than the peak MF evolution. This could indicate that even after the rate of DMM oxidation to MF has begun to decrease, the rate of oxidation of products from this initial step continues to increase.

The onset of CO_2 formation is approximately 0.2 V more positive than the onsets of Faradaic oxidation current and of MF evolution (figure 3.3c). Though less CO_2 is produced at all potentials in H_2SO_4 solution, the identity of the supporting electrolyte has little effect on the peak positions in the CO_2 mass spectrometric CVs (MSCVs). The peak CO_2 evolution currents are 0.12 V and 0.07 V more positive than the peak MF currents in H_2SO_4 and $HClO_4$ solutions, respectively. This peak separation is not apparent in the Faradaic current observed in these solutions. In 0.5 M (bi)sulfate (H_2SO_4 + Na_2SO_4, pH = 1) solution, however, the peak separation observed for the products is also somewhat evident in the Faradic current.

Integrating the MF and CO_2 mass spectrometric currents over one potential cycle and taking the relative sensitivity of the spectrometer into account, it was found that more MF than CO_2 was produced under all conditions tested (table 3.1). The MF to CO_2 ratio was higher in H_2SO_4 solution than in $HClO_4$ solution; the amounts of MF and CO_2 produced were both diminished in H_2SO_4 solution, but the effect was larger for CO_2. The fact that the amounts were

not equally diminished might be explained if the process(es) forming MF require fewer surface sites than those forming CO_2.

Table 3.1: Quantification of products formed during a potential cycle
Methyl formate to CO_2 product ratios (MF:CO_2), methyl formate current efficiencies A_{MF}, and $Q_{ms22}/(K^*_{22} \cdot Q_F)$ values obtained using the electrolytes and DMM concentrations noted. These data were obtained under the conditions shown in figures 3.3 and 3.4.

electrolyte	[DMM] (M)	MF:CO_2	A_{MF}	$Q_{ms22}/(K^*_{22} \cdot Q_F)$
0.2 M $HClO_4$	0.050	3.9 ± 0.2	0.57 ± 0.10	0.063 ± 0.010
	0.010	2.0 ± 0.1	0.43 ± 0.08	0.106 ± 0.019
0.1 M H_2SO_4	0.050	8.2 ± 0.3	0.89 ± 0.16	0.054 ± 0.008
0.2 M $HClO_4$ + 0.05 mM HCl	0.050	14 ± 3	0.91 ± 0.20	0.031 ± 0.011
0.2 M $HClO_4$ + 0.1 mM HCl	0.050	25 ± 4	0.97 ± 0.12	0.020 ± 0.005
0.2 M $HClO_4$ + 0.5 mM HCl	0.050	37 ± 6	1.01 ± 0.13	0.014 ± 0.003

The current efficiency for MF, A_{MF}, was higher in H_2SO_4 solution than in $HClO_4$. This indicates that processes, other than oxidation of DMM to MF, make a larger contribution to the overall oxidation current in the latter case. These processes do not necessarily involve oxidation of MF. Previous infrared studies of DMM have shown MF to be relatively difficult to oxidize, and this is further supported by the isotopically labeled DMM study reported herein (*vide infra*). We do not report current efficiencies for CO_2 formation, since the stoichiometric ratio of electrons to moles of CO_2 produced cannot be established with certainty. Furthermore, if the 8 electron oxidation of DMM to MF and CO_2, as proposed by Zhou et al.,[16] is the dominant pathway, a current efficiency of 100% would represent complete oxidation of only 1/3 of the carbon atoms. Instead, we report values of $Q_{ms22}/(K^*_{22} \cdot Q_F)$, which is equivalent to A_{CO_2}/n, where A_{CO_2} would be the current efficiency as typically calculated and n is the stoichiometric ratio of electrons to moles of CO_2 produced. While the overall amount of CO_2 produced in $HClO_4$ solution was higher than in H_2SO_4, the difference in the $Q_{ms22}/(K^*_{22} \cdot Q_F)$ values was not large.

The total amount of CO_2 produced from DMM oxidation in one potential cycle in H_2SO_4 solution amounted to about five times the amount produced during an adsorbate stripping experiment (figure 3.3c). (This experiment was done by stopping the potential cycle at its lower limit, purging the cell with DMM-free solution while maintaining potential control, and then continuing the potential sweep.) This suggests that an indirect electrooxidation pathway,[32,33] proceeding through strongly bound adsorbed species, namely CO, might be responsible for a significant portion of the CO_2 observed. When this same experiment was carried out with $HClO_4$ as a supporting electrolyte, the amount of CO_2 produced during a potential cycle was about ten times greater than the amount produced during the corresponding adsorbate stripping experiment. This may indicate that the turnover rate for forming and oxidizing the adsorbed species is greater in $HClO_4$ solution, or that another mechanism which does not proceed through strongly adsorbed species is in play.

The identification of the adsorbate as CO is supported by the position of the stripping peak and by the observation of CO_{ads} during infrared experiments. Assuming a CO_2 current efficiency of 100% for the adsorbate stripping process, the number of electrons per molecule of CO_2 produced is calculated to be approximately 2, as expected for CO.

3.3.3 Anion Adsorption Effects: Chloride

The adsorption of chloride on Pt is significantly stronger than that of (bi)sulfate. The cyclic voltammogram of Pt in $HClO_4$ with low concentrations of chloride in solution shows that the hydrogen adsorption / desorption peaks are compressed towards more negative potentials, and that formation of the surface oxide is increasingly suppressed with increasing chloride concentration (figure 3.4g). Based upon the variation in surface oxide coverage with chloride concentration, it has been shown that adsorption takes place in two stages.[34,35] In the first stage,

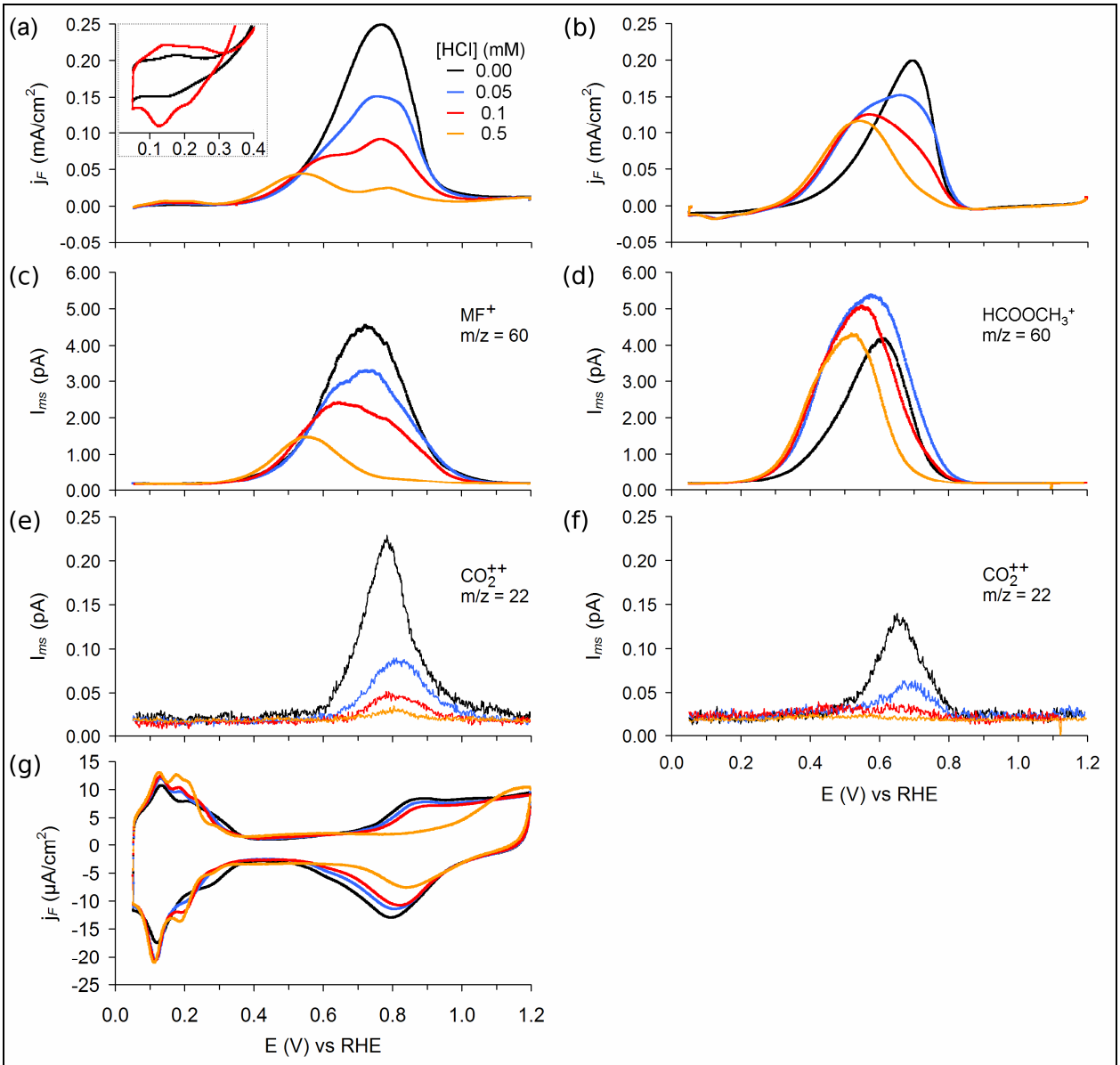

Figure 3.4: Simultaneously recorded cyclic voltammograms (a,b), and methyl formate (c,d) and CO_2 (e,f) mass spectrometric cyclic voltammograms for 0.05 M DMM electrooxidation at Pt/C in 0.2 M $HClO_4$, with varying concentrations of HCl added (noted in the legend). The first three panels on the left hand side show anodic sweeps only, and those on the right hand side show the corresponding cathodic sweeps. The cyclic voltammograms shown in panel (g) were collected for Pt/C in DMM – free solutions (anodic and cathodic sweeps together). Scan rate: 10 mV/s; flow rate: 10 µL/s

at lower chloride concentrations, only the oxide formed below about 1.1 V is affected, while at higher concentrations, oxide formation above this potential is also affected. The concentrations chosen here lie in both ranges, with 0.05 and 0.1 mM in the lower range, and 0.5 mM in the upper range. The chloride concentration required to reach the higher coverage range here is somewhat higher here than was reported in the literature. This may be due to mass transport limitations in chloride at the high surface area nanoparticle film electrode used here.

Chloride adsorption has effects similar to those of (bi)sulfate on the electrooxidation of DMM, though greater in extent (figure 3.4). Both the peak Faradaic current and total amount of oxidative charge passed during a potential cycle decreased with increasing chloride concentration. Two peaks became apparent in the Faradaic current in the anodic sweep, with the more negative peak corresponding to the peak MF production. The significant negative shift in this peak is likely due to higher blockage of surface sites by chloride at more positive potentials. There was a minor positive shift in the potential of peak CO_2 production, which may be due to inhibition of the formation of surface oxide species which participate in DMM oxidation at higher potentials. It has previously been reported that CO oxidation at Pt is shifted to more positive potentials in the presence of chloride[36-38] and bromide,[39] likely due to inhibition of adsorbed OH formation. The more positive peak in the Faradaic current appears to correspond to both stripping of adsorbed CO and to oxidation of DMM to MF. As the adsorbate is stripped from the surface, more sites become available to catalyze the DMM to MF conversion.

The quantity of CO_2 produced decreased drastically with increasing chloride concentration, but interestingly, slightly more MF was produced at low chloride concentrations (0.05 mM and 0.1 mM). At low surface coverages, chloride may prevent DMM or products of its oxidation from forming surface-adsorbed poisons, leaving more surface sites available to

catalyze the DMM to MF conversion. This is consistent with the increased hydrogen adsorption charge observed in chloride containing solutions (figure 3.4a, inset). The increase in MF production occurred primarily in the cathodic sweep, which may be due to some desorption of chloride at potentials in the surface oxide range.[40,41] Upon reduction of the surface oxide, readsorption of chloride may be mass transport limited owing to its low concentration. At higher concentrations, the amount of MF produced decreases as chloride begins to block more surface sites.

The MF to CO_2 product ratios for chloride containing solutions were significantly higher than that observed for H_2SO_4 (Table 3.1). The MF current efficiency approached 100% with increasing chloride concentration, while the $Q_{ms22}/(K^{*}_{22} \cdot Q_F)$ value for CO_2 decreased markedly. This shows that, as with (bi)sulfate, the conversion of DMM to CO_2 is more strongly inhibited than its conversion to MF, suggesting that the former process may require more contiguous surface sites.

3.3.4 Concentration Effects

The CVs and MSCVs collected at different DMM concentrations appear qualitatively similar. A larger hydrogen adsorption charge is apparent at lower DMM concentrations, indicating a lower coverage of adsorbate formed from DMM. Lowering the DMM concentration from 0.05 M to 0.01 M decreased the peak anodic current by about half, and also decreased the MF to CO_2 ratio. As the DMM concentration is lowered, the amount of MF produced diminishes more rapidly than does the amount of CO_2 generated (Table 3.1). A similar trend of more complete oxidation with decreasing concentration has also previously been reported for methanol[42] and ethanol[4], and it may be explained, at least in part, by adsorbate stripping representing a larger fraction of the overall current at lower analyte concentrations. There are

also likely more surface sites available for more extensive oxidation processes at lower concentrations.

3.3.5 Potential Step Experiments

A series of steps to potentials ranging from +0.5 to +0.8 V was conducted, and the simultaneously recorded electrochemical and mass spectrometric currents are shown in figures 3.5 and 3.6. As was seen with cyclic voltammetry, DMM oxidation was inhibited in H_2SO_4 solution in the more positive potential range, while at +0.5 and +0.6 V the effect was less pronounced. Overall, the trends observed in these steady state experiments are similar to those in the cyclic voltammetric experiments. It is useful to carry out this type of potential step experiment, none the less, as potential cycling can yield higher currents due to oxidation of adsorbed poisons at high potentials.

There was a downward trend in the MF current efficiency with increasing potential (figure 3.7). At +0.5 V, A_{MF} was near 100% in H_2SO_4 solution. At all potentials, the A_{MF} values observed in $HClO_4$ solution were lower than those in H_2SO_4 solution. The value of $Q_{ms22}/(K^*_{22} \cdot Q_F)$ was found to increase with potential, but there did not appear to be a large difference between the $HClO_4$ and H_2SO_4 solutions. The ratio of MF to CO_2 produced decreased consistently with potential, and, at each potential, was lower in $HClO_4$ solution than in H_2SO_4 solution. This was due to a larger decrease in the amount of CO_2 produced than in the amount of MF (n.b.: in figures 3.5 and 3.6, the Faradaic current and CO_2 current axes are different).

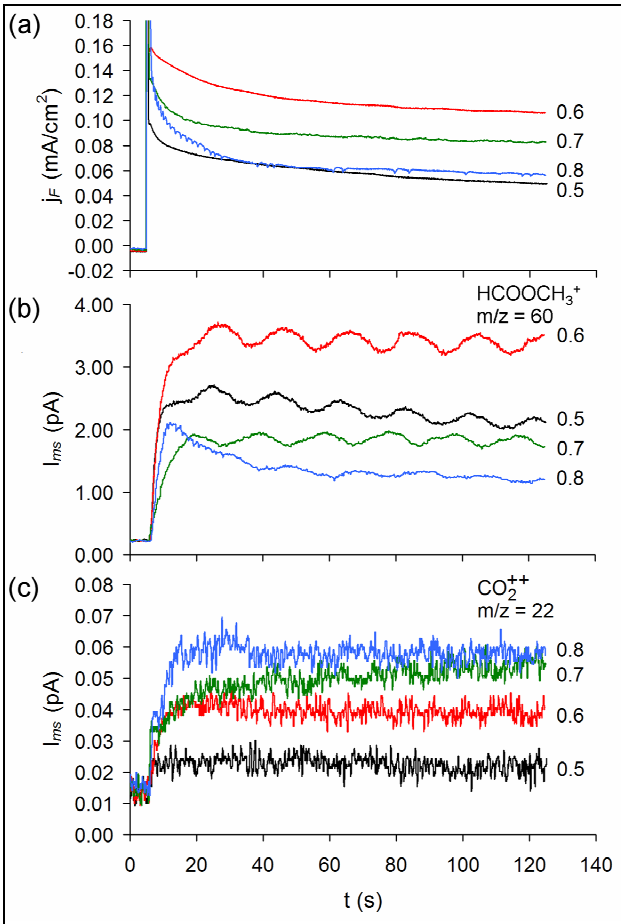

Figure 3.5: Potential steps in 0.05 M DMM in 0.1 M H_2SO_4, with potentials indicated at right. Electrochemical data (a), mass spectrometric current for methyl formate (b) and CO_2 (c). The undulations in the mass spectrometric signals are due to the stepping action of the syringe pump. Initial potential: +0.05 V, flow rate: 10 µL/s

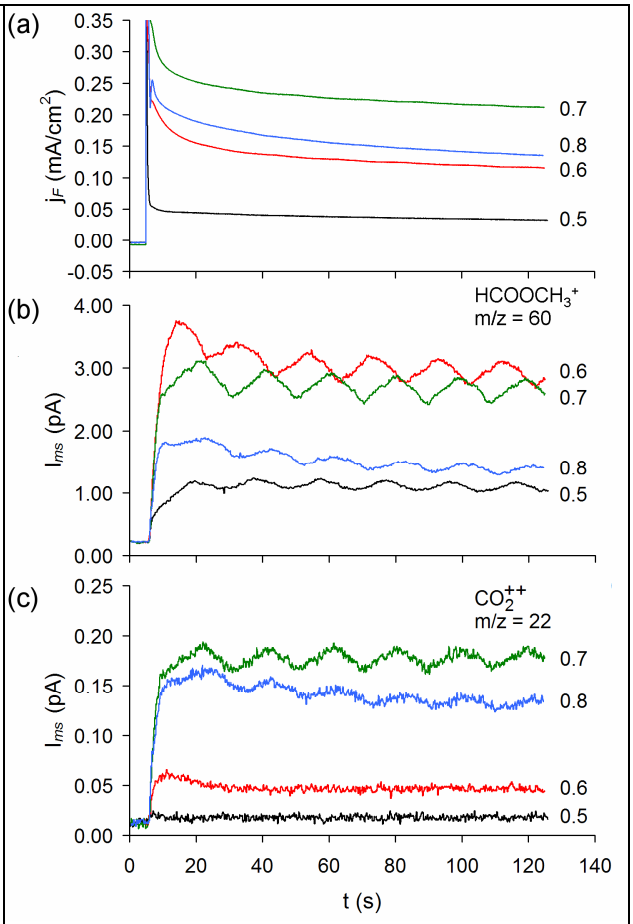

Figure 3.6: Potential steps in 0.05 M DMM in 0.2 M $HClO_4$, with potentials indicated at right. Electrochemical data (a), mass spectrometric current for methyl formate (b) and CO_2 (c). Initial potential: +0.05 V, Flow rate: 10 µL/s

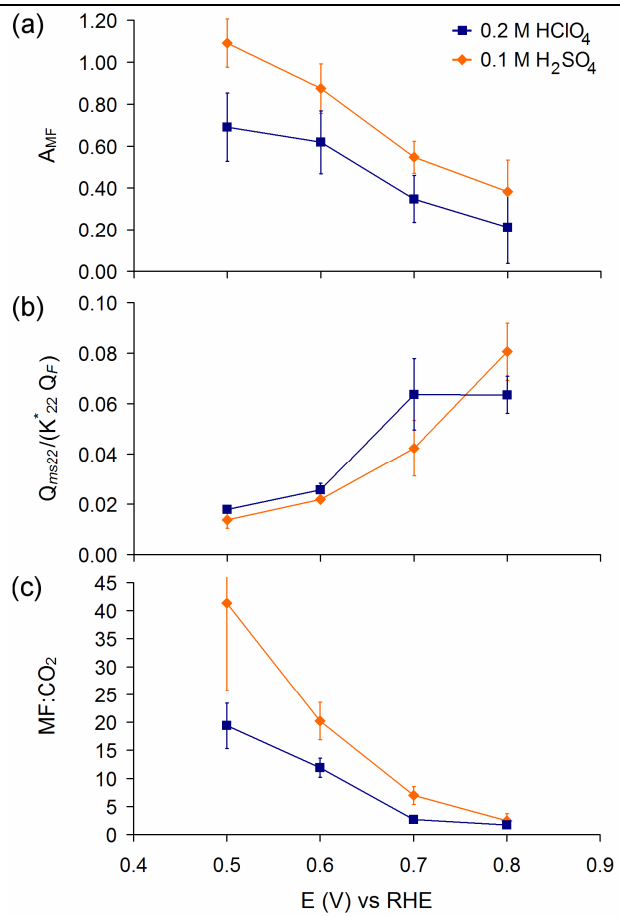

Figure 3.7: Methyl formate current efficiency (a), $Q_{ms22}/(K^{*}_{22}\ Q_F)$ (b), and methyl formate to CO_2 ratio (c) for potential step experiments in 0.1 M H_2SO_4 and 0.2 M $HClO_4$, shown in figures 3.5 and 3.6. Error bars indicate a confidence interval of 80%.

3.3.6 DEMS of Isotopically Labeled DMM

Isotopically labeled DMM ($H_3{}^{13}COCH_2O{}^{13}CH_3$) was synthesized from ^{13}C-methanol and unlabeled formaldehyde. The two chemically distinct types of carbon atoms in the molecule are therefore distinguishable.

Using DEMS, production of $^{12}CO_2$ and of $^{13}CO_2$ during labeled DMM electrooxidation were monitored by CO_2^{++} ion currents at m/z = 22 and 22.5, respectively (figure 3.8). The resolution of the spectrometer was set to a value sufficient to ensure negligible overlap of the two signals, though unfortunately, the signal strength suffered with the increased resolution. The

peak current observed for $^{13}CO_2$ in the anodic sweep was approximately 7 times that for $^{12}CO_2$. A $^{13}CO_2$ to $^{12}CO_2$ ratio of 2 to 1 would be expected if each carbon in the original molecule were equally labile. The higher ratio shows that complete electrooxidation of the methyl carbons to CO_2 is much more facile, though a small amount CO_2 is produced from the central carbon as well.

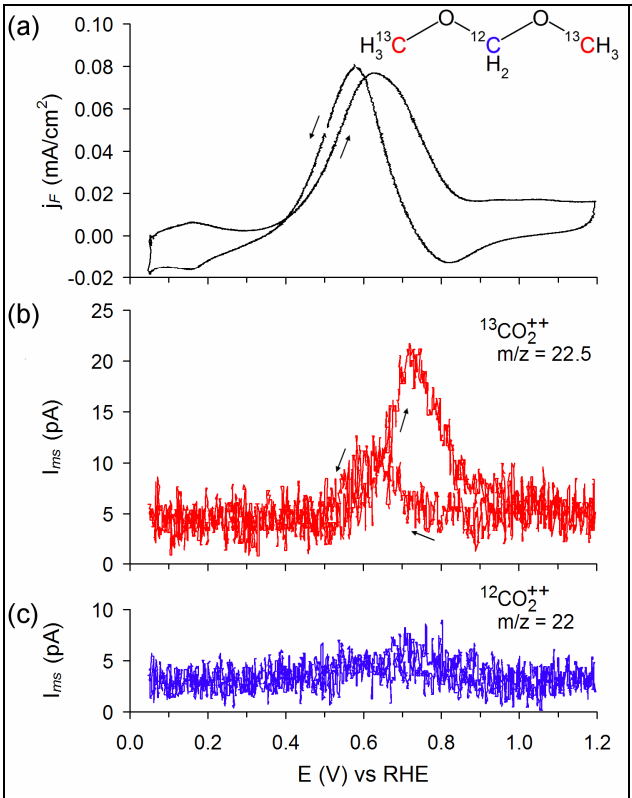

Figure 3.8: Simultaneously recorded cyclic voltammogram (a), and $^{13}CO_2$ and $^{12}CO_2$ mass spectrometric cyclic voltammograms for isotopically labeled 0.05 M DMM at Pt/C in 0.1 M H_2SO_4. Scan rate: 10 mV/s; flow rate: 10 µL/s

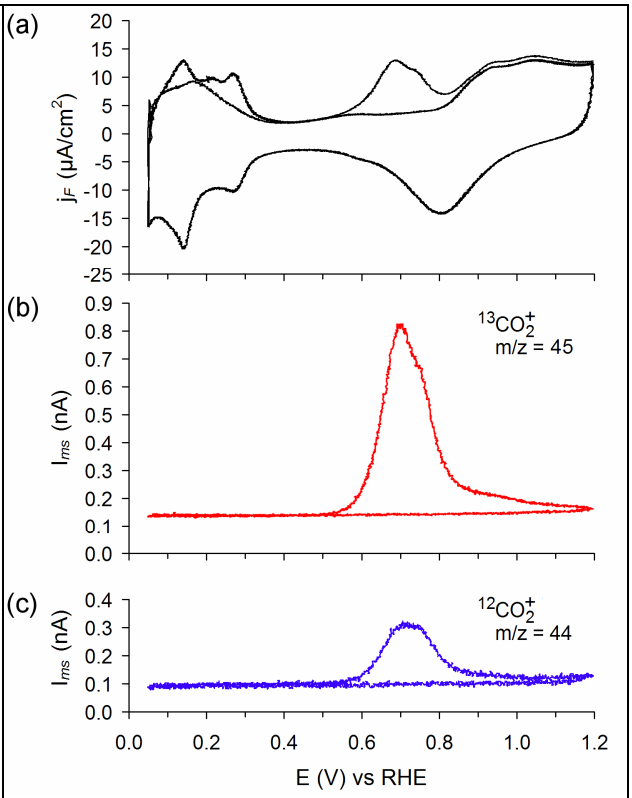

Figure 3.9: Stripping of adsorbate formed from isotopically labeled DMM on Pt/C during potential cycling in 0.1 M H_2SO_4. Electrochemical data (a), mass spectrometric data for $^{13}CO_2$ (b), and $^{12}CO_2$ (c). Scan rate: 10 mV/s; flow rate: 10 µL/s

After three potential cycles in the labeled DMM solution, the potential was stopped at the lower limit (+0.05 V), and the cell was then purged with clean supporting electrolyte while maintaining potential control. This removed DMM and any remaining solution products from

the cell, while preserving electrode-adsorbed species. The adsorbate was then anodically stripped from the electrode using cyclic voltammetry. Production of $^{13}CO_2$ and of $^{12}CO_2$ were followed simultaneously by signals at m/z = 44 and 45 (figure 3.9). Integration of the peaks for the two isotopes yields a $^{13}CO_2$ to $^{12}CO_2$ ratio of approximately 3 to 1, showing that the adsorbate is also preferentially, though not exclusively, formed from the methyl carbons. The fact that the ratio is smaller than that observed for bulk oxidation could possibly indicate that a larger fraction of the methyl groups than of the central carbon is oxidized to CO_2 through an indirect (non-CO forming) pathway.

3.3.7 In situ FTIR spectroscopy of Isotopically Labeled DMM

In situ FTIR is a complementary method to DEMS, in that it can detect both adsorbed and solution species. We used this method to investigate electrooxidation of the labeled and unlabeled DMM at a polycrystalline Pt disk electrode (figure 3.10). Evolution of $^{13}CO_2$ and $^{12}CO_2$ were monitored by peaks at 2,277 cm^{-1} and 2,343 cm^{-1}, respectively. For the labeled DMM, the peak observed for $^{13}CO_2$ was far more intense than that for $^{12}CO_2$, again showing the methyl carbons to be more readily oxidized. The $^{13}CO_2$ to $^{12}CO_2$ ratio ranged from about 6 to 12, depending on the potential, which is higher than that found using DEMS. This discrepancy is likely due to the different mass transport conditions of these two experimental setups. As was shown with the rotating disk electrode experiment (*vide supra*), solution convection can transport partial oxidation products away from the electrode surface before they can be further oxidized. In the thin layer configuration of the FTIR setup, diffusion of products back to the working electrode and their further oxidation is more likely. Time resolved spectral data also show the $^{13}CO_2$ peak to increase more rapidly after the potential step than the $^{12}CO_2$ peak.

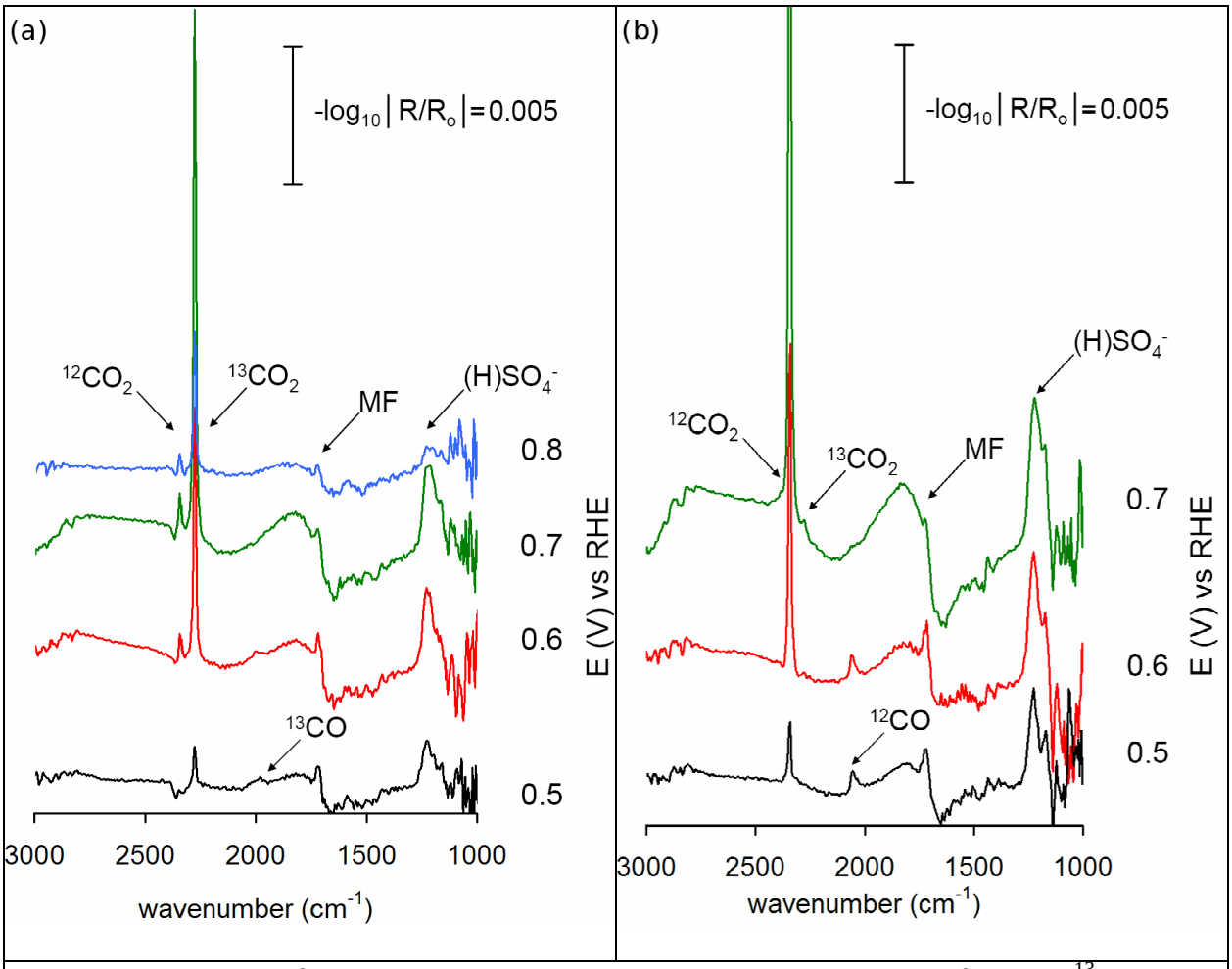

Figure 3.10: Infrared spectra collected during the electrooxidation of 0.05 M ^{13}C – labeled DMM (a) and unlabled DMM (b) at polycrystalline Pt at the indicated potentials in 0.1 M H_2SO_4. Reference spectra collected at +0.05 V.

Though their signals are weaker, other species were also discernable. For the non – labeled DMM, a band at 2,060 cm^{-1} at +0.5 V was attributed to linearly bound CO.[2,14-16] In the spectra collected for labeled DMM at +0.5 and +0.6 V, there is a weak peak at close to 2,000 cm^{-1} at +0.5 V. In both cases, the peak shifted more positive with potential, supporting its identification as a surface adsorbed species. The peak position observed for the labeled DMM is shifted to lower energy as would be expected for ^{13}CO, taking the isotopic shift into account. It has previously been reported that the FTIR spectra of a mixed ^{13}CO and ^{12}CO adlayer on a Pt electrode in H_2SO_4 solution shows only a single peak, with a position ranging between that of a

pure ^{13}CO layer and that of a pure ^{12}CO layer, depending on the isotope ratio. The observation of a single peak rather than discrete peaks was attributed to a vibrational coupling effect.[43] The peak observed here could thus have contributions from both isotopes. The intensity of the CO peak for the labeled DMM was also less intense, which has also been observed for isotopically mixed adlayers.[43]

The peak at 1,720 cm^{-1} can be attributed to MF, while the peak at 1,226 cm^{-1} likely has contributions from both MF and $(H)SO_4$.[16] The weak peak at about 1,435 cm^{-1} might be attributed to $H_2C(OH)_2$.[44] The position of the peak did not shift with potential, suggesting it arose from a solution species rather than an adsorbed species. There was little difference in the peak position between the tests with labeled and non – labeled DMM, suggesting this vibrational mode involved primarily the central, non labeled carbon atom.

The extinction coefficient of the MF carbonyl stretch is very close to that of the CO_2 asymmetric stretch,[16] indicating that significantly more CO_2 was produced than MF in the FTIR experiments, contrary to what was found with DEMS. This might also be attributed to the thin-layer configuration and stagnant solution of the FTIR setup. Time resolved data shows the MF peak increasing and then leveling off shortly after the potential step, while the $^{13}CO_2$ peak continued to grow for a longer duration after the step, in a manner similar to what Zhou et al. observed.[16]

3.3.8 Electrochemical Behavior of DMM Electrooxidation Products: *Methanol, Formaldehyde, and Formic Acid*

Since and methanol and methyl formate have been identified as major products of DMM electrooxidation, the electrochemical behavior of these species is also of interest in this investigation. The electrooxidation of methanol, and its intermediate oxidation products,

formaldehyde and formic acid, have been studied extensively for many years, out of fundamental interest and in relation to direct methanol fuel cells. It has long been held that electrooxidation of formic acid and methanol proceed via the so – called dual path mechanism, with an "indirect" and "direct" pathway.[32] The former pathway has a strongly adsorbed intermediate, the identification of which as CO is supported by *in situ* FTIR spectroscopy.[45] FTIR measurements with ^{13}C labeled methanol have shown that adsorbed CO acts primarily as a poison at lower potentials and not as a reactive intermediate.[46] The "direct" pathway is still not well understood. It was recently suggested that the weakly adsorbed intermediate was formate,[47] but it was later concluded that this species mainly acts as a specifically adsorbing anion and likely only represents a small fraction of the current.[33]

Mechanisms similar to the dual path mechanism proposed for formic acid have also been suggested for methanol, though with additional dehydrogenation steps and additional paths producing formic acid and formaldehyde intermediates.[25,48] Anion adsorption experiments suggest that fewer surface sites are required for the conversion of methanol to formaldehyde or formic acid than to CO_2.[25] In experiments in which an ordered adlayer of CN^- was adsorbed on Pt (111), it was shown that at least three contiguous surface sites are necessary to form CO from methanol, but also that conversion to CO_2 was still possible with fewer than three surface sites.[49,50]

A comparison of methanol and DMM elctrooxidation at Pt/C, and corresponding mass spectrometric CO_2^{++} currents is shown in figure 3.11. As was noted earlier, the onset of DMM electrooxidation is significantly more negative than that of methanol. The onsets of CO_2 formation from the two species are quite similar, however, which also supports a mechanism in which the CO_2 produced from DMM arises from a methanol intermediate.

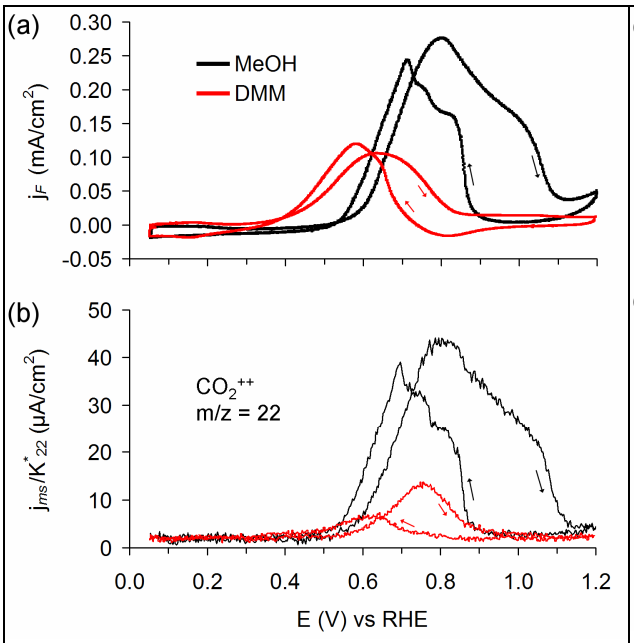

Figure 3.11: A comparison of the Fardaic currents (a) and CO_2^{++} mass spectrometric currents (b) observed during the electrooxidation of 0.05 M methanol and 0.05 M DMM at a Pt/C 50% electrode in 0.1 M H_2SO_4. Scan rate: 10 mV/s; flow rate: 10 μL/s

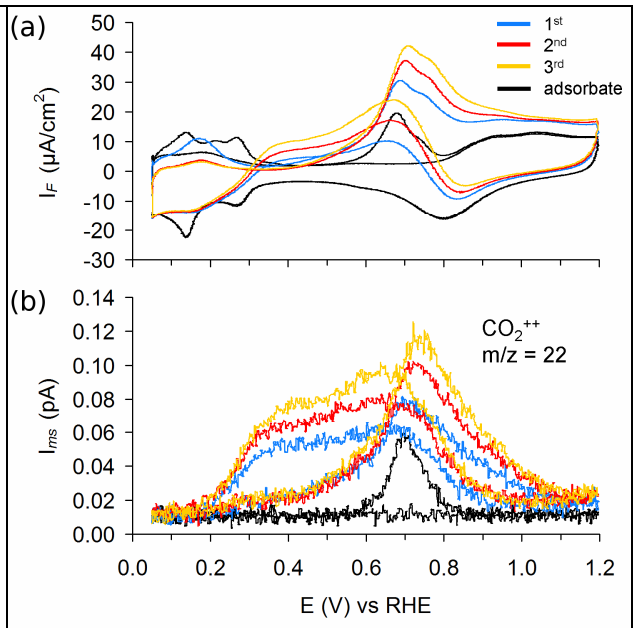

Figure 3.12: Cyclic voltammogram (a) and corresponding CO_2^{++} mass spectrometric signal (b) for 10 mM methyl formate in 0.2 M $HClO_4$. The first, second, and third cycles are shown. Also shown is the stripping voltammogram for the adsorbate formed during the last potential cycle in methyl formate solution. Scan rate: 10 mV/s; flow rate : 10 μL/s

*3.3.9 Electrochemical Behavior of DMM Electrooxidation Products***:** *Methyl Formate*

Miki et al. used ATR – SIERAS to study methyl formate in addition to DMM, and observed adsorbed CO and formate (this setup was sensitive only to adsorbed species due to the ATR configuration).[14] It is difficult to make measurements on MF alone, since it hydrolyzes quite rapidly under acidic conditions. In figure 3.12 the electrooxidation of 0.010 M MF, and the stripping of the adsorbate formed during potential cycling in this solution, are shown.

In the previous CVs presented in this chapter, only the 2nd cycle is shown, since there was generally little change beyond the 2nd cycle. For MF, the first three cycles are presented. It can be seen that there is a continuous increase in the Faradaic current and CO_2 production over the

three cycles, and this can be attributed to the more facile electrooxidation of the MF hydrolysis products than of the parent molecule.

As with DMM, it is not possible to set an electron number for current efficiency calculations, since reactions with 2 to 4 moles of electrons per mole of CO_2 could be written. If a 2 electron oxidation is assumed, however, current efficiencies of close to 1 are obtained. Higher electron numbers would give unphysical results. Several 2 e^- processes can be proposed: (1) The MF could first hydrolyze, and the formic acid produced accounts for most of the observed current. (2) The MF is directly oxidized to CO_2 and methanol. (3) The MF decomposes to form adsorbed CO and methanol, and a significant fraction of the current arises from oxidation of the adsorbed CO. This would be consistent with the close coincidence peak in the anodic sweep with the peak position in the adsorbate stripping experiment. The observed behavior may arise from a combination of these. The relatively large hysteresis between the forward and reverse going sweeps suggests MF poisons the surface more quickly than DMM.

3.3.10 Open Circuit Behavior of DMM at Pt/C

The open circuit electrochemical behavior of DMM at Pt/C was also investigated. These data would be relevant to the open circuit behavior of a direct DMM fuel cell, in particular with regards to DMM crossover to the cathode. As has been shown for several other SOMs, DMM can chemically reduce the surface oxide of Pt under open circuit conditions.[51-53] The first panel of figure 3.13 shows the potential of a Pt/C film electrode in a DMM solution as a function of time. The electrode potential was initially maintained at +0.05 V, and was then stepped to +0.950 V for 30s. It was then set to open circuit. The observed behavior was similar to that reported for other SOMs: the potential gradually decreases at first, followed by a rapid drop, and then a slow increase. Finally, the electrode was placed back under potential control at +0.05 V,

which was followed by a drop in the MF mass spectrometric current. As might be expected from the low activity of Pt for DMM in the oxide potential range, the reduction of the surface was significantly slower than that observed for methanol or formic acid under the same conditions.

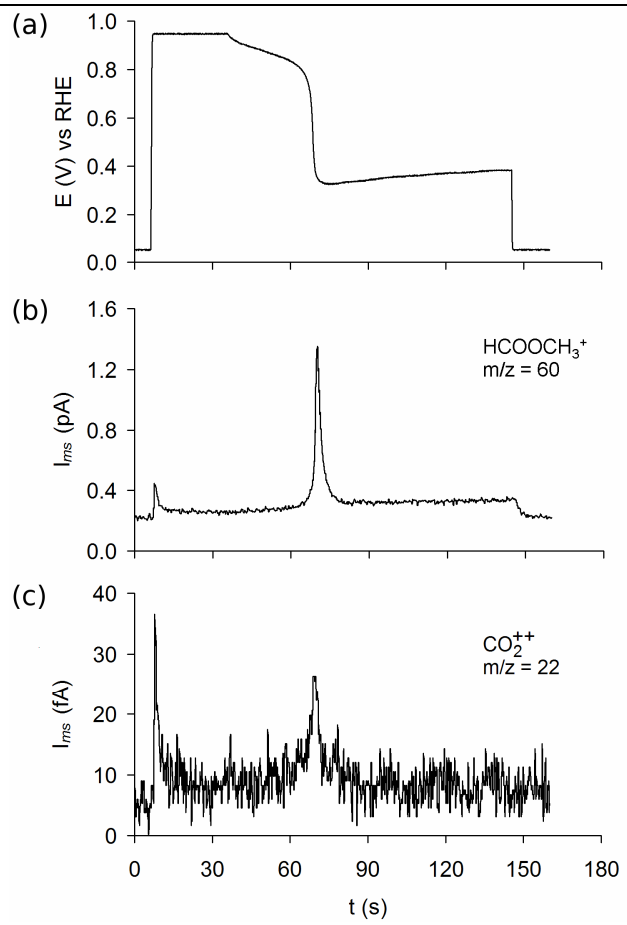

Figure 3.13: A plot of the potential of a Pt/C electrode vs time (a), and the corresponding mass spectrometric currents for methyl formate (b) and CO_2 (c). The solution was 0.05 M DMM and 0.1 M H_2SO_4. The potential was initially held at +0.05 V, stepped to +0.95 V for 30s, then set to open circuit, and finally returned to potential control at +0.05 V. Flow rate: 10 µL/s

Production of CO_2 and of MF were monitored simultaneously with potential. There was a spike in the production of CO_2 and MF immediately following the initial step to high potential, possibly due to oxidation of adsorbed CO and also direct oxidation of DMM prior to blockage of the surface by oxide. There was a second, larger spike in the production of both species,

coincident with the sharp drop in the potential. The ratio of MF to CO_2 produced in the transient is approximately 8 to 1.

There was also a slight decrease in the MF current after restoring the electrode potential to +0.05 V. Prior to returning potential control, the surface may have been simultaneously catalyzing the oxidation of DMM and the reduction of residual O_2 at equal rates.

The initial slow decrease in the OCP may be attributed to the chemical reduction of the Pt surface oxide by DMM:

$$Pt–O + H_3COCH_2OCH_3 \rightarrow Pt + H_3COOCH + H_3COH$$

Over the range in which the potential decreases sharply, there may be a simultaneous electrooxidation of DMM and electroreduction of surface oxide:

$$Pt + H_3COCH_2OCH_3 + H_2O \rightarrow Pt + H_3COOCH + H_3COH + 2H^+ + 2e^-$$

$$Pt–O + 2H^+ + 2e^- \rightarrow Pt + H_2O$$

Each cycle of this reaction yields more free surface sites, which in turn, are also able to oxidize DMM, making this an autocatalytic reaction.

The decrease in the MF current after stepping back to +0.05 shows that DMM continued to be oxidized after the sharp drop in OCP. In this potential range, the oxidation of DMM was likely coupled with the reduction of traces of O_2 remaining in solution, despite deaeration.

3.4 CONCLUSIONS

In H_2SO_4 solution, convection causes DMM oxidation currents to increase at lower potentials and decrease at more positive potentials, and both trends might be explained by transport of products out of the diffusion layer and formation of adsorbed CO from these products, in combination with specific adsorption of (bi)sulfate. The onset of MF formation coincided closely with the onset of Faradaic oxidation current, and the MF current efficiency was

high over the low potential range. The onset of CO_2 formation occurred at approximately +0.55 V, which is about 0.2 V more positive than the onset of Faradaic oxidation current, indicating incomplete oxidation over much of the potential range useful for fuel cell applications. Under all conditions tested, with the exception of the thin layer FTIR measurements, more MF was produced than CO_2. The MF to CO_2 ratio was higher in solutions containing specifically adsorbing anions, and increased with DMM concentration. The relatively large MF to CO_2 ratios, the difficulty of oxidizing the central carbon (indicated by the DEMS and FTIR experiments), and conservation of mass suggest that in addition to the two detected products, significant amounts of single-carbon species (methanol, formaldehyde, and formic acid) were also produced.

3.5 REFERENCES

(1) Narayanan, S. R.; Vamos, E.; Surampudi, S.; Frank, H.; Halpert, G.; Prakash, G. K. S.; Smart, M. C.; Knieler, R.; Olah, G. A.; Kosek, J.; Cropley, C. *J. Electrochem. Soc.* **1997**, *144*, 4195-4201.

(2) Kéranguéven, G.; Sibert, E.; Hahn, F.; Léger, J. M. *J. Electroanal. Chem.* **2008**, *622*, 165-172.

(3) Gurau, B.; Smotkin, E. S. *J. Power Sources* **2002**, *112*, 339-352.

(4) Wang, H.; Jusys, Z.; Behm, R. J. *J. Phys. Chem. B* **2004**, *108*, 19413-19424.

(5) Wang, Q.; Sun, G. Q.; Jiang, L. H.; Xin, Q.; Sun, S. G.; Jiang, Y. X.; Chen, S. P.; Jusys, Z.; Behm, R. J. *Phys. Chem. Chem. Phys.* **2007**, *9*, 2686-2696.

(6) Colmenares, L.; Wang, H.; Jusys, Z.; Jiang, L.; Yan, S.; Sun, G. Q.; Behm, R. J. *Electrochim. Acta* **2006**, *52*, 221-233.

(7) Wang, H.; Zhao, Y.; Jusys, Z.; Behm, R. J. *J. Power Sources* **2006**, *155*, 33-46.

(8) Wakabayashi, N.; Takeuchi, K.; Uchida, H.; Watanabe, M. *J. Electrochem. Soc.* **2004**, *151*, A1636-A1640.

(9) Chetty, R.; Scott, K. *J. Power Sources* **2007**, *173*, 166-171.

(10) Kéranguéven, G.; Coutanceau, C.; Sibert, E.; Hahn, F.; Léger, J.; Lamy, C. *J. Appl. Electrochem.* **2006**, *36*, 441-448.

(11) Shao, M. H.; Warren, J.; Marinkovic, N. S.; Faguy, P. W.; Adzic, R. R. *Electrochem. Commun.* **2005**, *7*, 459-465.

(12) Tong, Y.; Lu, L.; Zhang, Y.; Gao, Y.; Yin, G.; Osawa, M.; Ye, S. *J. Phys. Chem. C* **2007**, *111*, 18836-18838.

(13) Vigier, F.; Coutanceau, C.; Leger, J. M.; Dubois, J. L. *J. Power Sources* **2008**, *175*, 82-90.

(14) Miki, A.; Ye, S.; Senzaki, T.; Osawa, M. *J. Electroanal. Chem.* **2004**, *563*, 23-31.

(15) Kéranguéven, G.; Berná, A.; Sibert, E.; Feliu, J. M.; Léger, J. M. *Electrochim. Acta* **2008**, *54*, 394-402.

(16) Zhou, Z.-Y.; Chen, D.-J.; Li, H.; Wang, Q.; Sun, S.-G. *J. Phys. Chem. C* **2008**, *112*, 19012-19017.

(17) Baxter, R. L.; Abbot, E. M. *Journal of Labelled Compounds and Radiopharmaceuticals* **1985**, *22*, 1211-1216.

(18) Albert, M.; Hahnenstein, I.; Hasse, H.; Maurer, G. *Journal of Chemical & Engineering Data* **2001**, *46*, 897-903.

(19) Jusys, Z.; Behm, R. J. *J. Phys. Chem. B* **2001**, *105*, 10874-10883.

(20) Subbaraman, R.; Strmcnik, D.; Stamenkovic, V.; Markovic, N. M. *J. Phys. Chem. C* **2010**, *114*, 8414-8422.

(21) Kendrick, I.; Kumari, D.; Yakaboski, A.; Dimakis, N.; Smotkin, E. S. *J. Am. Chem. Soc.* **2010**, *132*, 17611-17616.

(22) Lamy, C.; Leger, J. M.; Clavilier, J.; Parsons, R. *Journal of Electroanalytical Chemistry and Interfacial Electrochemistry* **1983**, *150*, 71-77.

(23) Markovic, N.; Ross, P. N. *J. Electroanal. Chem.* **1992**, *330*, 499-520.

(24) Herrero, E.; Franaszczuk, K.; Wieckowski, A. *J. Phys. Chem.* **1994**, *98*, 5074-5083.

(25) Batista, E. A.; Malpass, G. R. P.; Motheo, A. J.; Iwasita, T. *J. Electroanal. Chem.* **2004**, *571*, 273-282.

(26) Wang, H.; Baltruschat, H. *J. Phys. Chem. C* **2007**, *111*, 7038-7048.

(27) Ferreira Jr, R. S.; Oliveira, V. R.; Reis, R. G. C. S.; Maia, G.; Camara, G. A. *J. Power Sources* **2008**, *185*, 853-856.

(28) Mostany, J.; Herrero, E.; Feliu, J. M.; Lipkowski, J. *J. Phys. Chem. B* **2002**, *106*, 12787-12796.

(29) Gamboa-Aldeco, M. E.; Herrero, E.; Zelenay, P. S.; Wieckowski, A. *J. Electroanal. Chem.* **1993**, *348*, 451-457.

(30) Sung, Y. E.; Thomas, A.; Gamboa-Aldeco, M.; Franaszczuk, K.; Wieckowski, A. *J. Electroanal. Chem.* **1994**, *378*, 131-142.

(31) Lachenwitzer, A.; Li, N.; Lipkowski, J. *J. Electroanal. Chem.* **2002**, *532*, 85-98.

(32) Capon, A.; Parsons, R. *Journal of Electroanalytical Chemistry and Interfacial Electrochemistry* **1973**, *44*, 1-7.

(33) Chen, Y. X.; Heinen, M.; Jusys, Z.; Behm, R. J. *Langmuir* **2006**, *22*, 10399-10408.

(34) Novak, D. M.; Conway, B. E. *Journal of the Chemical Society, Faraday Transactions 1: Physical Chemistry in Condensed Phases* **1981**, *77*, 2341-2359.

(35) Zolfaghari, A.; Conway, B. E.; Jerkiewicz, G. *Electrochim. Acta* **2002**, *47*, 1173-1187.

(36) de Becdelièvre, A. M.; de Becdelièvre, J.; Clavilier, J. *Journal of Electroanalytical Chemistry and Interfacial Electrochemistry* **1990**, *294*, 97-110.

(37) López-Cudero, A.; Cuesta, A.; Gutiérrez, C. *J. Electroanal. Chem.* **2003**, *548*, 109-119.

(38) Angelucci, C. A.; Nart, F. C.; Herrero, E.; Feliu, J. M. *Electrochem. Commun.* **2007**, *9*, 1113-1119.

(39) Markovic, N. M.; Lucas, C. A.; Rodes, A.; Stamenkovic, V.; Ross, P. N. *Surf. Sci.* **2002**, *499*, L149-L158.

(40) Li, N.; Lipkowski, J. *J. Electroanal. Chem.* **2000**, *491*, 95-102.

(41) Horányi, G.; Rizmayer, E. M. *Electrochim. Acta* **1985**, *30*, 923-926.

(42) Wang, H.; Löffler, T.; Baltruschat, H. *J. Appl. Electrochem.* **2001**, *31*, 759-765.

(43) Severson, M. W.; Russell, A.; Campbell, D.; Russell, J. W. *Langmuir* **1987**, *3*, 202-209.

(44) Batista, E. A.; Iwasita, T. *Langmuir* **2006**, *22*, 7912-7916.

(45) Parsons, R.; VanderNoot, T. *Journal of Electroanalytical Chemistry and Interfacial Electrochemistry* **1988**, *257*, 9-45.

(46) Leung, L. W. H.; Weaver, M. J. *Langmuir* **1990**, *6*, 323-333.

(47) Miki, A.; Ye, S.; Osawa, M. *Chemical Communications* **2002**, 1500-1501.

(48) Cohen, J. L.; Volpe, D. J.; Abruña, H. D. *Phys. Chem. Chem. Phys.* **2007**, *9*, 49-77.

(49) Cuesta, A. *J. Am. Chem. Soc.* **2006**, *128*, 13332-13333.

(50) Cuesta, A.; Escudero, M.; Lanova, B.; Baltruschat, H. *Langmuir* **2009**, *25*, 6500-6507.

(51) Oxley, J. E.; Johnson, G. K.; Buzalski, B. T. *Electrochim. Acta* **1964**, *9*, 897-910.

(52) Sitta, E.; Varela, H. *J. Solid State Electrochem.* **2008**, *12*, 559-567.

(53) Batista, B. C.; Sitta, E.; Eiswirth, M.; Varela, H. *Phys. Chem. Chem. Phys.* **2008**, *10*, 6686-6692.

CHAPTER 4

The Relation of Structure and Electrochemical Reactivity of a Family of Acetals

4.1 INTRODUCTION

The electrooxidation of dimethoxymethane (DMM) was investigated in detail in the previous chapter. It was found that, despite several attractive properties, its electrooxidation was largely incomplete at low potentials. The information obtained with DEMS and *in situ* FTIR spectroscopy were in agreement with the mechanism proposed by Zhou et al., in which DMM first undergoes a 2 e^- oxidation to methyl formate and methanol, the former of which can be further oxidized to CO_2.[1]

In the interest of learning more about the mechanism of DMM electrooxidation, and also investigating the relationship between chemical structure and electrochemical reactivity, two acetals, structurally related to DMM, were studied: 1,1 – dimethoxyethane (1,1 – DME) and 2,2 – dimethoxypropane (2,2 – DMP). The series can be though of as progressively replacing the C – H bonds of the central carbon of DMM with C – CH_3 bonds. This substitution was chosen with the idea of progressively deactivating the molecule, since the proposed first step of DMM electrooxidation is cleavage of one of the C – H bonds of the central carbon of DMM.

Table 4.1: Structures of the acetals, and ideal electrooxidation reactions, and stoichiometric ratio of electrons to CO_2 (n).

structure	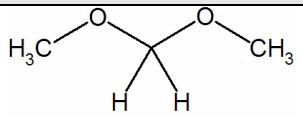	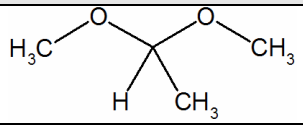	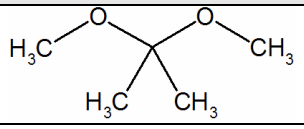
name	dimethoxymethane (DMM)	1,1 – dimethoxyethane (1,1 – DME)	2,2 – dimethoxypropane (2,2 – DMP)
complete electrooxidation reaction	$C_3H_8O_2 + 4H_2O \rightarrow$ $3CO_2 + 16H^+ + 16e^-$	$C_4H_{10}O_2 + 6H_2O \rightarrow$ $4CO_2 + 22H^+ + 22e^-$	$C_5H_{12}O_2 + 8H_2O \rightarrow$ $5CO_2 + 28H^+ + 28e^-$
n	16/3	22/4	28/5

4.2 METHODOLOGY

The procedures utilized herein are the same as those described earlier unless otherwise noted. Reagent grade 1,1 – DME and 2,2 – DMP were obtained from Sigma Aldrich, and were heated over metallic Na overnight to remove methanol and aldehyde / ketone contaminants. Purity of the analytes was confirmed by FTIR spectroscopy. The mass spectrometer used in this work was the Inficon Transpector, rather than the Pfeiffer HiQuad used in the previous chapter. Mass spectrometric currents have been normalized to the calibration constant to compensate for the variability of the calibration constant on different days of testing. The electrode preparation for the DEMS measurements was the same as that used in chapter III. The electrode used for the *in situ* FTIR experiments was a 9 mm Au disk, with 30 $\mu g/cm^2$ of ETek Pt/C 50% deposited from the ink described in chapter II.

4.3 RESULTS

4.3.1 Electrooxidation of 1,1 – Dimethoxyethane (1,1-DME)

This acetal 1,1 – DME is derived from methanol and acetaldehyde. The onset potential for its electrooxidation at Pt was about 0.1 V more positive than that of methanol and 0.3 V more positive than that of DMM (figure 4.1). Its activity in the surface oxide potential range was significantly higher than DMM and methanol. The only species discernable from DEMS data was CO_2, as measured at m/z = 22. The evolution of CO_2 tracked the Faradaic current fairly closely, except above about + 1.0 V, where the Faradaic current continued to increase but the mass spectrometric current deacreased. In the *in situ* FTIR data, CO_2 and singly bound CO were detected. From the structure of 1,1 – DME, methyl acetate might be expected as a product of its electrooxidation if it followed a mechanism analogous to that of DMM. Methyl acetate should be observable from its molecular ion at m/z = 74, but no change above baseline was observed for this mass.

In an adsorbate stripping experiment, two peaks were evident in the mass spectrometric data (figure 4.2). One was located in the potential range typically observed for the electrooxidation of adsorbed CO, and the other broad peak was located in the Pt surface oxide region. This behavior is similar to that previously reported for adsorbates formed from ethanol and acetaldehyde.[2-4] In a study by Silva – Chong et al., labeled acetaldehyde ($H_3{}^{12}C{}^{13}CHO$) was used to study this adsorbate. It was concluded that the lower potential peak formed mainly from the –CHO group, while the higher potential peak formed mainly from the methyl group.[3] The lower potential peak corresponds mainly to adsorbed CO, while the higher potential peak has been attributed to adsorbed CH_x species. These adsorbates may form through the dissociation of the C – C bond on the Pt surface.

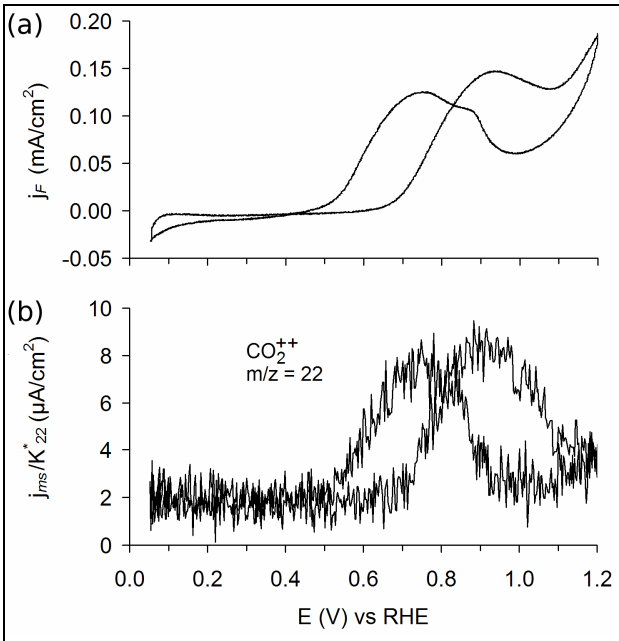

Figure 4.1: Faradaic (a) and CO_2 mass spectrometric (b) currents for 0.05 M 1,1 – dimethoxyethane electrooxidation at Pt/C 50% in 0.1 M H_2SO_4. Scan rate 10 mV/s; flow rate: 10 μL/s

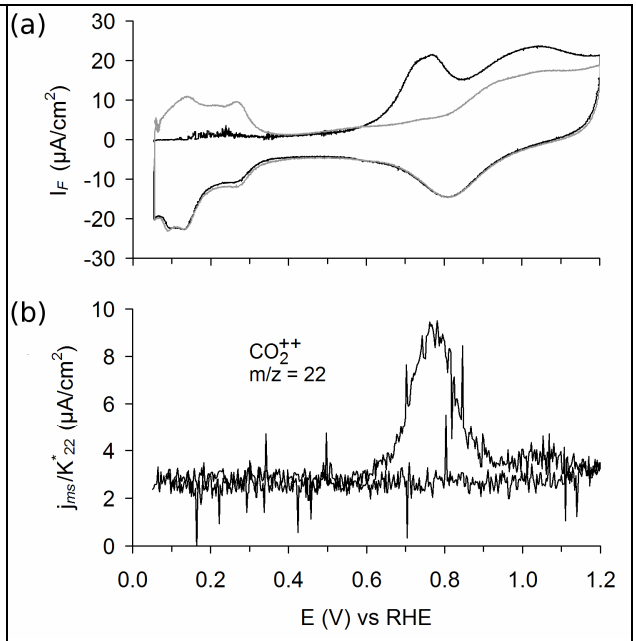

Figure 4.2: Faradaic (a) and CO_2 mass spectrometric (b) currents for stripping of the adsorbate formed during potential cycling in 0.05 M 1,1 – dimethoxyethane in 0.1 M H_2SO_4. Scan rate: 10 mV/s; flow rate 10 μL/s

As with DMM, it is not possible to calculate a CO_2 current efficiency for 1,1 – DME, since the stoichiometric ratio of electrons to moles of CO_2 produced is not known. The complete electrooxidation reaction of this molecule would give a stoichiometric ratio of 22/4 for moles of electrons to moles of CO_2. If the molecule were incompletely oxidized however, reactions with values of n ranging from 4 to 8 might be written, but as with DMM, a current efficiency of 100% could still only represent electrooxidation of a fraction of the carbon atoms. The value of $Q_{ms22}/(K^{*}_{22} \cdot Q_F)$ was found to be about 0.03, suggesting a very low current efficiency for CO_2, even when the largest value of n is assumed. This indicates that large amounts of intermediate oxidation products were generated.

A comparison of the 1,1 – DME bulk oxidation and stripping experiments, (figures 4.1 and 4.2) shows that only about 3 times more CO_2 was produced in the case of bulk oxidation. This suggests that an indirect pathway, proceeding through strongly adsorbed intermediates, accounts for most of the CO_2 produced. Overall, the behavior of 1,1 – DME appears similar to that of acetaldehyde.[4]

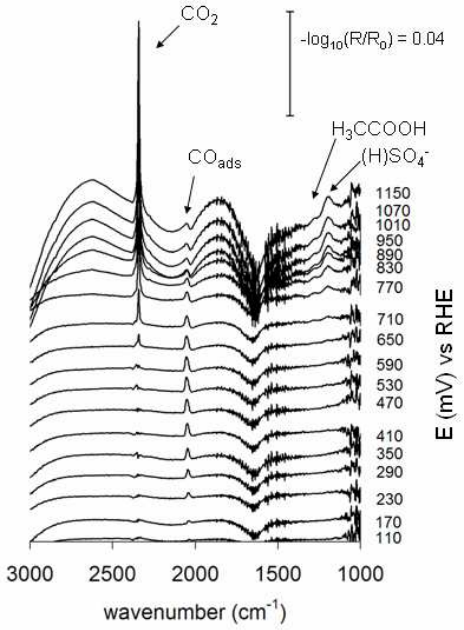

Figure 4.3: Infrared spectra collected during a linear potential sweep of a Pt/C electrode in 0.05 M 1,1-DME and 0.1 M H_2SO_4. Scan rate: 1mV/s; 99 scans co-added over a 30 mV range for each spectrum; E_{ref} = +0.05 V vs RHE

In situ FTIR spectra collected during the electrooxidation of 1,1 – DME at Pt/C 50% revealed the formation of CO_2 and adsorbed CO. The CO peak was present even at high potentials at which it should be oxidized, suggesting that a steady state coverage forms at these potentials. A weak peak was also observed at 1,280 cm^{-1} at potentials similar to those at which CO_2 appeared. This peak may correspond to acetic acid, as a peak in a similar position has previously been observed during the electrooxidation of acetaldehyde.[5,6] The $(H)SO_4^-$ peak may arise due to migration of this anion into the thin layer to compensate for the H^+ generated from 1,1 – DME oxidation.

4.3.2 Electrooxidation of 2,2 – Dimethoxypropane

This acetal is derived from methanol and acetone. The cyclic voltammogram of 2,2 – DMP is very similar to that of methanol, both in terms of onset potential and the shape of the voltammogram. The currents densities for 2,2 – DMP and methanol at the same concentration

were also quite similar. DEMS measurements revealed only the formation of CO_2 (figure 4.4), while *in situ* FTIR spectra showed CO_2, linearly bound CO and a very weak bridge bound CO signal (figure 4.5). A weak peak was observed at 1,373 cm^{-1}, which might be attributed to formic acid.[7] The peak at 1,200 cm^{-1} likely has overlapping contributions from both formic acid and $(H)SO_4$. Negative going peaks were also observed at 2,860 cm^{-1} and 2,970 cm^{-1}, which may be due to consumption of 2,2 – DMP, and are probably associated with C – H stretching modes. No peaks associated with acetone were observed. The value of $Q_{ms22}/(K^*_{22} \cdot Q_F)$ was about 0.12, which would correspond to a current efficiency of 0.72 if it were assumed that n = 6.

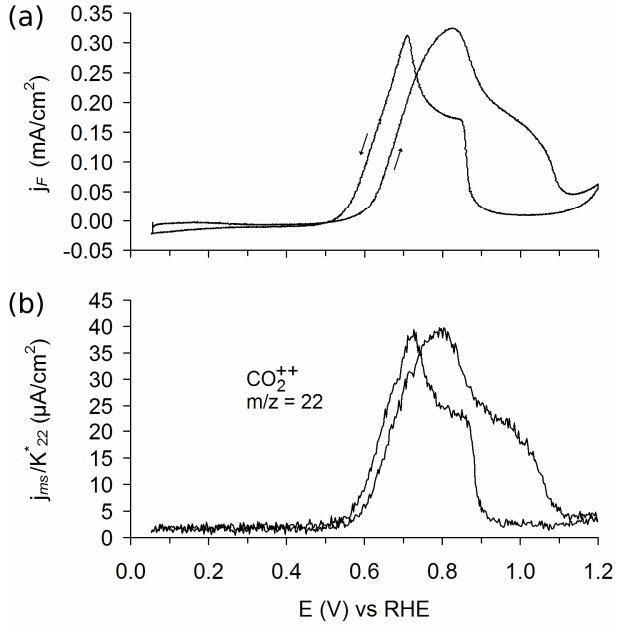

Figure 4.4: Fardaic current (a) and corresponding CO_2^{++} mass spectrometric (b) cyclic voltammograms for 0.05 M2,2 – dimethoxypropane electrooxidation at Pt/C in 0.1 M H_2SO_4 solution. Scan rate: 10 mV/s; flow rate: 10 μL/s

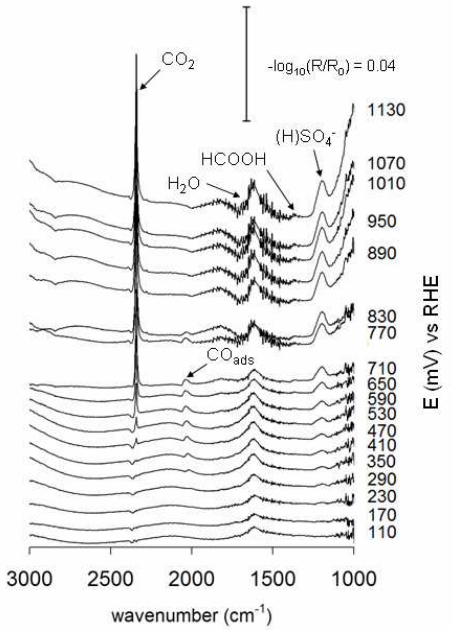

Figure 4.5: Infrared spectra collected during a linear potential sweep of a Pt/C electrode in 0.05 M 2,2-DMP and 0.1 M H_2SO_4. Scan rate: 1mV/s; 99 scans co-added over a 30 mV range for each spectrum; E_{ref} = +0.05 V vs RHE

In a separate measurement it was shown that acetone does not readily undergo electrooxidation at Pt, with no discernable oxidation current in the double layer range of the CV. A small oxidation current was evident in the Pt surface oxide region in the anodic sweep.

Reduction of acetone begins at about +0.15 V vs RHE. This suggests that the acetone backbone of 2,2 – DMP is relatively inert to electrooxidation.

It might be suggested that the observed behavior was due to hydrolysis of the 2,2 – DMP to methanol and acetone. This does take place to some extent, as acetone was observed mass spectrometrically in solutions of 2,2 – DMP. It is not expected, however, that this would occur so rapidly that hydrolysis products would entirely determine its response. DMM does not undergo significant hydrolysis on the time scale of the measurement under these conditions, and 2,2 – DMP is expected to hydrolyze more slowly than DMM. This is also supported by the fact that the CV does not show large changes between consecutive cycles.

4.4 DISCUSSION

The cyclic vltammograms of the three acetals and methanol are superimposed for comparison in figures 4.6 and 4.7. It is somewhat surprising that the reactivity of 1,1 – DME did not appear to be analogous to DMM. Only one of the C – H bonds of the central carbon was replaced, so it might be expected that it could undergo conversion to methyl acetate, but none was detected. It may be that sterics prevent 1,1 – DME from adsorbing on the electrode surface in such a way that it can follow this pathway. Another possibility is that the addition of the methyl group alters the electronic structure in such a way that it is no longer energetically favorable for Pt to insert into the remaining C – H bond. It could also be that Pt does cleave this bond, but then the subsequent steps do not lead to the formation of methyl acetate.

It was not entirely clear what the major products of 1,1 – DME electrooxidation were, as the only clearly identified products were CO_2 and CO, and the former did not appear to be a major product from its low current efficiency. It appeared that some acetic acid may have been

produced. It is also possible that methanol, formaldehyde, and formic acid were produced, as these are not as readily detected by DEMS and *in situ* FTIR.

One possible reaction path would be the oxidation of 1,1 – DME to acetic acid and methanol:

$$H_3COC(CH_3)HOCH_3 + 2H_2O \rightarrow H_3CCOOH + 2H_3COH + 2H^+ + 2e^-$$

In another possible path, the acetaldehyde backbone of 1,1 – DME dissociates to form CO and CH_x adsorbates, along with methanol:

$$H_3COC(CH_3)HOCH_3 + H_2O \rightarrow H_3C_{ads} + CO_{ads} + 2H_3COH + H^+ + e^-$$

At low potentials, this pathway would serve only to block the catalyst surface, but at high potentials, the CH_x and CO adsorbates could be further oxidized to make CO_2. If methanol was a major product, it might be expected that more CO_2 would have been formed. It may be that the surface is so heavily blocked with adsorbates from the dissociation of the acetaldehyde backbone that few are available to completely oxidize methanol. The onset of 1,1 – DME oxidation and CO_2 production did not occur until potentials approaching the Pt oxide region, suggesting that surface oxide species are required for the oxidation.

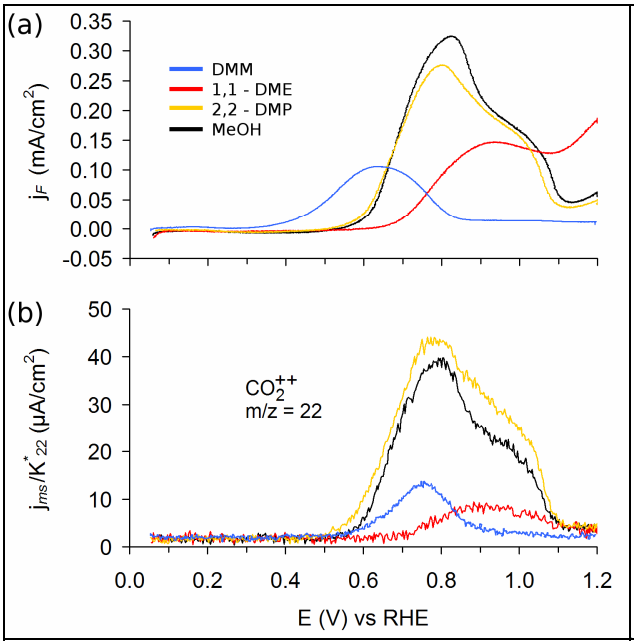

Figure 4.6: Faradaic (a) and CO_2 mass spectrometric currents (b) observed for dimethoxymethane, 1,1 – dimethoxyethane, 2,2 – dimethoxypropane, and methanol at a Pt/C electrode. Only anodic sweeps are shown. In each case, the analyte concentration was 0.05 M, and the solution was 0.1 M H_2SO_4. Scan rate: 10 mV/s; flow rate: 10 μL/s

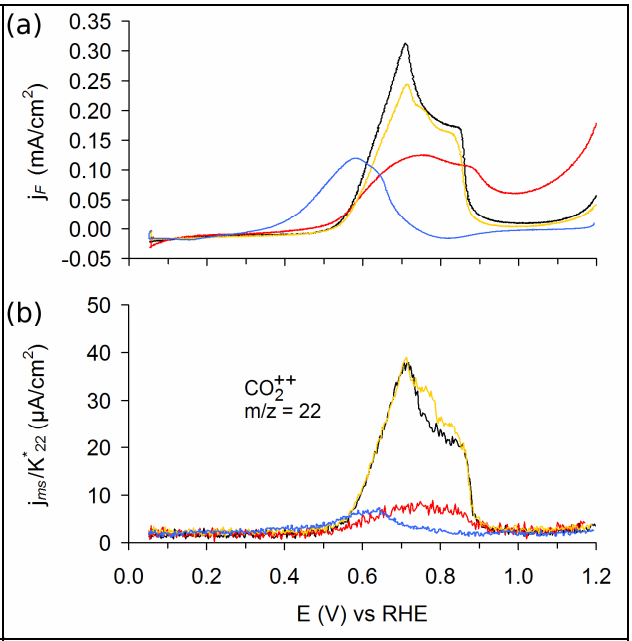

Figure 4.7: Cathodic sweeps corresponding to the anodic sweeps shown in figure 4.6.

The reactivity of 2,2 – DMP did not resemble that of DMM, nor was it expected to, given that both of the C – H bonds of the central carbon were replaced with C – C bonds, and the difficulty with which the acetone backbone is oxidized. It is somewhat surprising how closely its reactivity resembled that of methanol, however. This result is consistent with the view that methanol primarily adsorbs via cleavage of a C – H bond, rather than its O – H bond.[8] This line of reasoning, however, would not be consistent with the reactivity of dimethyl ether, in which the O – H bond is also replaced with a second O – C bond. It shows a more positive onset potential, and a significantly lower current density than methanol.[9,10] Since 2,2 – DMP is a significantly larger molecule than dimethyl ether, it would be expected that it would be more difficult for it to

adsorb on Pt in the correct orientation to undergo electrooxidation. This does not seem to be the case. The difference in reactivity could possibly be due to differences in the electronic structures of dimethyl ether, methanol, and 2,2 – DMP.

Since the acetone backbone of 2,2 – DMP is unreactive for the most part, and taking into account that no acetone was detected as a product, and that the observed cyclic voltammogram was quite similar to that of methanol, a reaction producing CO_2 and a methanol – acetone hemiacetal might be proposed:

$$H_3COC(CH_3)_2OCH_3 + 2H_2O \rightarrow H_3COC(CH_3)_2OH + CO_2 + 6H^+ + 6e^-$$

4.5 CONCLUSIONS

Despite the structural similarities of this group of acetals, they did not display similar reactivities. The behavior of 1,1 – DME more closely resembled that of its acetaldehyde backbone, while the behavior of 2,2 – DMP more closely resembled that of its methyl groups. As might be expected for higher complexity molecules, their electrooxidation was far from complete, indicating these are unsuitable for use in direct fuel cells.

4.6 REFERENCES:

(1) Zhou, Z.-Y.; Chen, D.-J.; Li, H.; Wang, Q.; Sun, S.-G. *J. Phys. Chem. C* **2008**, *112*, 19012-19017.

(2) Wang, H.; Jusys, Z.; Behm, R. J. *Fuel Cells* **2004**, *4*, 113-125.

(3) Silva-Chong, J.; Guillén-Villafuerte, O.; Rodríguez, J.; Pastor, E. *J. Solid State Electrochem.* **2008**, *12*, 517-522.

(4) Wang, H.; Jusys, Z.; Behm, R. J. *J. Appl. Electrochem.* **2006**, *36*, 1187-1198.

(5) Rasch, B.; Iwasita, T. *Electrochim. Acta* **1990**, *35*, 989-993.

(6) Farias, M. J. S.; Camara, G. A.; Tanaka, A. A.; Iwasita, T. *J. Electroanal. Chem.* **2007**, *600*, 236-242.

(7) Batista, E. A.; Iwasita, T. *Langmuir* **2006**, *22*, 7912-7916.

(8) Batista, E. A.; Malpass, G. R. P.; Motheo, A. J.; Iwasita, T. *J. Electroanal. Chem.* **2004**, *571*, 273-282.

(9) Shao, M. H.; Warren, J.; Marinkovic, N. S.; Faguy, P. W.; Adzic, R. R. *Electrochem. Commun.* **2005**, *7*, 459-465.

(10) Tong, Y.; Lu, L.; Zhang, Y.; Gao, Y.; Yin, G.; Osawa, M.; Ye, S. *J. Phys. Chem. C* **2007**, *111*, 18836-18838.

CHAPTER 5

A Combined Scanning Differential Electrochemical Mass Spectrometer (SDEMS) and Scanning Electrochemical Microscope (SECM) for the Analysis of Combinatorial Electrocatalyst Libraries

5.1 INTRODUCTION

5.1.1 Background of Combinatorial Screening

The electrooxidation reactions of small organic molecules (SOMs), such as methanol or ethanol, are slow processes at room temperature. This is a factor which severely limits the performance of fuel cells directly utilizing SOMs as fuels. To hasten the search for new catalysts for these reactions, we have taken a high throughput combinatorial approach. To generate combinatorial libraries of compositions, up to four different elements are simultaneously magnetron sputtered onto a three inch silicon wafer.[1,2] Oxide and carbide composition spreads can be produced by sputtering in a reactive atmosphere,[3] and nitrides have been produced by post – treatment of a sample by heating in an ammonia atmosphere.[4]

To screen these libraries, we employ a pH – sensitive fluorescence assay, originally developed by Reddington et al.[5] In this method, quinine ($pK_{a1} = 4.24$, $pK_{a2} = 8.55$)[6] is used as an indicator. While its basic forms display negligible fluorescence under UV light, its doubly protonated form shows intense blue fluorescence. When a fuel is oxidized at the electrode surface, H^+ accumulates in the diffusion layer, lowering the local pH into the range in which quinine will fluoresce. This method allows all regions of the library to be screened for activity in parallel.

While this method is highly effective for rapid assessment of a library, it does not necessarily indicate the extent of the reaction occurring at a given location. A location which the fluorescence assay indicates to be active for ethanol electrooxidation, for example, may only catalyzing its 2 e^- oxidation to acetaldehyde. For this reason, we have constructed a scanning

DEMS (SDEMS), which can spatially resolve reaction products in an unambiguous manner. Additionally, this instrument can be used as a scanning electrochemical microscope (SECM), which, with an appropriately selected tip material, could also serve as a chemically selective probe. Herein, the development of this instrument is described. Additionally, brief reviews of the literature on the use of scanning probe mass spectrometers, and on the use of SECM for the analysis of combinatorial libraries are given.

5.1.2 Previous Work on Scanning Probe Mass Spectrometers for Heterogeneous Catalysis

Scanning probe mass spectrometric instruments have previously been developed for screening combinatorial libraries of heterogeneous catalysis. Cong et al. developed a system to analyze sputter – deposited libraries for activity towards gas phase reactants.[7,8] That system utilized a probe with capillaries to deliver and withdraw gases, and also to act as an inlet to the mass spectrometer vacuum chamber. The composition library was held by an XY translation stage. When a given composition was held in proximity to the probe, it was heated locally by a laser incident on the back of the substrate, allowing reactivity to be tested over a range of temperatures.

Li et al. described a similar system for spatial resolution of gas phase species involved in reactions at a solid surface.[9,10] Similar to the setup of Cong et al., this system utilized concentric capillaries, with one delivering gaseous species, and the other acting as the inlet to the mass spectrometer chamber. This system was also capable of mapping surface topography using a negative feedback mode, based upon hindrance of mass transport of a chemically inert gas to the inlet by the surface, at small probe-substrate separations. Unlike the system of Cong et al., data were collected while continuously scanning the substrate under the tip.

Roos et al. developed a scanning probe mass spectrometer system with a simpler tip design, which consisted of a single capillary inlet to the mass spectrometer system.[11] This system was also used for the study of gas phase reactants at a catalyst surface. The tip height was determined using a fiber optic displacement sensor.

There has been less work on scanning mass spectrometer systems for liquid environments, and even less in electrochemical environments. The first such work appears to be that of Modestov et al., in which a scanning electrospray ionization (ESI) inlet was used it to image the electrooxidation of N,N-dimethyl-p-phenylenediamine at Pt band electrodes. Similar to some of the systems for gas phase species, the probe consisted of two concentric capillaries; the outer dispensed reactant containing solution, while the inner withdrew solution, and passed it over the ESI inlet.[12]

The scanning DEMS (SDEMS) technique was first described by Jambunathan and Hillier.[13,14] This system utilized a capillary probe in which the end was covered with a porous Teflon membrane. The capillary was backed by a roughing pump, and was joined to a high vacuum chamber containing a quadurupole mass spectrometer. The tip height was controlled visually, using a CCD camera to aid the operator. This system was used it to study methanol electrooxidation at an array of PtRu electrodes of varying atomic ratios.

While not scanning instruments, there have been two other DEMS configurations related in terms of placing the membrane inlet at the end of a probe.[15,16] These were configured to use with bead – type single crystal electrodes used in the hanging meniscus configuration, with the tip approaching the electrode from below.

5.1.3 The use of SECM for the analysis of combinatorial libraries

The scanning electrochemical microscopy (SECM) technique was developed by the Bard group in the 1980's, and has been expanded upon extensively since then.[17] In short, the scanning probe used in this technique consists of an electrode, generally with a diameter of 25 µm or less, encased in an insulator. Some aspects of this technique are further discussed later in this chapter. SECM has found some use in the screening of combinatorial electrocatalyst libraries. Hillier et al. developed a screening method using the H^+/H_2 couple as a redox mediator in a dilute acidic solution. An Au SECM tip was used to reduce H^+ to H_2, which could then be oxidized back to H^+ if the tip was sufficiently close to an active substrate.[18] This method was used to screen a gradient of Pt – Ru compositions for CO tolerance for the H_2 oxidation reaction.[19] Prochaska et al. used a H^+ – selective potentiometric SECM tip to detect H^+ generated from methanol electrooxidation. This acted as a higher resolution complement to the fluorescence assay method.[1]

The Bard group has developed tip generation – substrate collection methods for screening composition arrays. In one, an Au – Hg amalgam tip is used to reduce CO_2/HCO_2^- to formate, which can be oxidized by active compositions on the substrate.[20] In another recently developed SECM – related technique, a micropipette is loaded with an electroactive species, such as methanol, dissolved in an organic solvent which is immiscible with water. The electroactive species is able to cross the interface between the water and organic solvent, and diffuse into solution. When this tip approaches an active substrate, the substrate current will increase due to the impinging dispensed species.[21]

5.2 METHODOLOGY

5.2.1 The Membrane Inlet Tip

The vacuum and mass spectrometer system used in this work were described in detail in the methodology chapter II. The membrane inlet system consisted of a hollow conical stainless steel tip, with a stainless steel frit at its end. The tip was covered with a porous Teflon membrane, which was fastened with heat – shrink tubing. The porosity and pore size of the frit were low enough that in the event it was exposed to liquid, i.e. if the membrane broke, the chamber pressure would not rise enough to damage the mass spectrometer or pumps. The tip was connected to the vacuum system with a DN 16 flexible metal hose.

A T – piece was added at the junction between the vacuum hose and the angle valve. An additional valve was connected to the side of this T – piece, allowing the flexible tubing to be pumped down with a diaphragm pump prior to opening it to the mass spectrometer chamber. This was necessary, as the quantity of air at atmospheric pressure in the hose was large enough that the pressure increase when opening to the mass spectrometer chamber was hazardous to the turbo pumps.

5.2.2 Tip Positioning

The tip was held by an arm connected to an XYZ positioning system, obtained from Velmex, inc., (Bloomfield, NY). Motion in the X and Y directions was driven by stepper motor – powered leadscrews, controlled by computer via a VXM-2 stepper motor controller, connected via an RS – 232 connection. Each motor step corresponded to a 2.5 µm increment. Control of the Z position was manual, using a leadscrew (A6009Q1-S6 UniSlide).

A custom LabVIEW program was written to synchronize collection of mass spectrometric data with the movement in the XY plane. The program allows the user to specify

travel distances and speeds for each scan direction, and all parameters entered by the user are written to the data file. Data collection in each row scan was triggered by a signal on a digital output of the VXM-2 to the PFI0 digital input of the PCI-MIO-16E-1 National Instruments card. The LabVIEW software is described in greater detail in the appendix.

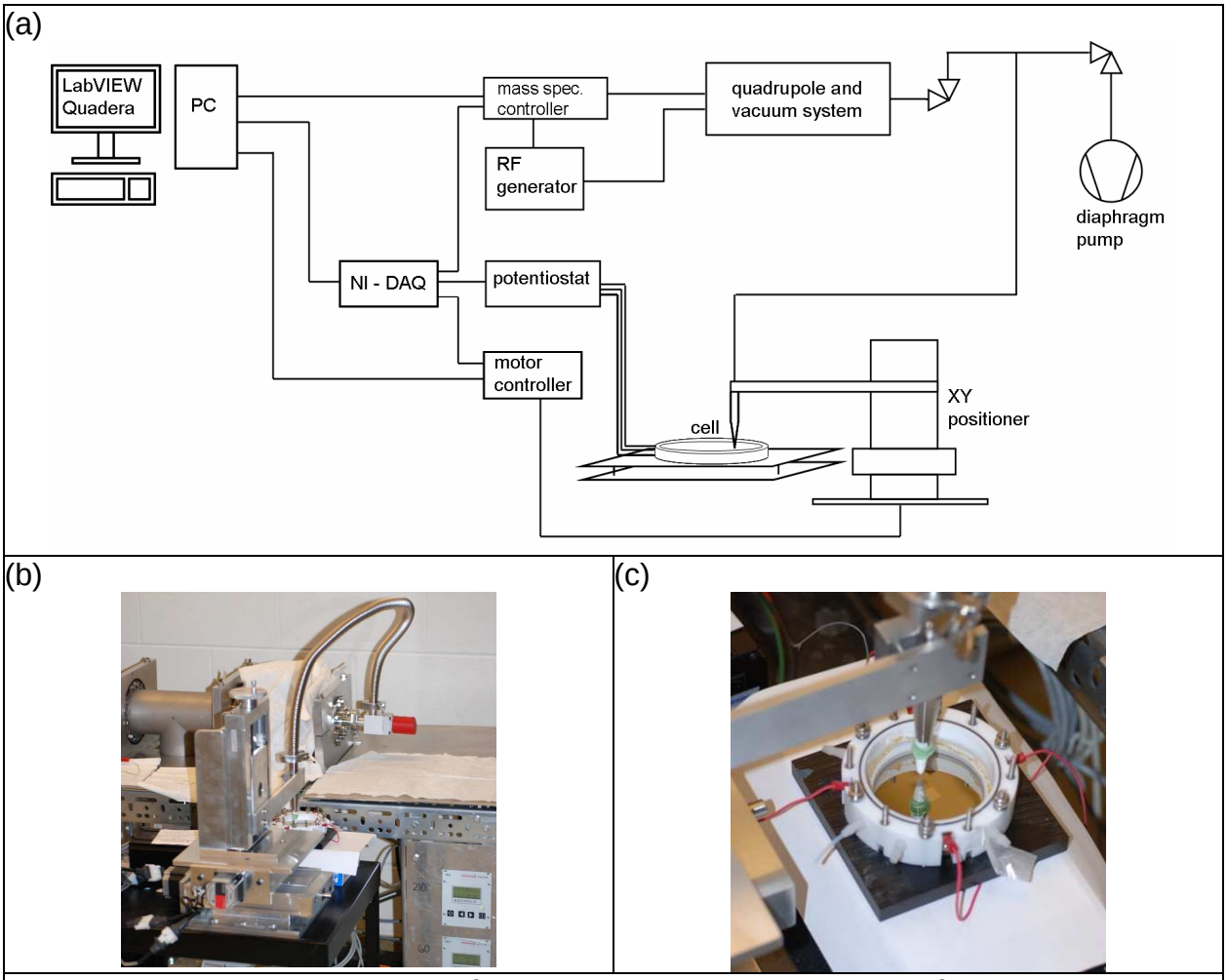

Figure 5.1: Block diagram of the SDEMS setup (a), photograph of the scanning attachment connected to the vacuum system (b), and a close – up photograph of the SDEMS tip over the electrochemical cell (c).

5.2.3 Electrochemical Cell

The electrochemical cell used in this work is the same as that used in previously reported work. In short, it was designed to accommodate a 3 – inch Si wafer, sputtered with a composition spread. It consisted of a Teflon ring, which sealed against the wafer with a Teflon

O – ring (figure 5.1c). Despite being degenerately doped, the through plane resistance of the wafer was extremely high, so electrical contact was made to the top surface with four phosphorous bronze contacts, outside of the region sealed by the O – ring. The counter electrode was a coiled Au wire, which rested on a ridge in the Teflon ring around the perimeter of the wafer. The reference electrode was contained in a separate chamber, connected by a solution filled capillary. The potential of the sample was controlled using a PAR 173 Potentiostat / Galvanostat. For SECM measurements, the tip potential was controlled using an Ensman Instruments EI – 400 bipotentiostat. The current capability of this potentiostat was not sufficient to control the substrate potential as well, so this was at open circuit during SECM measurements. The use of coaxial cables for all electrodes was crucial to avoid electrical interference from the stepper motors.

5.2.4 Scanning Electrochemical Microscopy and Leveling the Sample

Minimizing the tilt of the sample is crucial, as the analyte collection efficiency of the scanning probe varies with height above the sample (*vide infra*). To adjust the tilt of the wafer, the electrochemical cell was placed atop a plane balanced on three set screws, which allowed for adjustments in two orthogonal directions. To determine whether the sample is tilted relative to the probe, a means of determining the probe – sample separation is required. Initially, we attempted to use the transit time technique discussed in the next section, but decided to use that technique for determination of the SDEMS tip height only. To level the sample, a scanning electrochemical microscopy (SECM) tip was employed. This consisted of a Pt wire, 25 µm in diameter, sealed in glass, which was abraded down to a truncated conical shape, leaving a Pt disk exposed at the end, surrounded by less than about 250 µm of glass in all directions. The ratio of

the radius of the glass at the tip, and the radius of the disk electrode is known as the RG value, and it is typically kept in the range of 2 to 10 for SECM tips.

When an SECM tip is brought within a few tip diameters of a substrate, it is possible to have negative or positive electrochemical feedback, meaning the tip current will decrease or increase as the tip approaches the substrate. Negative feedback results from hindrance of mass transport of the redox species of interest to the tip by the substrate. Negative feedback occurs when the substrate is inactive towards the redox species of interest, either due to irreversibility of the reaction at the tip, or due to the substrate being at a potential at which it cannot reverse the tip reaction. Insulating substrates will also give negative feedback. Positive feedback occurs when the substrate can reverse the electrochemical reaction occurring at the tip, allowing the redox mediator to shuttle charge between the tip and substrate. It is also possible to obtain a response intermediate between pure positive and pure negative feedback if the substrate is able to reverse the tip reaction, but not efficiently.

The current vs. tip height response is referred to as an approach curve. Electrochemical feedback has been modeled in detail, and equations have been derived numerically to fit approach curves.[22,23] In figure 5.2, in addition to approach curves to two different substrates, modeled positive and negative feedback curves are shown. In this experimental setup, O_2 was used as a redox mediator, as it avoided introduction of a foreign species which could affect the catalytic activity of the substrate. A sufficient solution concentration of O_2 was maintained by the passive diffusion from the environment. A Hg-modified Pt tip was used, as it is not as sensitive to poisoning as a pure Pt tip would be. This electrode catalyzed the 2 e^- reduction of O_2 to H_2O_2, rather than the 4 e^- reduction to H_2O. The substrate was left at open circuit when approaching it with the SECM tip. For a test pattern of Pt surrounded by Ta_2O_5, negative

feedback was obtained when approaching areas covered with Ta_2O_5, but intermediate feedback was obtained over Pt covered areas. The decomposition of H_2O_2 to H_2O and O_2 can be chemically catalyzed by several materials, including platinum. It is also possible for the substrate to simultaneously oxidize tip-generated H_2O_2 back to O_2, while reducing O_2 at another location on the substrate.[24] Due to these complications, the tilt corrections were carried out at a location of the wafer not covered with catalyst. The differences in reactivity of the substrate towards H_2O_2 can also be imaged, as is shown in figure 5.2b.

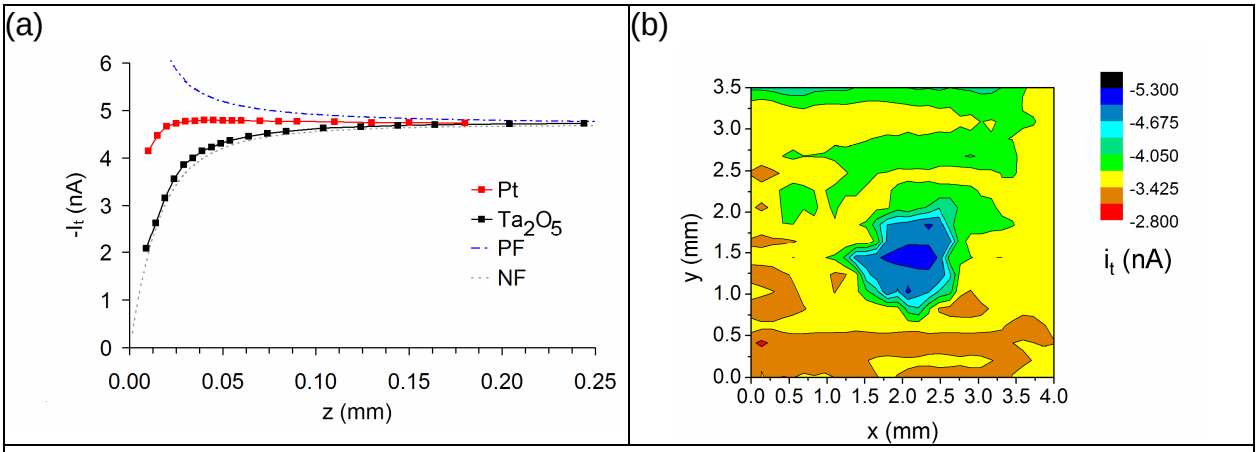

Figure 5.2: (a) Approach curves for a Hg – modified Pt tip over Pt and Ta_2O_5 regions of a wafer surface in O_2 – containing 0.1 M H_2SO_4. Simulated approach curves for positive feedback (PF) and negative feedback (NF) are plotted in dashed lines (assuming RG = 10). (b) SECM image of a 1 mm Pt spot test pattern, surrounded by Ta_2O_5, using the tip shown in (a). Tip height: ~30 µm; scan rate: 0.05 mm/s; x increment: 0.2 mm

5.2.5 Determination of the membrane inlet tip height

Maintaining the SDEMS tip at a consistent height over the sample is important, as the collection efficiency for electrogenerated species varies with the tip height. To determine the height, a method in which the time delay between the electrochemical generation of H_2 and its mass spectrometric detection, was developed. The potential of the substrate was stepped to a potential sufficiently negative for the evolution of H_2 for a 2s duration, and then stepped back to a potential at which H_2 was no longer evolved (figure 5.3). The mass spectrometric response to

this perturbation was a sharp initial rise, followed by a more gradual decrease. Plotting the square root of the time delay from the beginning of the potential step to the peak mass spectrometric H_2 current against the tip height yields a linear trend. A similar trend is also obtained using the time delay from the beginning of the potential step to the onset of mass spectrometric H_2 detection, though this point was not as easily discernable as the height. Air currents in the room created significant scatter in the data, so the cell was placed in an enclosure to avoid this.

This height calibration procedure was also tested with CO_2 generated from formic acid oxidation during 2 s potential steps. It was found the baseline of the mass spectrometric current increased with successive steps, which is likely due to the accumulation of CO_2 in the diffusion layer. This did not occur with H_2 because the substrate was able to reoxidize it after being returned to more positive potentials. The shape of the mass spectrometric response is in part determined by the growth and consumption of the diffusion layer by the substrate, as well as the formation of a depletion region by the membrane inlet tip.

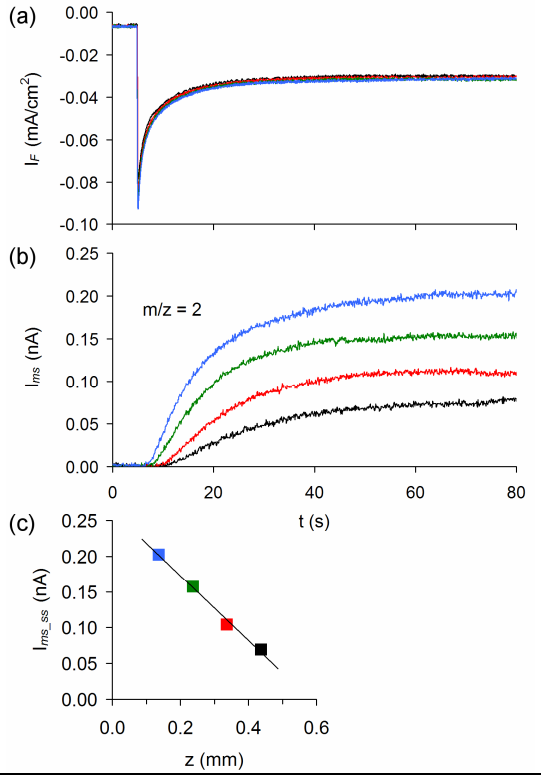

Figure 5.3: Fardaic currents (a) and corresponding H_2 mass spectrometric currents (b) for four different tip – substrate distances. The variation of the mass spectrometric current at 60 s is plotted against the separation in (c).

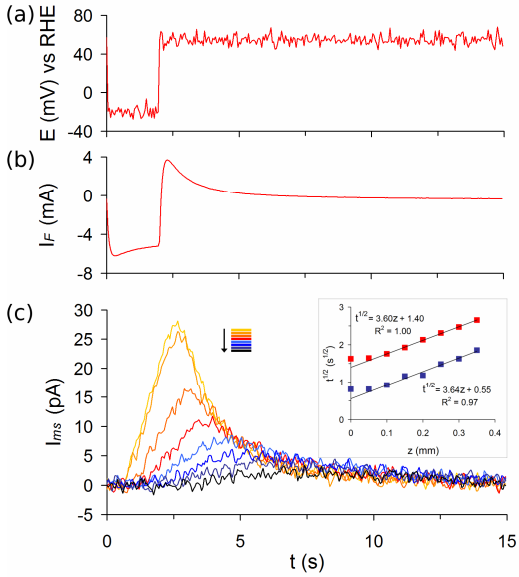

Figure 5.4: Calibration of the membrane inlet tip using the transit time of substrate generated H_2. The substrate potential (a), Faradaic current (b), and mass spectrometric H_2^+ (m/z = 2) current are all plotted over time. Mass spectrometric currents are shown for several tip – substrate separations, with the arrow next to the legend pointing towards increasing separation. Square root of time delays to the onset and to the peak H_2^+ current vs. separation are plotted in the inset in (c).

Such "transit time" or "time-of-flight" experiments have been employed previously, though with electrochemical detection, for the determination of the height of a scanning electrochemical microscope tip[17] and for determination of diffusion coefficients using microelectrodes at fixed separation,[25] or rotating ring-disk electrodes. A problem which can arise in these cases, however, is that the large double-layer charging current and Faradaic current

associated with stepping the working electrode potential can couple with the detecting electrode, producing a transient in the detector current, complicating interpretation of its response.[17]

It was found that the time delay did not depend on the H_2 evolution current. This is important, as different materials support different H_2 evolution current densities at a given potential. While this does limit the technique to materials that support a detectable H_2 evolution current at reasonable potentials, many of the materials under examination do.

One variation on this technique we tested was to apply a small sinusoidal signal to the potential of the working electrode in the H_2 evolution range, and then measure the phase difference between the Faradaic current and the mass spectrometric current. The time response of the system was too slow for this method to be of practical use, however.

It was found that the electrochemical surface area of the substrate, as determined from the hydrogen adsorption/desorption charge, decreased and the open circuit potential increased while developing the tip height calibration procedure. Upon scanning to more positive potentials, peaks associated with the formation and reduction of Au - oxide were observed. To compensate the H^+ reduction current at the working electrode, the counter electrode must pass an oxidative current. For very large reduction currents at the working electrode, the counter must go to potentials at which water oxidizes, and at which some Au can dissolve. The dissolved Au can then deposit on the working electrode. In general, this is more likely to give a false negative result in screening, rather than a false positive result, as Au has generally been found to have low activity for SOM electrooxidation in acidic media. The transit time technique can still be used, but it should be done to a limited extent.

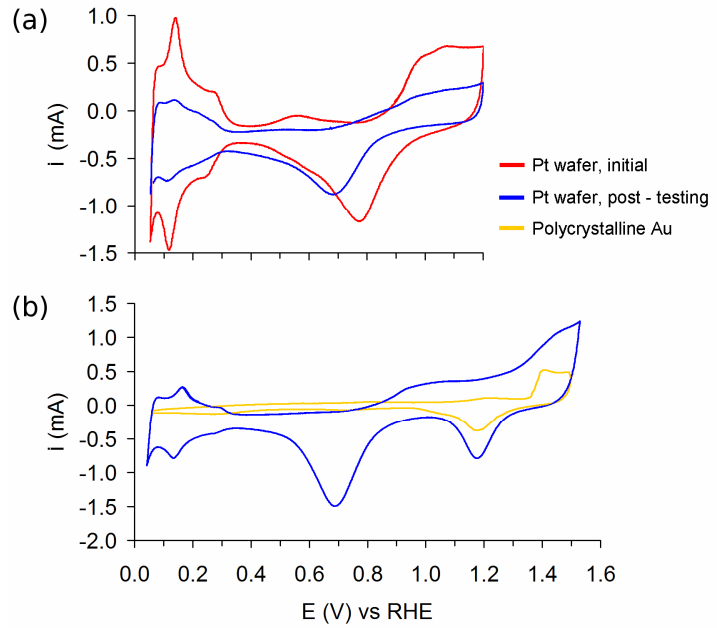

Figure 5.5: CVs of a wafer sputtered with only Pt, showing decrease in Pt surface area during development of tip height calibration procedure (a). A CV of the same wafer, but with a more positive potential limit, showing Au oxide peaks, and a CV of polycrystalline Au for comparison (b).

If the probe diameter could be made small enough, and the leak rates at locations other than the tip were small enough, it might also be possible to operate the membrane inlet tip in a negative feedback mode. This would employ a gas not involved in any chemical or electrochemical reaction at the surface, such as Ar or He. This method would be analogous to the negative feedback used in SECM or in the scanning probe system described by Li et al.[9,10]

5.3 RESULTS AND DISCUSSION

5.3.1 Scanning Test Patterns

To test the resolution of the scanning tip, a wafer with a 10 mm x 10 mm square of Pt was prepared. This was done by first sputtering a Ta adhesion underlayer, and then covering it with an Al foil mask, through which Pt was sputtered. One mass spectrometric image for H_2^+ (m/z = 2) was collected while holding the substrate at a potential in the hydrogen evolution range, while the other, for CO_2^+ (m/z =44), was collected during formic acid electrooxidation. It can be

seen that the mass spectrometric image corresponds fairly well to the Pt pattern, though there is some distortion. The alternate protrusions on either side of the square are due to the solution being dragged by the tip as it moves. In both images, there is also a fairly high signal off to the lower left of the square. This may arise from convection currents in solution. This problem was lessened to some extent by enclosure of the cell to shield it from ambient air currents.

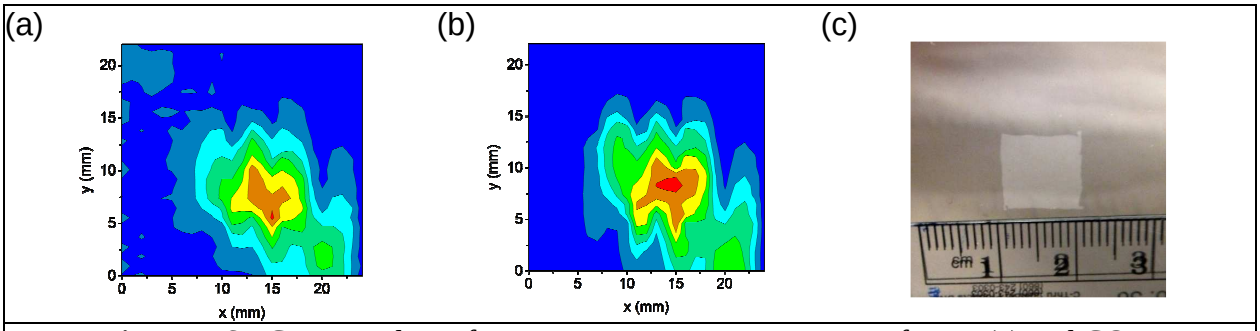

Figure 5.6: Contour plots of mass spectrometric ion currents for H_2 (a) and CO_2 (b) detected while rastering the SDEMS tip over the surface of a patterned wafer, with a 10 mm x 10 mm Pt square surrounded by Ta. For (a), the substrate was set at -0.010 V vs RHE to evolve H_2 ($i_{substrate}$ ~ -20 µA). For (b), a 0.5 M formic acid solution in 0.1 M H_2SO_4 was used, and the substrate current was galvanostatically controlled at 150 µA. Tip height: ~150 µm; Scan rate: 0.2 mm/s; x increment: 2 mm. An optical image of the patterned wafer is shown in (c).

In later measurements, this problem was lessened and the resolution improved by decreasing the outer diameter of the tip. The diameter of the probe was decreased by attaching a short length of glass capillary tubing to the end of the stainless steel taper. The capillary was attached with heat shrink tubing, and the end was covered with Teflon pipe tape. It might be expected that is would cause a time delay in the response due to the introduction of ineffectively pumped dead space, but this did not seem to be the case.

5.3.2 Stationary Tip Measurements and Comparison to Fluorescence Testing Results

Though the SDEMS is primarily intended as a scanning instrument, it can also be operated in stationary mode. The tip position is held constant while the substrate potential is

swept. When a potential is applied to the composition spread, the measured Faradaic current response sums over all compositons on the wafer. The response of the tip, however, corresponds only to areas within the diffusion length of the tip, which would be approximately 0.15 cm at the end of a 10 minute potential sweep, assuming $D_{CO_2} = 1.8 \times 10^{-5}$ cm^2/s.[26] In reality, the tip may sample a larger radius, due to solution convection arising from air currents, vibrations, and slight temperature changes.

As a test sample, a wafer sputtered only with Pt was used. In this case, the Faradaic current and mass spectrometric current should coincide closely. Formic acid, methanol and ethanol were tested, and the results for methanol are shown in figure 5.7. It can be seen that there is some lag, but this is expected from time required to reach a steady state observed in potential step experiments. For methanol, CO_2 and methyl formate are observed as products, while for ethanol, the only observed product was acetaldehyde. This does not necessarily mean that no CO_2 was produced from ethanol, but that there is too little to detect.

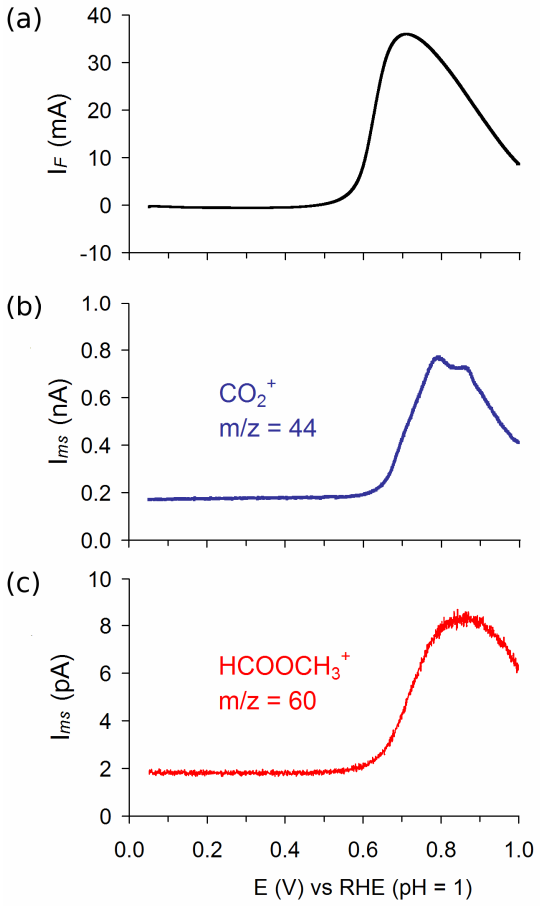

Figure 5.7: SDEMS, stationary tip mode measurement of the electrooxidation of 1.0 M methanol at a Pt wafer, showing Faradaic (a), and mass spectrometric CO_2^+ (b) and methyl formate (c) currents. 0.1 M H_2SO_4; tip height: 150 µm; scan rate: 1 mV/s

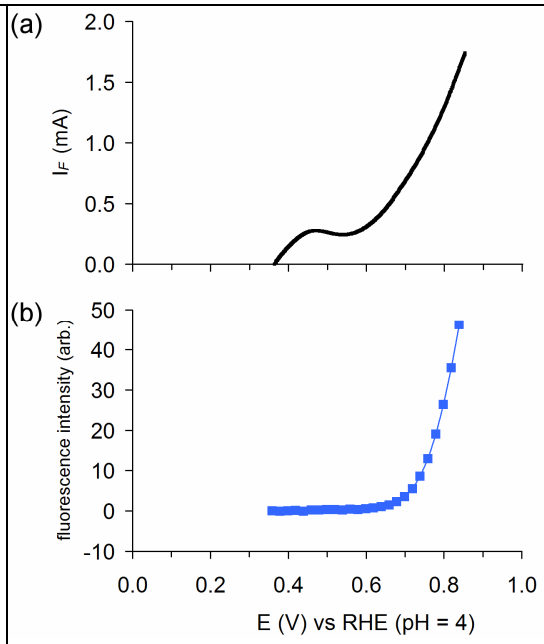

Figure 5.8: Faradaic oxidation current for 3.0 M methanol (a) and corresponding quinine fluorescence (b). 0.1 M KO_3SCF_3; scan rate: 5 mV/s; imaging interval: 4 s

For comparison, results obtained with the fluorescence assay setup are shown for methanol, in figure 5.8. These measurements were made using a Ag/AgCl reference electrode, but have been converted to a RHE scale for pH = 4, as this would be the approximate surface pH once intense fluorescence is observed. It is somewhat difficult to define a potential scale in this case, as the pH at the surface of the electrode decreases during the sweep. The observed fluorescence intensity and Faradaic currents observed are somewhat displaced from those in the SDEMS, likely due to the changing potential scale.

5.3.3 Preferential orientation of combinatorial libraries

One other feature to note about combinatorial libraries is that the method of production of the samples can lead to preferential exposure of certain crystal facets. From the cyclic voltammogram of the Pt sputtered wafer shown in figure 5.5, it can be seen that the hydrogen adsorption peaks resemble those of a surface with relatively large (111) terraces with monatomic steps.[27] This is also supported by the relatively broad peak at +0.55, which likely corresponds to (bi)sulfate adsorption on the (111) terraces, and is related to the "butterfly" feature observed for (111) surfaces with a very low step density. This preferential orientation is important to note, as electrochemical activity strongly depends upon the orientation of the surface. The Pt (111) surface tends have a more negative onset potential for the electrooxidation of several different small organic molecules, including formic acid, formaldehyde, methanol and dimethoxymethane.[28-31] The onset potential of methanol oxidation observed here is about 60 mV more negative than that observed for polycrystalline Pt in a separate experiment, though that experiment was carried out at a faster sweep rate and in a flow cell.

5.4 ONGOING AND FUTURE WORK

5.4.1 Modifications to the SDEMS Probe

It would be desirable to further decrease the size of the SDEMS probe. As was mentioned earlier, this has been achieved by affixing a capillary to the end of the probe. The size of the capillary can be further decreased using a pipette puller. As the diameter of the capillary approaches the thickness of the membrane, this will become problematic, however. It may be possible to do without the membrane if a thin, porous hydrophobic layer can be packed into the capillary tip.

5.4.2 Formic Acid Selective SECM Tip

A tip selective for the electrooxidation of formic acid (FA) might be considered for the study of methanol electrooxidation at combinatorial libraries. It is expected that this type of sensor would only be qualitative, as derivation of concentration data from the current response of the tip is not likely to be straightforward. Several approaches towards preparation of a FA selective tip might be considered.

One candidate material for FA sensing is Pd, which has significantly higher activity for FA than for methanol or formaldehyde in the low potential range. The use of bulk Pd might be complicated by the formation of a Pd – hydride phase at the low potentials at which this catalyst is selective for FA. A possible alternative would be a Pd monolayer catalyst on a Au or Pt substrate. This could be prepared using the method developed by Adzic et al., in which a monolayer of copper is formed on the substrate electrode by underpotential deposition. The electrode is then placed in a solution containing the oxidized form of a second metal with a redox potential more positive than that of copper, in this case Pd. The second metal can then oxidatively displace Cu spontaneously, forming a metallic monolayer of the second element.[32] This process is commonly referred to as "galvanic displacement."

Another approach would be to modify a Pt tip with Pb or Bi. The enhancement in the activity of Pt towards formic acid by modification with these elements has been well established in the literature.[33-35] Modification with these elements can be carried out with solutions containing ions of these metals. Bismuth will spontaneously undergo irreversible adsorption on Pt from solutions of Bi^{3+}, possibly by a coupling between the reduction of Bi^{3+} and formation of a Pt surface oxide.[36] Lead will also undergo irreversible adsorption, but the adlayer is less stable than that formed from Bi.[37] It has also recently been demonstrated that electrodeposition of the ordered intermetallic PtPb, a highly active formic acid oxidation catalyst,[38] can be carried out.[39]

An additional modification, which might further increase the sensitivity and possibly selectivity for oxidation of FA, would be to preferentially orient the microelectode to preferentially expose the Pt (111), which has the highest activity of the low index planes for FA oxidation at low potentials. Single crystal ultramicroelectrodes of Au and Pt have been reported, but they are not readily fabricated.[40,41] Arvia et al. published a series of papers in the 1980's reporting a technique by which Pt electrodes could be modified to preferentially expose a particular crystal plane by the application of a high frequency potential waveform.[42] Several square and triangular wave forms with varying frequencies were tested, and it was found that preferential exposure of particular planes could be obtained depending on the upper and lower potential waveform, as well as the frequency. In preliminary tests, we were able to produce some preferential (111) orientation, though with a very large roughness factor. As long as the surface does not become recessed inside of the glass sheath by this etching procedure, the large roughness would be helpful in terms of increasing the tip current.

5.5 CONCLUSIONS

A combined SDEMS – SECM has been developed for the analysis of combinatorial libraries of electrocatalysts. Protocols for leveling the sample and calibrating the SDEMS tip height have been developed. The SDEMS can be operated in stationary mode, while the substrate potential is varied, tracking localized product formation as the potential is swept. It can also be rastered to spatially resolve product formation at the substrate at a fixed potential. The resolution of the SDEMS tip is approximately 2 mm, but this will be improved with further modifications to the tip. As of yet, the SECM has only been used for purposes of leveling the sample, but could be used to image product formation if a selective tip material is chosen.

5.6 REFERENCES

(1) Prochaska, M.; Jin, J.; Rochefort, D.; Zhuang, L.; DiSalvo, F. J.; Abruna, H. D.; van Dover, R. B. *Rev. Sci. Instrum.* **2006**, *77*.

(2) Gregoire, J. M.; van Dover, R. B.; Jin, J.; DiSalvo, F. J.; Abruna, H. D. *Rev. Sci. Instrum.* **2007**, *78*.

(3) Gregoire, J. M.; Tague, M. E.; Smith, E. H.; Dale, D.; DiSalvo, F. J.; Abruña, H. D.; Hennig, R. G.; van Dover, R. B. *J. Phys. Chem. C* **2010**, *114*, 21664-21671.

(4) Miura, A.; Tague, M. E.; Gregoire, J. M.; Wen, X.-D.; van Dover, R. B.; Abruña, H. D.; DiSalvo, F. J. *Chem. Mater.* **2010**, *22*, 3451-3456.

(5) Reddington, E.; Sapienza, A.; Gurau, B.; Viswanathan, R.; Sarangapani, S.; Smotkin, E. S.; Mallouk, T. E. *Science* **1998**, *280*, 1735-1737.

(6) Allen, R. I.; Box, K. J.; Comer, J. E. A.; Peake, C.; Tam, K. Y. *J. Pharm. Biomed. Anal.* **1998**, *17*, 699-712.

(7) Cong, P. J.; Doolen, R. D.; Fan, Q.; Giaquinta, D. M.; Guan, S. H.; McFarland, E. W.; Poojary, D. M.; Self, K.; Turner, H. W.; Weinberg, W. H. *Angew. Chem.-Int. Edit.* **1999**, *38*, 484-488.

(8) Weinberg, W. H.; McFarland, E. W.; Cong, P.; Guan, S.; Symyx Technologies: United States, **1999**, Patent no. 5,959,297.

(9) Li, N.; Eckhard, K.; Assmann, J.; Hagen, V.; Otto, H.; Chen, X.; Schuhmann, W.; Muhler, M. *Rev. Sci. Instrum.* **2006**, *77*, 084102-7.

(10) Li, N.; Assmann, J.; Schuhmann, W.; Muhler, M. *Anal. Chem.* **2007**, *79*, 5674-5681.

(11) Roos, M.; Kielbassa, S.; Schirling, C.; Haring, T.; Bansmann, J.; Behm, R. J. *Rev. Sci. Instrum.* **2007**, *78*.

(12) Modestov, A. D.; Srebnik, S.; Lev, O.; Gun, J. *Anal. Chem.* **2001**, *73*, 4229-4240.

(13) Jambunathan, K.; Hillier, A. C. *J. Electrochem. Soc.* **2003**, *150*, E312-E320.

(14) Jambunathan, K.; Jayaraman, S.; Hillier, A. C. *Langmuir* **2004**, *20*, 1856-1863.

(15) Gao, Y.; Tsuji, H.; Hattori, H.; Kita, H. *J. Electroanal. Chem.* **1994**, *372*, 195-200.

(16) Wonders, A. H.; Housmans, T. H. M.; Rosca, V.; Koper, M. T. M. *J. Appl. Electrochem.* **2006**, *36*, 1215-1221.

(17) Bard, A. J.; Fan, F. R. F.; Kwak, J.; Lev, O. *Anal. Chem.* **1989**, *61*, 132-138.

(18) Shah, B. C.; Hillier, A. C. *J. Electrochem. Soc.* **2000**, *147*, 3043-3048.

(19) Jayaraman, S.; Hillier, A. C. *J. Comb. Chem.* **2003**, *6*, 27-31.

(20) Jung, C.; Sánchez-Sánchez, C. M.; Lin, C.-L.; Rodríguez-López, J.; Bard, A. J. *Anal. Chem.* **2009**, *81*, 7003-7008.

(21) Lin, C.-L.; Rodríguez-López, J.; Bard, A. J. *Anal. Chem.* **2009**, *81*, 8868-8877.

(22) Bard, A. J.; Faulkner, L. R. *Electrochemical methods: fundamentals and applications, 2nd ed.*; 2nd ed.; Wiley: New York, 2001.

(23) Bard, A. J.; Mirkin, M. V. *Scanning electrochemical microscopy*; Marcel Dekker: New York, NY, 2001.

(24) Fernández, J. L.; Hurth, C.; Bard, A. J. *J. Phys. Chem. B* **2005**, *109*, 9532-9539.

(25) Licht, S.; Cammarata, V.; Wrighton, M. S. *J. Phys. Chem.* **1990**, *94*, 6133-6140.

(26) Lide, D. R. *CRC Handbook of Chemistry and Physics*; 90 ed.; CRC Press (Taylor and Francis): Boca Raton, FL, 2009.

(27) Mostany, J.; Herrero, E.; Feliu, J. M.; Lipkowski, J. *J. Phys. Chem. B* **2002**, *106*, 12787-12796.

(28) Lamy, C.; Leger, J. M.; Clavilier, J.; Parsons, R. *Journal of Electroanalytical Chemistry and Interfacial Electrochemistry* **1983**, *150*, 71-77.

(29) Herrero, E.; Franaszczuk, K.; Wieckowski, A. *J. Phys. Chem.* **1994**, *98*, 5074-5083.

(30) Batista, E. A.; Iwasita, T. *Langmuir* **2006**, *22*, 7912-7916.

(31) Kéranguéven, G.; Berná, A.; Sibert, E.; Feliu, J. M.; Léger, J. M. *Electrochim. Acta* **2008**, *54*, 394-402.

(32) Brankovic, S. R.; Wang, J. X.; Adzic, R. R. *Surf. Sci.* **2001**, *474*, L173-L179.

(33) Adzic, R. R.; Simic, D. N.; Despic, A. R.; Drazic, D. M. *Journal of Electroanalytical Chemistry and Interfacial Electrochemistry* **1975**, *65*, 587-601.

(34) Shibata, M.; Motoo, S. *J. Electroanal. Chem.* **1985**, *188*, 111-120.

(35) Smith, S. P. E.; Ben-Dor, K. F.; Abruña, H. D. *Langmuir* **1999**, *15*, 7325-7332.

(36) Clavilier, J.; Feliu, J. M.; Aldaz, A. *J. Electroanal. Chem.* **1988**, *243*, 419-433.

(37) Clavilier, J.; Orts, J. M.; Feliu, J. M.; Aldaz, A. *Journal of Electroanalytical Chemistry and Interfacial Electrochemistry* **1990**, *293*, 197-208.

(38) Casado-Rivera, E.; Volpe, D. J.; Alden, L.; Lind, C.; Downie, C.; Vázquez-Alvarez, T.; Angelo, A. C. D.; DiSalvo, F. J.; Abruña, H. D. *J. Am. Chem. Soc.* **2004**, *126*, 4043-4049.

(39) Hwang, S.-M.; Bonevich, J. E.; Kim, J. J.; Moffat, T. P. *J. Electrochem. Soc.* **2011**, *158*, D307-D316.

(40) Komanicky, V.; Fawcett, W. R. *Anal. Chem.* **2003**, *75*, 4534-4540.

(41) Komanicky, V.; Fawcett, W. R. *J. Electroanal. Chem.* **2003**, *556*, 109-115.

(42) Visintin, A.; Canullo, J. C.; Triaca, W. E.; Arvia, A. J. *Journal of Electroanalytical Chemistry and Interfacial Electrochemistry* **1988**, *239*, 67-89.

CHAPTER 6

Fuel Cell Testing of $Pt/Ti_{0.7}W_{0.3}O_2$ as a CO Tolerant Anode Catalyst

6.1 INTRODUCTION

6.1.1 Doped Metal Oxides as Support Materials

The catalysts utilized in H_2/O_2 fuel cells generally consist of catalyst nanoparticles disbursed on a support material, which prevents agglomeration of the catalyst, which would decrease the available surface area. Most commonly, carbon is employed as a support, even though it is not thermodynamically stable above +0.207 V vs NHE. Under moderate operating conditions, the potential of the anode should be close to 0 V, assuming a sufficient amount of catalyst is used for the anode reaction not to be the limiting factor. The cathode potential will be in the 0.6 to 0.85 V range at moderate loads, but at open circuit, its potential can be higher than 1 V. During startup and shutdown, however, when air is present in the anode, potentials as high as 1.2 V can be reached, and carbon corrosion is rapid.[1]

Corrosion of the carbon support can lead to degradation of the cell performance over time. For this reason, support materials with higher oxidative stability are desirable. Recently, materials of the class $Ti_{1-x}W_xO_2$, particularly with $x = 0.3$, have been investigated as catalyst support materials.[2,3] While rutile TiO_2 is expected to be highly stable over a wide potential range,[4] it is a semiconductor with a band gap of over 3 eV, making its conductivity too low for use as a catalyst support. By doping it with a sufficient amount of WO_2, which still has two free valence electrons, the conductivity can be significantly increased. While the Pourbaix diagram of W indicates that the thermodynamic window of potential stability for WO_2 ranges from about -0.1 to 0.0 V vs RHE,[4] it is possible that the material is kinetically stable.

6.1.2 CO Tolerance of Pt/$Ti_{0.7}W_{0.3}O_2$

Aside from stability, platinized $Ti_{0.7}W_{0.3}O_2$ is also of interest for its CO tolerant properties. It was recently shown, using rotating disk electrode (RDE) voltammetry, that Pt/$Ti_{0.7}W_{0.3}O_2$ demonstrated a much more negative onset potential for oxidative current in acidic solutions bubbled with 2% CO in H_2 than either PtRu or Pt.[5] Currently, PtRu is considered to be the best catalyst for CO tolerance. It is thought that the presence of Ru on the surface provides the adsorbed oxide species required to oxidize CO at lower potentials.

It has been known at least since the 1960's that the presence of WO_x (x = 2 to 3) or Na_yWO_3 (tungsten bronze, y = 0 to 1) in a fuel cell can yield improved CO tolerance.[6,7] Other W – containing fuel cell materials have also shown CO tolerance, such as a Pt – WO_x material produced by reduction of chloride precursors, Pt/C impregnated with phosphotungstic acid,[8] and Pt supported on WO_3.[9] Similar CO tolerant properties have also been obtained for some Mo containing materials, such as a $Pt_{0.7}Mo_{0.3}$ alloy,[10] and MoO_x – modified Pt.[11,12] We have also found that nanoparticles of the Pt_2Mo ordered intermetallic compound displayed enhanced CO tolerance. It has been shown using DEMS that modification of Pt with WO_x or MoO_x can shift the electrooxidation of some adsorbed CO to potentials significantly more negative than for pure Pt.[13,14] It was found that interaction of the $Ti_{0.7}W_{0.3}O_2$ support with Pt also enabled it to oxidize some CO at low potentials.[5] While it is not immediately apparent from the Faradaic current, a small amount of adsorbed CO is oxidized at potentials as low as +0.2 to +0.3 V vs RHE. The removal of this small amount of CO from the surface appeared to be enough to begin oxidizing H_2 at near its mass transport limited rate at about +0.4 V. This behavior seems to be associated with a negative shift in the CO elctrooxidation pre – peak, which will be discussed later in this chapter.

6.1.3 Differences Between Fuel Cell Testing and RDE Measurements

Although these results are highly promising, it is important to confirm these results under real fuel cell operating conditions. One significant difference is the ionic environment: in the RDE measurements, the supporting electrolyte was 0.1 M H_2SO_4, while in the fuel cell it was Nafion, and the differing adsorption properties of the anions in these electrolytes can affect electrocatalysis. The adsorption strength of Nafion appears to lie somewhere between those of ClO_4^- and $(H)SO_4^-$.[15] The differing anionic species could also affect the solubility of cationic species dissolving from the catalyst, which could lead to decreased stability. If the catalyst surface oxidizes and leaches metal cations, these may precipitate on the surface if they form an insoluble compound with the anions in solution. If the compound formed is soluble, the cations could then diffuse away from the electrode. The fact that the anions are tethered to the membrane is also expected to affect the characteristics of the electrochemical double layer.

Another significant difference between the fuel cell and RDE testing environments is the transport properties. In the RDE setup, diffusion and convection only occur in the liquid phase. In the fuel cell, a so called three phase boundary exists between the electrode, a gas phase reactant and solution. Transport in the gas phase can make significant contributions in this arrangement. As an example of this, when H_2 with 100 ppm of CO is run though a fuel cell anode, a high CO coverage on the catalyst is attained within minutes. On the same time scale in RDE testing, only small changes are apparent. This suggests the rate at which CO impinges on the surface is lower in the RDE testing conditions. For this reason, RDE experiments are carried out with higher CO concentrations. Another aspect of the RDE setup to consider is that the solution remains the same throughout the experiment, and if species dissolve from the electrode, they will accumulate in solution. In the case of the fuel cell, it may be possible for anionic and

neutral degradation products to leave the cell with excess water (either produced in O_2 reduction, or from the humidifiers).

Two other differing aspects of these experimental setups are the timescale of the experiment and the temperature. Fuel cell measurements can last 10's to 1000's of hours, while RDE experiments are usually only a few minutes. Also, RDE experiments are usually conducted at room temperature, while fuel cell testing is generally carried out at elevated temperatures.

In light of these differences, we have tested $Pt/Ti_{0.7}W_{0.3}O_2$ as a CO tolerant anode material under fuel cell operating conditions, and compared its performance with Pt/C and PtRu/C under comparable conditions. The results of this investigation are described herein.

6.2 METHODLOGY

Cell preparation methods are described in detail in the chapter II. The same 5 cm^2 serpentine flow field was used for all tests, and currents were normalized to the geometric area. The cathode catalyst, ETek Pt/C 50% at 0.4 mg/cm^2, was kept the same for all tests. The Pt/C 50% and PtRu/C 50% (1:1 atomic ratio) anode catalysts were also obtained from ETek, and were used at 0.4 mg/cm^2 loading. Preparation of the $Pt/Ti_{0.7}W_{0.3}O_2$ catalyst is described in a previous publication.[5] Each cell was prepared with a Nafion 117 membrane. The polarization curves have been plotted with cell voltage as the x – axis to facilitate comparison with the RDE data.

6.3 RESULTS AND DISCUSSION

6.3.1 Interaction of Pt with the support material

The cyclic voltammogram of $Pt/Ti_{0.7}W_{0.3}O_2/C$ suggests a significant interaction between the support and Pt figure 6.1. The typical hydrogen adsorption peaks are not visible, being obscured by a broad peak at about +0.27 V in the anodic sweep and +0.17 V in the cathodic

sweep. The CV looks similar to that obtained for Pt in solutions containing Na_2WO_4. It may be that WO_x species dissolve from the support material and deposit on the Pt nanoparticles.

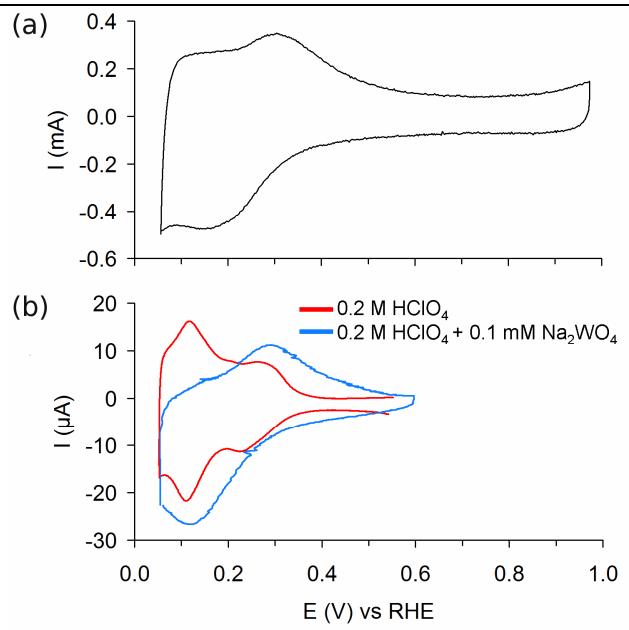

Figure 6.1: Cyclic voltammogram of $Pt/Ti_{0.7}W_{0.3}O_2/C$ 17% in 0.1 M H_2SO_4 (a), and of a 5 mm polycrystalline Pt disk electrode in 0.2 M $HClO_4$ with and without 0.1 mM Na_2WO_4 in solution (b). Scan rate: 50 mV/s

It has been suggested that the interaction of WO_x with the Pt surface is an underpotential deposition (UPD) process.[13] UPD is the electrodeposition of a monolayer of one metal on another at a potential more positive than that of bulk deposition, and occurs due to a negative Gibbs free energy for the interaction between the adsorbate and substrate. Kolb et al. studied the UPD of several different pairs of metals, and showed a linear trend between the difference in work functions of the two metals ($\Delta\Phi$) and the potential separation of UPD and bulk deposition (ΔU).[16]

$$\Delta U = \left(0.5\frac{V}{eV}\right)\Delta\Phi$$

The work function of polycrystalline Pt has been reported as 5.40 eV and that of polycrystalline W as 4.55 eV,[17] suggesting that UPD would take place about 0.4 V more positive than the onset

of bulk deposition. The potential range of stability for metallic W begins at about -0.1 V, so UPD might be expected to occur at +0.3 V, which is approximately the peak position in the anodic sweep.

The UPD explanation does not quite seem to fit the behavior seen here, though, since the species does not seem to dissolve from the surface as the potential is swept through the peak in the anodic direction. It is clear from the suppression of the surface oxide formation and reduction peaks that the W species is still adsorbed even at far more positive potentials. Another characteristic which would seem to discount the W UPD explanation is Cu can still undergo UPD on Pt surfaces already modified with WO_x (derived from WC), and the Cu_{UPD} stripping peak position is not radically altered.[18] Given the work function differences, Cu would not be expected to undergo UPD on a W coated surface.

Another possible explanation of the features in the voltammogram may be the deposition of an insoluble, redox active WO_x film on the Pt surface. The formation of films on Pt electrodes in acidic solutions containing tungstate ions has been confirmed using scanning tunneling microscopy (STM) and X – ray diffraction (XRD). The XRD data revealed the presence of hydrogen – tungsten bronzes in the film.[19] It may also be that WO_x undergoes an irreversible adsorption process, akin to that of Bi, which forms an adsorbed oxide compound that can undergo a reversible redox process.[20]

6.3.2 Fuel Cell Testing

An MEA was prepared with a $Pt/Ti_{0.7}W_{0.3}O_2/C$ anode, and a Pt/C cathode (ETek), and Nafion as the membrane. It was helpful to add carbon to the anode catalyst ink, as the conductivity of the support material was insufficient to form electrical contact with much of the catalyst layer. A cell was prepared with the same amount of $Pt/Ti_{0.7}W_{0.3}O_2$, but without any

addition of carbon, and the capacitive and pseudocapacitive currents on the anode were much lower than with carbon added, suggesting low utilization of the catalyst.

In a controlled voltage cell polarization, the currents obtained using pure H_2 and pure O_2 were not as high as those obtained using a Pt/C or PtRu/C anode (figure 6.2a). This loss may at least in part be due to the lower weight loading of catalyst on the support, which necessitated a larger volume of material to be applied to the membrane to maintain the same precious metal loading. The increased thickness of the catalyst layer can impede transport of water and reactants, and can also lead to increased electronic and ionic resistance.

When H_2 with 100 ppm CO was used, the Pt/$Ti_{0.7}W_{0.3}O_2$ cell did show increased CO tolerance relative to Pt, but not PtRu (1:1), in the first polarization (figure 6.2b). On the second cycle, however, the polarization looked similar to that of the cell with the Pt anode. It was possible to restore the CO tolerant behavior by purging the anode of CO, and stripping the adsorbed CO from the surface.

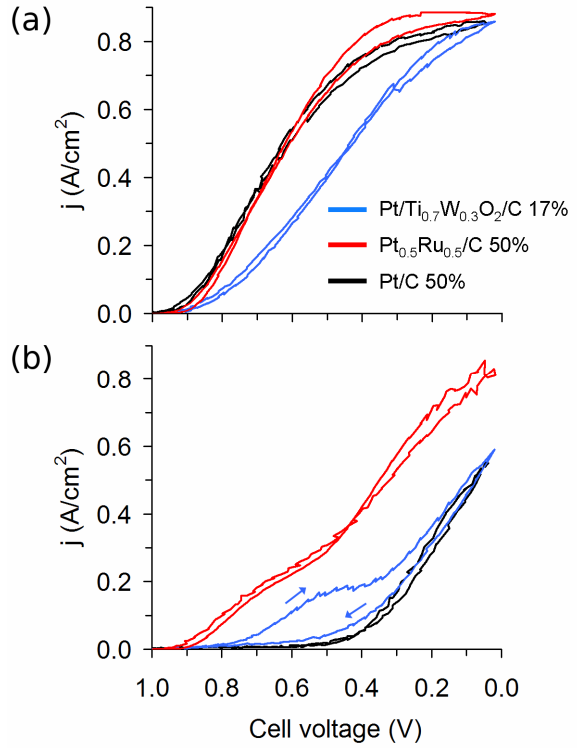

Figure 6.2: Controlled voltage polarization curves for fuel cells prepared with the anode catalysts noted in the legend with pure H_2 (a) and H_2 with 100 ppm CO (b) for the anode gas. For each, the Pt loading was All cells had Pt/C 50% from ETek at 0.4 mg_{Pt}/cm^2 for the cathode material. Membrane: Nafion 117; Cell temperature: 60° C; Anode and cathode humidifier temperature: 65° C; Anode flow rates: 50 sccm; Scan rate: 1 mV/s

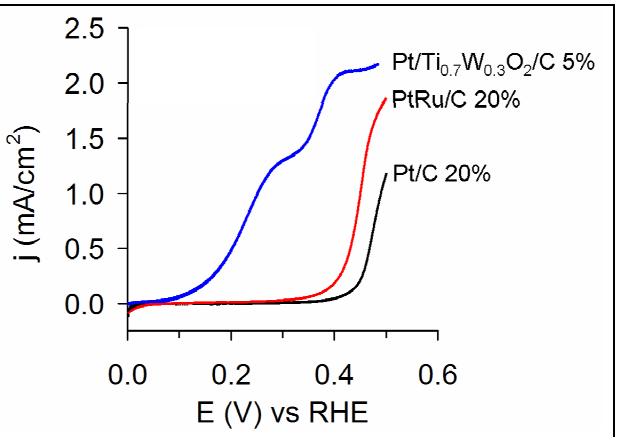

Figure 6.3: Linear sweep rotating disk electrode voltammograms of the different anode materials in 0.1 H_2SO_4 solution bubbled with H_2 with 2% CO. Currents are normalized the geometric surface area. 1600 rpm, 1 mV/s, 21° C. Data courtesy of Deli Wang.[5]

One possible explanation for the loss of CO tolerance after the first cycle may be dissolution of WO_x species from the surface at the potentials the anode must reach to oxidize CO. If the dissolution of WO_x frees Pt surface sites, CO could then occupy these sites, preventing the WO_x from redepositing.

Another possible explanation is that this behavior is similar to the so called “pre – peak” observed for pure Pt. The eletrooxidative stripping of CO from Pt occurs in two stages, the pre – peak and the main peak. The former represents a small fraction of the adsorbed CO that is

oxidized in a broad feature between about +0.4 and +0.65 V vs RHE, while the majority of the adsorbed CO is oxidized at a sharper feature at more positive potentials, usually in the +0.65 V to +0.85 V range. The origin of the pre – peak has received much attention in the literature, but it is generally thought to arise from defect sites, which can form surface oxide species at lower potentials than ordered regions of the surface.[21-23] The electrooxidation of CO is believed to occur via a Langmuir – Hinshelwood mechanism with and adsorbed oxygen species, often referred to as OH_{ads} (even though this might not be the true nature of the adsorbate.) The defect sites can provide the second reactant at more negative potentials, and thus allowing some of the CO adsorbate to be oxidized.

The important characteristic to note about the pre peak is that it occurs only when the CO adlayer forms below about +0.3 V. When it is formed at more positive potentials, little CO is oxidized at potentials below the main peak, leaving few sites free to oxidize H_2. It is not possible to recover the pre – peak by lowering the potential of an electrode which has already had CO adsorbed at higher potentials.[23] For comparison, figure 6.4 shows the voltammogram of polycrystalline Pt in H_2SO_4 solution bubbled with 2% CO in H_2, in the DEMS flow cell. Also shown are the corresponding mass spectrometric currents for H_2 and CO_2. The electrode was held at +0.05 V while introducing CO, so the pre – peak is present in the first cycle, and is visible in the CO_2 mass spectrometric current. The number of sites freed by the oxidation of CO in the pre – peak was sufficient for the oxidation of H_2 to reach a significant fraction of its mass transport limited current. When the potential passed the main peak, both CO and H_2 were oxidized at the mass transport limited rate. In the following cathodic sweep, the oxidation current decreased as the surface became poisoned with CO again. Much of the CO adlayer formed at more positive potentials, so the pre – peak was not observed in the second cycle, and

H_2 was not oxidized at a significant rate until potentials more positive than the main peak. Such might also be the case for the $Pt/Ti_{0.7}W_{0.3}O_2$, though with a more negative pre – peak position in this case.

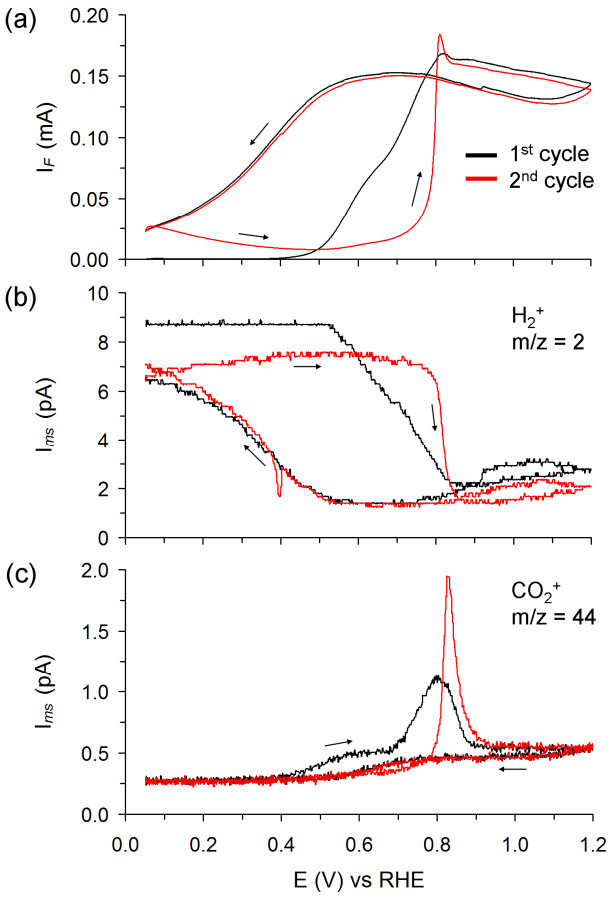

Figure 6.4: Cyclic voltammograms of a polycrystalline Pt disk electrode (6 mm diameter) in 0.1 M H_2SO_4, bubbled with 2% CO in H_2. Faradaic (a), and mass spectrometric H_2 (b) and CO_2 (c) currents. Scan rate: 10 mV/s; Flow rate: 15 µL/s; 21 ^oC

A comparison of the polarization curves collected at the beginning and end of a week of testing showed little difference, suggesting that $Pt/Ti_{0.7}W_{0.3}O_2$ was relatively stable (figure 6.5). The testing carried out over this week consisted of several polarization curves with pure H_2 and 100 ppm CO in H_2, with the majority of the time being taken up with a voltage hold at 0.52 V. A comparison of the cyclic voltammogram of the anode also showed little change over the week of

testing (figure 6.6a), but that of the cathode showed significant changes. It had taken on features resembling those of the anode, suggesting dissolution of WO_x species from the anode, and their subsequent transport through the membrane and deposition on the cathode (figure 6.6b). The identity of the WO_x species is not entirely clear, though it might be expected that they are neutral or cationic, given that it was able to permeate a cation exchange membrane. Pereira et al. observed similar WO_x crossover behavior when studying cells prepared with $PtWO_x/C$ and phosphotungstic acid impregnated Pt/C catalysts.[8] After the presence of the WO_x species at the cathode was known, the possibility of removing this species by holding the cathode at high potentials was tested. After holding at +1.0 V for 15 minutes, no major change was evident in the CV.

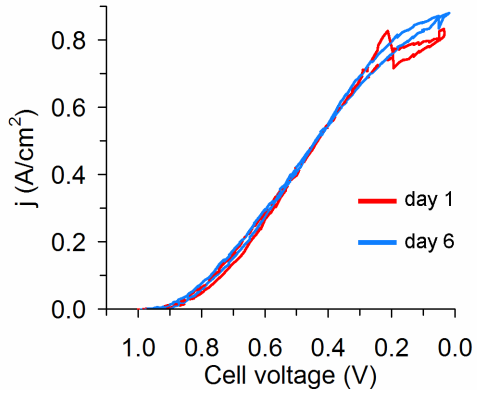

Figure 6.5: Cell polarization curves for the $Pt/Ti_{0.7}W_{0.3}O_2/C$, Pt/C cell obtained at the beginning of testing, and after running the cell for several days. Cell temperature 60° C; Humidifier temperature: 65° C; Anode: 50 sccm H_2; Cathode: 50 sccm O_2; Scan rate: 1 mV/s

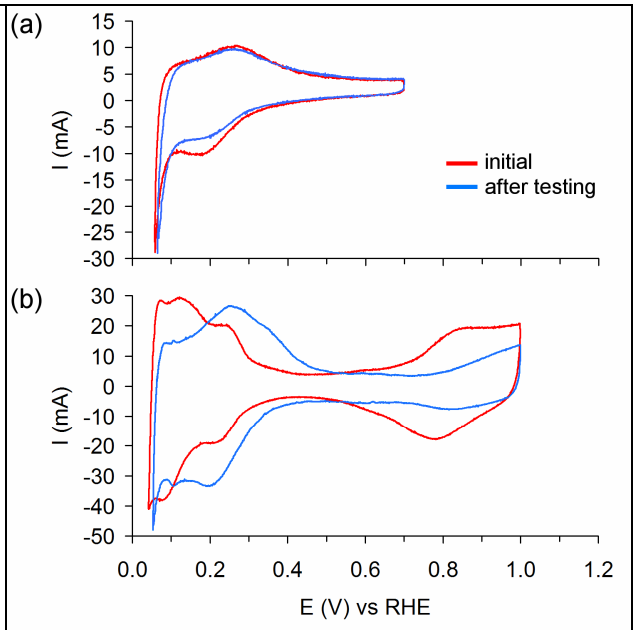

Figure 6.6: Cyclic voltammograms of the anode (a) and cathode (b) of the $Pt/Ti_{0.7}W_{0.3}O_2/C$ anode and Pt/C cathode described in figure 6.2, before and after testing. Cell temperature 60° C; Humidifier temperature: 65° C; Working electrode: 10 sccm N_2; Reference/Counter electrode: 100 sccm H_2; Scan rate: 20 mV/s

Dissolution and crossover of Ru has also been observed in DMFCs using PtRu as an anode material.[24,25] There, it was found that Ru crossover occurred under most conditions tested, including simply humidifying the cell without passing any current, as well as exposure of the anode to higher potentials.[24] It has also been noted that Co is leached from PtCo cathode catalysts under fuel cell operating conditions, and that the resulting Co^{2+} exchanged with protons in the membrane.[26] No mention was made regarding whether it deposited on the anode.

It is somewhat surprising that the overall cell performance was not strongly affected by such a large change at the surface of the cathode in this case. Though it is not generally the case for a H_2/O_2 fuel cell, it may be that the anode was limiting the cell performance, possibly due to the low density of catalytic sites in the anode layer.

6.4 CONCLUSIONS

The fuel cell performance of $Pt/Ti_{0.7}W_{0.3}O_2$ /C has been tested. There was some correspondence with the CO tolerant behavior observed for this material in H_2SO_4 solution at room temperature. The CO tolerance appeared to be transient in nature, however, appearing only for the first cell polarization cycle. It was possible to restore this behavior by totally removing the CO from its surface. The fuel cell performance showed only small changes over a week of testing, suggesting some stability, though dissolution and crossover of WO_x was apparent from the cyclic voltammogram of the cathode.

6.5 REFERENCES

(1) Mathias, M. F.; Makharia, R.; Gasteiger, H. A.; Conley, J. J.; Fuller, T. J.; Gittleman, C. I.; Kocha, S. S.; Miller, D. P.; Mittelsteadt, C. K.; Xie, T.; Yan, S. G.; Yu, P. T. *Electrochem. Soc. Interface* **2005**, *14*, 24-35.

(2) Subban, C. V.; Zhou, Q.; Hu, A.; Moylan, T. E.; Wagner, F. T.; DiSalvo, F. J. *J. Am. Chem. Soc.* **2010**, *132*, 17531-17536.

(3) Subban, C.; Zhou, Q.; Leonard, B.; Ranjan, C.; Edvenson, H. M.; DiSalvo, F. J.; Munie, S.; Hunting, J. *Philos. Trans. R. Soc., A* **2010**, *368*, 3243-3253.

(4) Pourbaix, M. *Atlas of electrochemical equilibria in aqueous solutions*; National Association of Corrosion Engineers: Houston, TX, 1974.

(5) Wang, D.; Subban, C. V.; Wang, H.; Rus, E.; DiSalvo, F. J.; Abruña, H. D. *J. Am. Chem. Soc.* **2010**, *132*, 10218-10220.

(6) Niedrach, L. W.; Weinstoc.Ib *Electrochemical Technology* **1965**, *3*, 270-&.

(7) Niedrach, L. W.; Zeliger, H. I. *J. Electrochem. Soc.* **1969**, *116*, 152-153.

(8) Pereira, L. G. S.; dos Santos, F. R.; Pereira, M. E.; Paganin, V. A.; Ticianelli, E. A. *Electrochim. Acta* **2006**, *51*, 4061-4066.

(9) Micoud, F.; Maillard, F.; Gourgaud, A.; Chatenet, M. *Electrochem. Commun.* **2009**, *11*, 651-654.

(10) Grgur, B. N.; Markovic, N. M.; Ross, P. N. *J. Phys. Chem. B* **1998**, *102*, 2494-2501.

(11) Ioroi, T.; Fujiwara, N.; Siroma, Z.; Yasuda, K.; Miyazaki, Y. *Electrochem. Commun.* **2002**, *4*, 442-446.

(12) Ioroi, T.; Yasuda, K.; Siroma, Z.; Fujiwara, N.; Miyazaki, Y. *J. Electrochem. Soc.* **2003**, *150*, A1225-A1230.

(13) Nagel, T.; Bogolowski, N.; Samjeske, G.; Baltruschat, H. *J. Solid State Electrochem.* **2003**, *7*, 614-618.

(14) Samjeské, G.; Wang, H.; Löffler, T.; Baltruschat, H. *Electrochim. Acta* **2002**, *47*, 3681-3692.

(15) Subbaraman, R.; Strmcnik, D.; Stamenkovic, V.; Markovic, N. M. *J. Phys. Chem. C* **2010**, *114*, 8414-8422.

(16) Kolb, D. M.; Przasnyski, M.; Gerischer, H. *Journal of Electroanalytical Chemistry and Interfacial Electrochemistry* **1974**, *54*, 25-38.

(17) Trasatti, S. *Journal of Electroanalytical Chemistry and Interfacial Electrochemistry* **1971**, *33*, 351-378.

(18) Obradovic, M. D.; Babic, B. M.; Kowal, A.; Panic, V. V.; Gojkovic, S. L. J. *J. Serb. Chem. Soc.* **2008**, *73*, 1197-1209.

(19) Timofeeva, E. V.; Tsirlina, G. A.; Petrii, O. A. *Russian Journal of Electrochemistry* **2003**, *39*, 716-726.

(20) Clavilier, J.; Feliu, J. M.; Aldaz, A. *J. Electroanal. Chem.* **1988**, *243*, 419-433.

(21) López-Cudero, A.; Cuesta, A.; Gutiérrez, C. *J. Electroanal. Chem.* **2005**, *579*, 1-12.

(22) López-Cudero, A.; Cuesta, Á.; Gutiérrez, C. *J. Electroanal. Chem.* **2006**, *586*, 204-216.

(23) Cuesta, A.; Couto, A.; Rincón, A.; Pérez, M. C.; López-Cudero, A.; Gutiérrez, C. *J. Electroanal. Chem.* **2006**, *586*, 184-195.

(24) Piela, P.; Eickes, C.; Brosha, E.; Garzon, F.; Zelenay, P. *J. Electrochem. Soc.* **2004**, *151*, A2053-A2059.

(25) Wang, Z.-B.; Rivera, H.; Wang, X.-P.; Zhang, H.-X.; Feng, P.-X.; Lewis, E. A.; Smotkin, E. S. *J. Power Sources* **2008**, *177*, 386-392.

(26) Chen, S.; Gasteiger, H. A.; Hayakawa, K.; Tada, T.; Shao-Horn, Y. *J. Electrochem. Soc.* **2010**, *157*, A82-A97.

CHAPTER 7

Electrocatalysis in Alkaline Conditions and Preliminary Testing Results for an Alkaline Anion Exchange Membrane Fuel Cell

7.1 INTRODUCTION

Some of the early work towards developing practical fuel cells was done by Francis T. Bacon in the 1930's to the 1950's. The cells he developed utilized an alkaline electrolyte, aqueous potassium hydroxide. They operated at high pressures and temperatures, and utilized nickel catalysts for both the anode and cathode. Bacon's alkaline fuel cells began receiving attention for use in the U.S. space program in the late 1950's,[1] and adaptations of his work were used for the Apollo program and in the space shuttle.[2] These devices required extremely high purity H_2 and O_2, as the presence of CO_2, CO, or organics would lead to the formation of K_2CO_3, which could precipitate and clog passages in the cell, resulting in performance degradation.

Interest in alkaline fuel cells diminished somewhat since their development for the space program, but there has been a recent resurgence, mainly due to the development of alkaline anion exchange membrane (AAEM) materials. These consist of cationic groups covalently tethered to a polymer backbone. As the cations are not free in solution, precipitation of solid carbonates is not a problem in these cells. From an electrocatalysis standpoint, alkaline conditions offer several advantages over acidic conditions. The reduction of O_2 at less costly materials, such as Ag, becomes more facile. The electrooxdation kinetics of small organic molecules are also improved. Also notable is the improved CO tolerance of Pt under alkaline conditions.

Herein, some of the benefits of alkaline conditions for electrocatalysis are briefly reviewed. Preliminary results of testing an alkaline anion exchange membrane fuel cell are also presented.

7.2 ELECTROCATALYSIS IN ALKALINE CONDITIONS

For electrochemical reactions involving the transfer of an equal number of protons and electrons, the reaction potential is expected to shift negative by an increment of $\ln[10]\cdot\frac{RT}{F}$, or 59 mV, at T = 298 K, per unit increase in pH. The oxygen reduction reaction (ORR), and the oxidation of methanol and other small organic molecules, carbon monoxide, and hydrogen are expected to shift in this manner. This might not seem to be particularly useful, since it would shift the reactions at both the fuel cell anode and cathode to the same extent on the potential axis. The situation is more complicated than this, however, as some electrochemical reactions show improved kinetics at higher pH values. It can also enable the use of materials which would not be stable at lower pH values.

7.2.1 Oxygen Reduction Reaction (ORR)

It is often stated that the kinetics of the ORR are better in alkaline conditions. In the case of Pt, there is some debate over whether this is true, as specific anion adsorption may make the results in acid worse.[3] In the alkaline fuel cells NASA utilized in the space shuttle, an AuPt (9:1) alloy was used for the cathode.[4] The ORR activity of Ag improves significantly at higher pH. It was recently shown that the onset of ORR at Ag (111) shifted positive by about 450 mV going from acid to alkaline conditions, and the production of H_2O_2 decreased markedly.[5] Nickel can carry out the ORR in base at room temperature, though the onset is about +0.5 V vs RHE in the positive going sweep, and there is significant hysteresis on potential cycling due to the irreversibility of the surface oxide formation process.[6] Other, more unusual, materials have also been considered for ORR catalysis in base, such as pyrochlores[7] and perovskites.[8] Complexes of Ni and Co with nitrogen – containing ligands have also been shown to have ORR activity in alkaline media.[9-11]

7.2.2 Small Organic Molecule Oxidation

It has been shown that the electrooxidation of some small organic molecules proceeds at a higher rate under alkaline conditions. In base, the oxidation of methanol at Pt proceeds at higher current densities and with less poisoning.[12] Formaldehyde is also oxidized more rapidly, and has even been shown to reach mass transport limited oxidation currents at Au and a PtAu catalyst.[13,14] Interestingly, though, formic acid/formate electrooxidation becomes slower at Pt at high pH values.[15]

It is not entirely clear that it will be possible to utilize SOM fuels without adding KOH to the fuel feed stream. In a recent review of alkaline DAFC's, NaOH or KOH was added to the fuel feed stream in nearly all cases, and those in which none was added generally showed much lower performance.[16] Without base added to the feed stream, the CO_2 produced by electrooxidation of an organic species will rapidly replace the OH^- in the membrane with CO_3^{2-}. While this is not expected to lead to a precipitation problem as in the original liquid electrolyte fuel cells, it generates other problems. It decreases the pH at the anode, which increases the anode potential (vs. a pH invariant reference) while possibly not shifting the cathode to the same degree, and thus lowering the cell voltage. Other problems might be expected from fuels which can produce relatively unreactive carboxylates, such as acetate from ethanol or formate from methanol, which might also be expected to replace the OH^- in the membrane.

7.2.3 CO Tolerance

Nickel was used for H_2 oxidation in Bacon's alkaline cells, but at high temperature and pressure. At room temperature and atmospheric pressure, however, Ni has relatively low activity for H_2 oxidation.[17] The electrooxidation kinetics of H_2 at Pt actually become slower at high pH values,[18] but the benefit for anode catalysis under alkaline conditions lies in improved CO

tolerance. There have been comparative studies of CO oxidation at Pt at low and high pH values,[19,20] showing that for CO bulk oxidation, with the CO adlayer formed in the higher potential range, the main oxidation peaks occur at similar potentials, but the onset is significantly more negative in base.

A more instructive measure of CO tolerance, than CO bulk oxidation or stripping, is the oxidation of H_2 in the presence of CO. These data are available in the literature for acidic conditions,[21] but to our knowledge, this measurement has not been reported for alkaline conditions. Figure 7.1 shows the cyclic voltammograms of a smooth polycrystalline Pt electrode in 0.1 M H_2SO_4 and 0.1 M KOH solutions, respectively, bubbled with H_2 with 2% CO. There is a negative shift of about 350 mV when switching from acid to base, which is quite large considering the fuel cell open circuit voltage might only be 1 V to begin with.

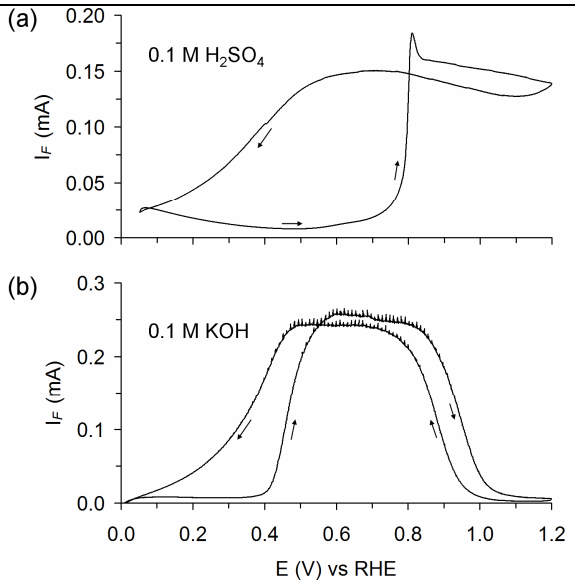

Figure 7.1 : A comparison of cyclic voltammograms of a Pt disk (6 mm) collected in 0.1 M H_2SO_4 (a) and 0.1 M KOH (b) solutions bubbled with H_2 with 2% CO. In both cases, the second cycle is shown. The measurements were done in the DEMS flow cell at flow rate of about 15 µL/s. Scan rate: 10 mV/s, 21°C

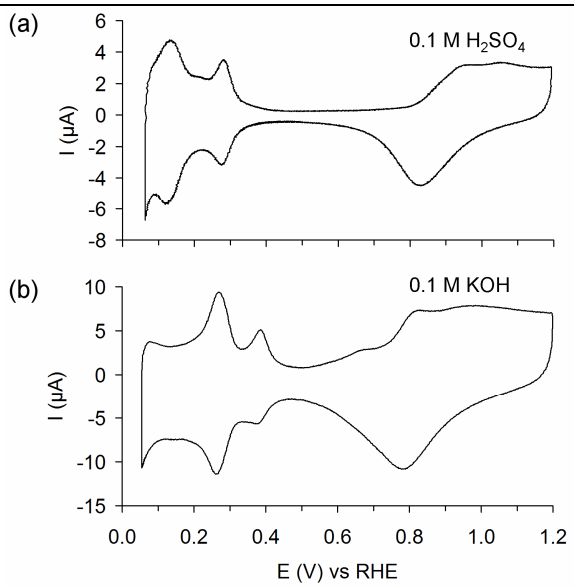

Figure 7.2 : Cyclic voltammograms of a Pt disk (6 mm) in 0.1 M H_2SO_4 (a) and 0.1 M KOH (b). Scan rates: 10 mV/s and 20 mV/s

The negative shift in CO oxidation potential is likely due to the adsorption of oxide species at lower potentials in alkaline solutions. The adsorbing species may be OH^- or another oxygen species which forms from OH^-. For comparison, cyclic voltammograms of polycrystalline Pt in 0.1 M H_2SO_4 and 0.1 M KOH purged with Ar are also shown (figure 7.2). The onset of surface oxide formation is shifted negative by about 70 mV in alkaline solution. The larger current in the double layer range in alkaline solution (relative to the hydrogen adsorption peaks) may, at least in part, arise from some surface oxide formation in this range. This is significantly more negative than in acid solution and would be consistent with the more negative onset of oxidation current in the H_2/CO bubbled solution.

It is also interesting to note that Au also becomes significantly better at oxidizing CO at high pH values, showing a negative shift of about 500 mV in the onset of electrooxidation when changing from 0.1 M $HClO_4$ to 0.1 M NaOH. The onset of CO oxidation occurs at about +0.1 V vs RHE at Au in base, though it appears that this may shift positive with time due to a poisoning process.[22] While Au itself is not a good catalyst for H_2 oxidation, it might be considered as a scrubber to remove CO from the H_2 feed stream.

7.2.4 Alternative Fuels

Alkaline conditions also make the use of alternative fuels such as borohydride possible.[23] Hydrazine is another possible alternative fuel, which shows improved electrooxidation kinetics in base.[24] These fuels have the benefit of more facile electrooxidation kinetics than methanol. They also offer advantages over H_2 in terms of being stored as condensed phases, and having higher solubility in water. These fuels do not have CO_2 as an electrooxidation product, meaning the membrane will not become carbonated. In the case of borohydride, the electrooxidation products may be borate species, which might also exchange with hydroxide in the membrane.

7.3 FUEL CELL TESTING

7.3.1 *Methodology*

For all MEAs, the ionomer shown in figure 7.3.b was dissolved at 0.7% weight in a 77% vol. of n-propanol in water mixture to form an ink. For the catalyst, Pt black or Pt/C 50 wt. % from ETek, were used for both electrodes at a nominal loading of 1 mg/cm^2. The actual loadings were likely less than 0.5 mg/cm^2 due to a large loss factor, arising from the poor dispersion of the catalyst in the ink. The membranes used were 30 µm thick. The GDL used was ELAT LT-1400-W from ETek, and gaskets were fabricated from 0.254 mm Teflon sheets. A 5 cm^2 serpentine flow field was used for the tests shown here, though some tests were also carried out using a 1.6 cm^2 flow field. The cell temperature was set at 50^o C, with the anode and cathode humidifiers both at 55^o C to maintain 100% relative humidity. Pure H_2 and O_2, both at a flow rate of 50 sccm, were used.

7.3.2 Fuel Cell Testing Results

The Coates group has developed several alkaline membrane materials based upon a polyethylene backbone with tetraalkyl ammonium cation groups.[25-27] The cation groups lack β – hydrogens so as to avoid degradation by Hoffman elimination. Several other cationic groups have been considered for AAEMs, and these were recently reviewed.[28]

We studied two membrane materials, one cross – linked and the other non cross – linked. The synthesis and physical properties of these materials are described in detail elsewhere.[26,27] The structures of these polymers are shown in figure 7.3. The non cross – linked polymer has the benefit that it can be dissolved in low molecular weight alcohols, which allows it to be used to prepare ionomer inks for the catalyst layer.

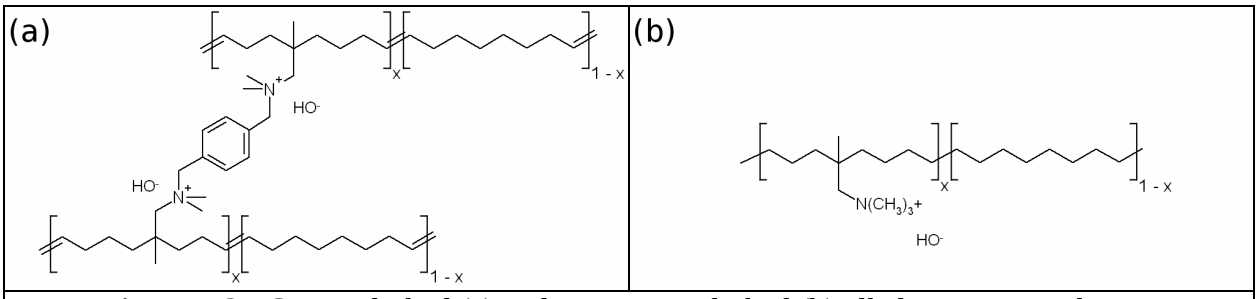

Figure 7.3: Cross – linked (a) and non cross – linked (b) alkaline anion exchange membrane materials. For (a), x = 0.4. For (b), x = 0.29 for the membrane material and 0.21 for the ionomer ink material.

In initial attempts, the hot pressing method of MEA preparation was used. The catalyst ionomer ink was applied to the GDLs, and these were pressed into the membrane at approximately 60^{o} C with a hydraulic press. When problems with punctured membranes were encountered, the catalyst coated membrane (CCI) method was attempted. In this case, difficulties were encountered with excessive swelling of the membrane, and with agglomeration of the catalyst around the edges of the area being painted. As successive layers were added to the coating, the ink broke up the previously applied layers and redeposited the catalyst around the edges.

In both methods, it was apparent that the membrane was degrading from the amine odor given off. Though the Hoffman elimination degradation mechanism is blocked for the quaternary ammonium groups in this material, degradation is still possible. In a study with trimethylammonium hydroxide, as a model compound, it was found that the methyl groups would undergo nucleophilic attack by hydroxide and methoxide at elevated temperatures and decreased water content. A second pathway proceeding through an ylide, formed by deprotonation of a methyl group, was also proposed.[29]

In our early testing attempts, the membrane had been soaked in KOH solution prior to preparation of the MEA. This subjected the membrane to heat and dehydration, which are favorable conditions for degradation. In later work, we found that it was possible to keep the

membrane in the carbonate form during assembly. Carbonate is less nucleophilic than hydroxide, so degradation was not as much of an issue under these conditions.

In the initial cell polarization of a membrane in the carbonate form, a large increase in current was observed between the decreasing and increasing voltage sweeps. This was attributed to *in situ* exchange of hydroxide with carbonate. This exchange has previously been noted for other anion exchange membranes.[30]

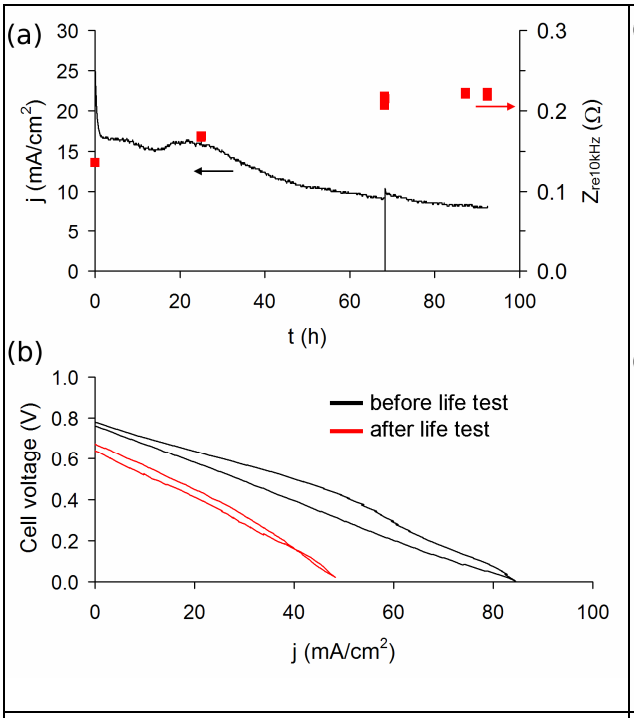

Figure 7.4 : Long term performance test of a cell with a cross – linked membrane at 0.52 V (a), and voltage polarization curves from before and after the long term test (b).

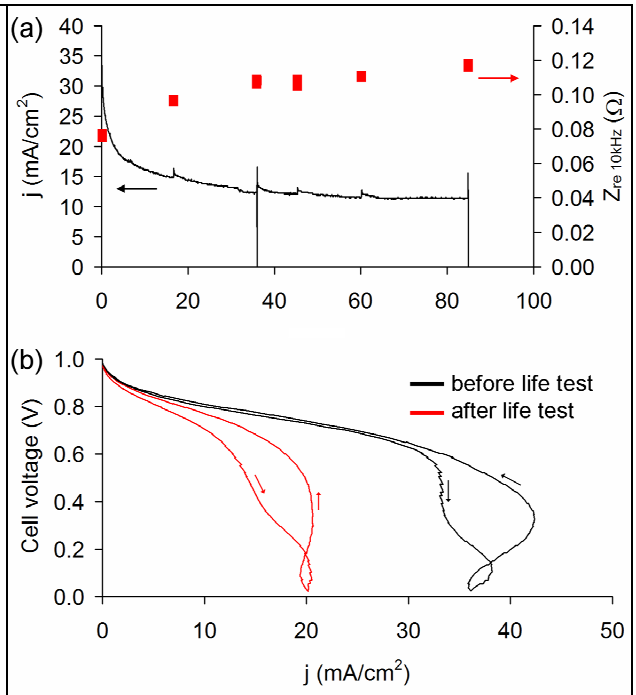

Figure 7.5 : Long term performance test of a cell with a non – cross linked membrane 0.52 V (a), and voltage polarization curves collected before and after the long term test (b).

Long term performance and controlled voltage polarization curves for fuel cells prepared with the two membrane materials are shown in figures 7.4 and 7.5, respectively. There was significant variability in cell performance, due to the difficulties in MEA preparation. These tests were not the best in terms of current and power densities achieved, but they were some of

the best in terms of longer term stability. For both materials, a decrease in current and an increase in the high frequency real impedance over time were observed. There was a sharp initial drop in the current, followed by a more gradual decline. The decreasing current and increasing resistance are suggestive of loss of ionic conductivity in the membrane material. These changes might also arise from physical degradation of the catalyst – ionomer layer, possibly from swelling upon water uptake.

In the case of the cross – linked membrane, the open circuit voltage (OCV) was low from the outset, and decreased further during the testing. The low OCV is indicative of permeation of reactants through the membrane, leading to mixed potentials at the two electrodes. The increase over time could arise from the formation of pin holes.

The non cross – linked membrane showed little change in the OCV over time. The polarization curves for this cell showed what appeared to be a mass transport limited current plateau at low cell voltages, though with some hysteresis. The current density of the plateau was much lower than that observed for cells prepared with Nafion, possibly due to agglomeration of the catalyst in the alkaline membrane cell. The hysteresis between the decreasing and increasing voltage sweeps is suggestive of removal of an adsorbed poison at low cell voltages, though it is not clear what the identity of the poison would be. The current of the transport limited plateau decreased over time, suggesting a loss of active surface area, possibly through increasing agglomeration or delamination of the catalyst layer.

7.4 CONCLUSIONS

Alkaline conditions appear to offer several advantages in terms of electrocatalysis, both in terms of improving existing catalysts, and making alternative, less costly, catalysts feasible. Initial testing was carried out in fuels using alkaline anion exchange membranes, and operational

cells were obtained using both cross – linked and non cross – linked membrane mateials. Though the performance was low, and there was degradation over time, the cells remained functional for several days. Better performance will likely be obtained with improvements in the MEA preparation protocol, particularly in the formulation of the catalyst – ionomer ink.

7.5 REFERENCES

(1) Bacon, F. T. *J. Electrochem. Soc.* **1979**, *126*, 7C-17C.

(2) Srinivasan, S. *Fuel cells: from fundamentals to applications*; Springer: New York, NY, 2006.

(3) Spendelow, J. S.; Wieckowski, A. *Phys. Chem. Chem. Phys.* **2007**, *9*, 2654-2675.

(4) Blomen, L. J. M. J.; Mugerwa, M. N. *Fuel cell systems*; Plenum Press: New York, 1993.

(5) Blizanac, B. B.; Ross, P. N.; Markovic, N. M. *Electrochim. Acta* **2007**, *52*, 2264-2271.

(6) Shumilova, N. A.; Bagotzky, V. S. *Electrochim. Acta* **1968**, *13*, 285-293.

(7) Goodenough, J. B.; Manoharan, R.; Paranthaman, M. *J. Am. Chem. Soc.* **1990**, *112*, 2076-2082.

(8) Suntivich, J.; Gasteiger, H. A.; Yabuuchi, N.; Nakanishi, H.; Goodenough, J. B.; Shao-Horn, Y. *Nat Chem* **2011**, *3*, 546-550.

(9) Jasinski, R. *Nature* **1964**, *201*, 1212-1213.

(10) Hurrell, H. C.; Mogstad, A. L.; Usifer, D. A.; Potts, K. T.; Abruna, H. D. *Inorg. Chem.* **1989**, *28*, 1080-1084.

(11) Goubert-Renaudin, S. N. S.; Wieckowski, A. *J. Electroanal. Chem.* **2011**, *652*, 44-51.

(12) Cohen, J. L.; Volpe, D. J.; Abruña, H. D. *Phys. Chem. Chem. Phys.* **2007**, *9*, 49-77.

(13) Beltowska-Brzezinska, M. *Electrochim. Acta* **1985**, *30*, 1193-1198.

(14) Beltowska-Brzezinska, M.; Heitbaum, J. *Journal of Electroanalytical Chemistry and Interfacial Electrochemistry* **1985**, *183*, 167-181.

(15) John, J.; Abruña, H. D. **in preparation**.

(16) Antolini, E.; Gonzalez, E. R. *J. Power Sources* **2010**, *195*, 3431-3450.

(17) Floner, D.; Lamy, C.; Leger, J. M. *Surf. Sci.* **1990**, *234*, 87-97.

(18) Sheng, W.; Gasteiger, H. A.; Shao-Horn, Y. *J. Electrochem. Soc.* **2010**, *157*, B1529-B1536.

(19) Kita, H.; Shimazu, K.; Kunimatsu, K. *Journal of Electroanalytical Chemistry and Interfacial Electrochemistry* **1988**, *241*, 163-179.

(20) Couto, A.; Rincón, A.; Pérez, M. C.; Gutiérrez, C. *Electrochim. Acta* **2001**, *46*, 1285-1296.

(21) Gasteiger, H. A.; Markovic, N. M.; Ross, P. N. *J. Phys. Chem.* **1995**, *99*, 16757-16767.

(22) Kita, H.; Nakajima, H.; Hayashi, K. *Journal of Electroanalytical Chemistry and Interfacial Electrochemistry* **1985**, *190*, 141-156.

(23) Finkelstein, D. A.; Mota, N. D.; Cohen, J. L.; Abruña, H. D. *J. Phys. Chem. C* **2009**, *113*, 19700-19712.

(24) Burke, L. D.; Healy, J. F.; O'Dwyer, K. J.; O'Leary, W. A. *J. Electrochem. Soc.* **1989**, *136*, 1015-21.

(25) Clark, T. J.; Robertson, N. J.; Kostalik IV, H. A.; Lobkovsky, E. B.; Mutolo, P. F.; Abruña, H. D.; Coates, G. W. *J. Am. Chem. Soc.* **2009**, *131*, 12888-12889.

(26) Robertson, N. J.; Kostalik, H. A.; Clark, T. J.; Mutolo, P. F.; Abruña, H. D.; Coates, G. W. *J. Am. Chem. Soc.* **2010**, *132*, 3400-3404.

(27) Kostalik, H. A.; Clark, T. J.; Robertson, N. J.; Mutolo, P. F.; Longo, J. M.; Abruña, H. D.; Coates, G. W. *Macromolecules* **2010**, *43*, 7147-7150.

(28) Merle, G.; Wessling, M.; Nijmeijer, K. *J. Membr. Sci.* **2011**, *In Press, Corrected Proof*.

(29) Macomber, C. S.; Boncella, J. M.; Pivovar, B. S.; Rau, J. A. *Journal of Thermal Analysis & Calorimetry* **2008**, *93*, 225-229.

(30) Adams, L. A.; Poynton, S. D.; Tamain, C.; Slade, R. C. T.; Varcoe, J. R. *ChemSusChem* **2008**, *1*, 79-81.

APPENDIX

Data Acquisition and SDEMS LabVIEW Software

1. DATA ACQUISITION

To record data from cyclic voltammetry, a LabVIEW (version 8.2) program was read two analog inputs of a National Instruments data acquisition card and display the data on an XY plot, as well as write it to a text file. This program was adapted from the example program "Cont Acq&Graph Voltage" provided with LabVIEW. There are also inputs on the front panel which allow the user to specify the acquisition rate, the DAQ inputs to be used, and the configuration of these inputs. Generally this will be referenced single ended (RSE), though differential inputs can also be used, and is preferable in terms of improved S/N ratio. There also fields with which the range of the analog inputs can be specified, which affects the voltage resolution of the inputs. Though arbitrary numbers can be entered for the ranges, the NI cards actually have incrememental ranges, generally ±10, ±5, ±2.5, ±1, ±0.5 V, and ±0.05 V or 10 - 0, 5 - 0 V, etc., and these are specified in the board manuals. There is also a control labeled "E x -1," which multiplies the X axis by -1, which is useful since some potentiostats in the lab utilize the potential convention in which the sign is reversed. The record button allows the user to chose whether the data will be written to file or not, and will record to file by default. The reset button will clear the plot when pressed.

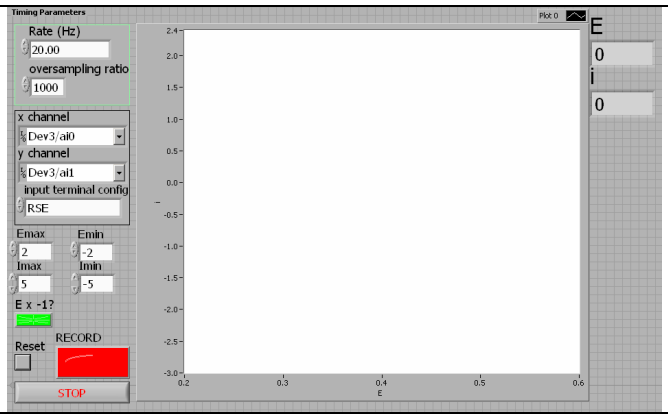

Figure 1: Front panel of the program "XY_rec.vi"

In addition to acquiring and recording data, the program also utilizes an on the fly median filter to improve the signal to noise ratio. Data are acquired at a multiple for the specified poling rate, controlled by the user input "oversampling ratio" on the front panel, and the median of the points is taken. This processed data are written to the file and displayed on the screen. Additionally, the unfiltered data is also written to the file. The program contains one sub – vi which writes header information to the data file, including the time and the rate of acquisition. In cases of excessive noise, a low pass RC filter (hardware) was placed at the analog outputs of the potentiostat.

The block diagram of the program is annotated for users wishing to modify it, but we will describe it briefly here. It makes use of the DAQmx subroutines provided with LabVIEW. First, the program will prompt the user for a file name and directory, and then create the file to accept the data. The analog inputs are configured, then the sampling clock is configured, and finally the card is primed to begin recording. The program then enters a while loop which will poll the card for data at the user specified rate, plot it and write it to file until the user presses the stop button on the front panel. After the loop is exited, the data file is closed and the data acquisition task deleted from the card.

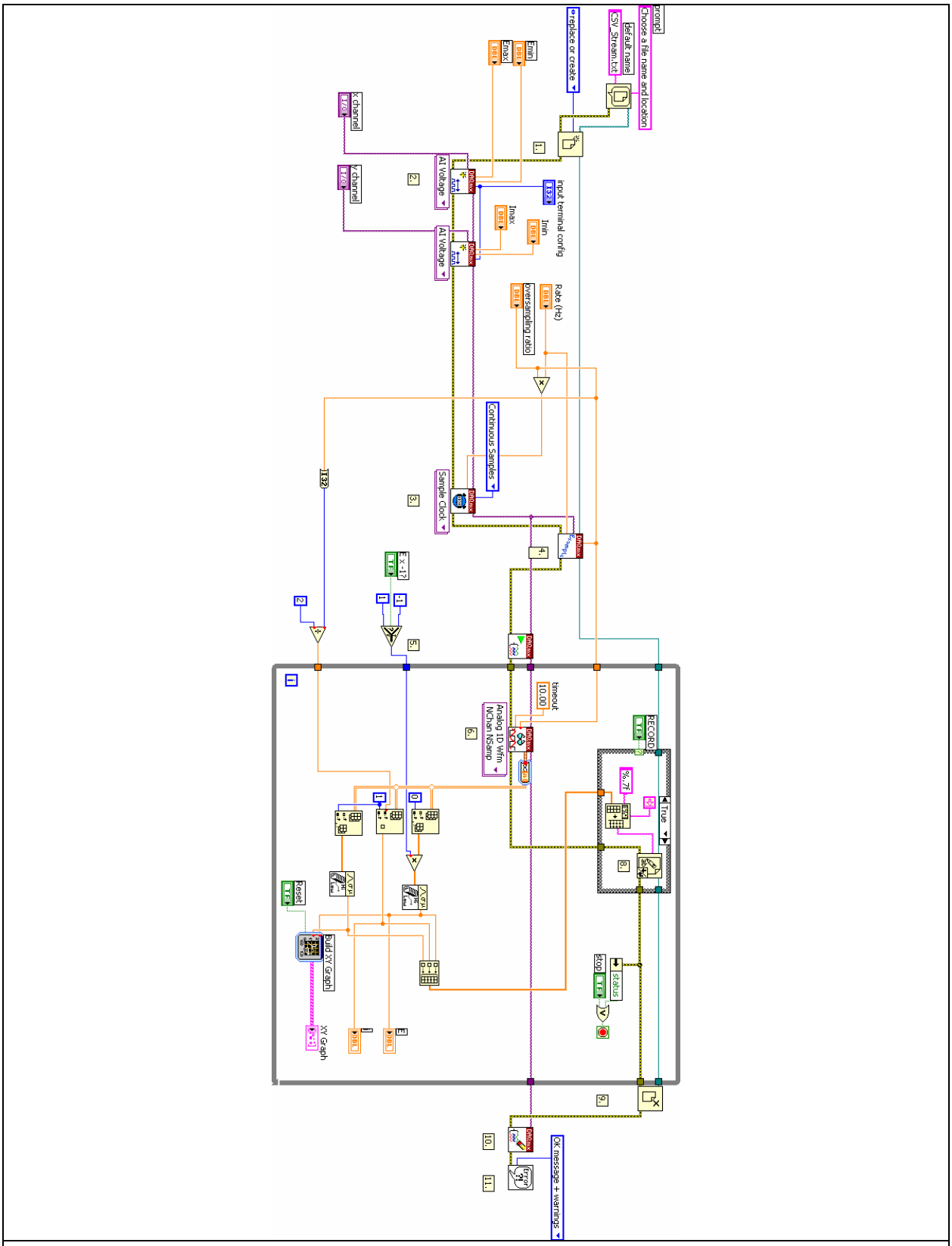

Figure 2: Block diagram of the program “XY_rec.vi”

Versions of this program with additional analog inputs were also written for use with rotating ring disk electrode setups and the DEMS. This program would also be applicable to other applications in which recording of additional voltage signals beyond current and potential was desired, such as from a thermocouple. The voltage signal from the analog outputs of the Pfeiffer Vacuum mass spectrometers were not directly proportional to the mass spectrometric signal, but rather transformed to a logarithmic scale. The analog output signals varied between 0 and 10 V, are related to the mass spectrometric currents as:

$$i = A \cdot 10^{N(\frac{V_o}{10}-1)}$$

The value V_o is the analog output signal from the mass spectrometer. The values N and A correspond to the parameters LOGND and AO Range, resepectively, set in the MID mode of Quadera, the mass spectrometer control software from Pfeiffer. In earlier versions of Quadera, the AO Range is fixed at 10^{-5}. A sub – vi is employed to convert V_o to the unscaled mass spectrometric current on the fly.

2. SCANNING DEMS SOFTWARE

The software written for the SDEMS performs the tasks of directing the motion of the XY translation table and recording a voltage signal at the appropriate times. The software interfaces with two different components: the VXM-2 stepper motor controller, and the PCI-MIO-16E-1 NI data acquisition card. The latter is used to record the analog output signal from the mass spectrometer or to a potentiostat. The VXM-2 and NI DAQ are also connected to each other: one of the digital outputs of the former is connected to the PFI0 digital input of the latter for purposes of triggering data acquisition. The mass spectrometer is controlled and configured using the Quadera software provided by Pfeiffer Vacuum.

The front panel of the program has inputs which allows the user to input parameters for the raster scan of the instrument, including displacement, velocity and increment between the rows scanned. It also calculates the time required to complete the scan to avoid impractically long measurements. Once the user has entered this information, the "OK" button should be pressed, and there will be a prompt for a file path and name. The data points are displayed in a 3D plot in the front panel, as well as in a plot vs. time below it. There is an emergency stop button on the right hand side of the screen, which will allow the user to stop the scan in the event of an error or accident. There is also a control on the front panel which allows the user to control the scaling of the input data, as is needed for the mass spectrometric data. There is also an option to not transform the data, when the instrument was being used for SECM measurements.

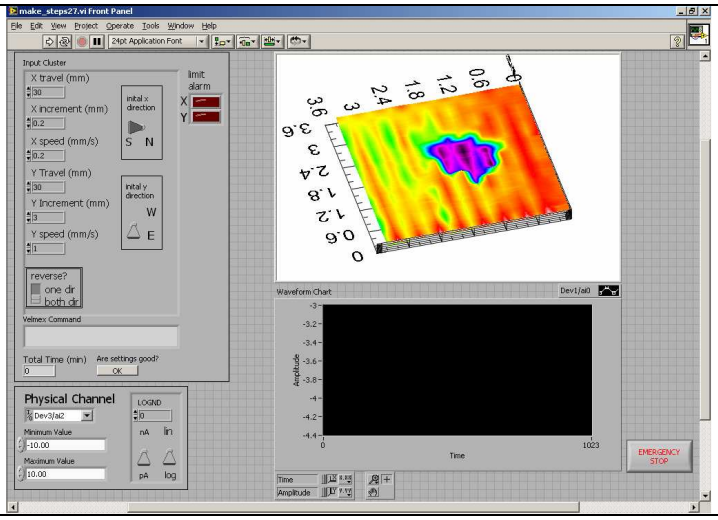

Figure 3: Front panel of the SDEMS – SECM program.

The separate steps of the program are contained in a sequence structure, which controls the timing of major sections of the program. The block diagram is annotated, but the parts will be described briefly here. In frame (1) (see figure 4), global variables associated with the emergency stop button are reset. In frame (2) stepper motor controller (VXM-2) is then polled for the motor positions, so that the user will be warned as to whether the motors will reach the limits of the lead screws during the scan. Each time the VXM-2 is restarted, it will refer to its

initial position as the zero point, even though it may not be. Prior to starting measurements, the motor positions should be centered, and the VXM-2 then restarted so that motor positions are calculated with respect to the centers of the lead screws.

In frame (3), the program reads the user input parameters for the scan and calculates the time required to complete the scan. The inputs are in a loop, so the user can modify the settings until they are satisfactory. The scan parameters are also translated to a command string for the VXM-2, instructing it to move in a raster pattern, giving a high signal on one of the digital outputs of the controller before beginning. Also included in the command is a 5 s pause before the scanning begins. This was needed to prevent the first trigger signal from being given before DAQmx began listening for it. Frame (3) also configures the analog input parameters, data acquisition parameters and the analog trigger. In frame (4), the header information and scan parameters are written to the file.

In frame (5), an array is generated to contain the data, the connection with the VXM-2 is established, the commands sent to it, and the scan initiated. The collection of data with the DAQmx read vi is initiated by a trigger signal from the VXM-2 to the PFI0 digital input of the NI DAQ. Data collection is initiated at the beginning of each row in this way. After completion of a row, the data is scaled, displayed on the front panel, entered in the array, and written to the file. The elapsed time is also recorded at the end of each row for trouble shooting purposes. Also contained in this frame is a user event that will send the stop command to the VXM-2 if the user presses the emergency stop button on the front panel. After scanning is completed, the DAQmx task is erased.

In frame (6), the elapsed time data is written to file and the XYZ array is written to file. The Z data is actually written to the file twice: once as rows during the scan, without

corresponding XY values, and once after the scan in columns, with XY values. This is done to ensure that the data is saved, even if something goes wrong with the program before it completes scanning. Finally, the file is closed in frame (7). The program contains several sub routines, which have been listed with brief descriptions in table 1.

Table 1: Sections of the block diagram, shown in figures 4 and 5.

section	purpose
(1)	reset global variables
(2)	get motor positions
(3)	scan parameters set, input parameters formatted for VXM-2, analog inputs initialized
(4)	prompt user for file name and path, create file, write scan parameters to file
(5)	XYZ array to contain data generated, connection with VXM-2, initialized, command sent to VXM-2, scan initiated, data acquired and displayed on front panel, unformatted data written to file
(6)	timing data written to file, formatted data written to file
(7)	file closed

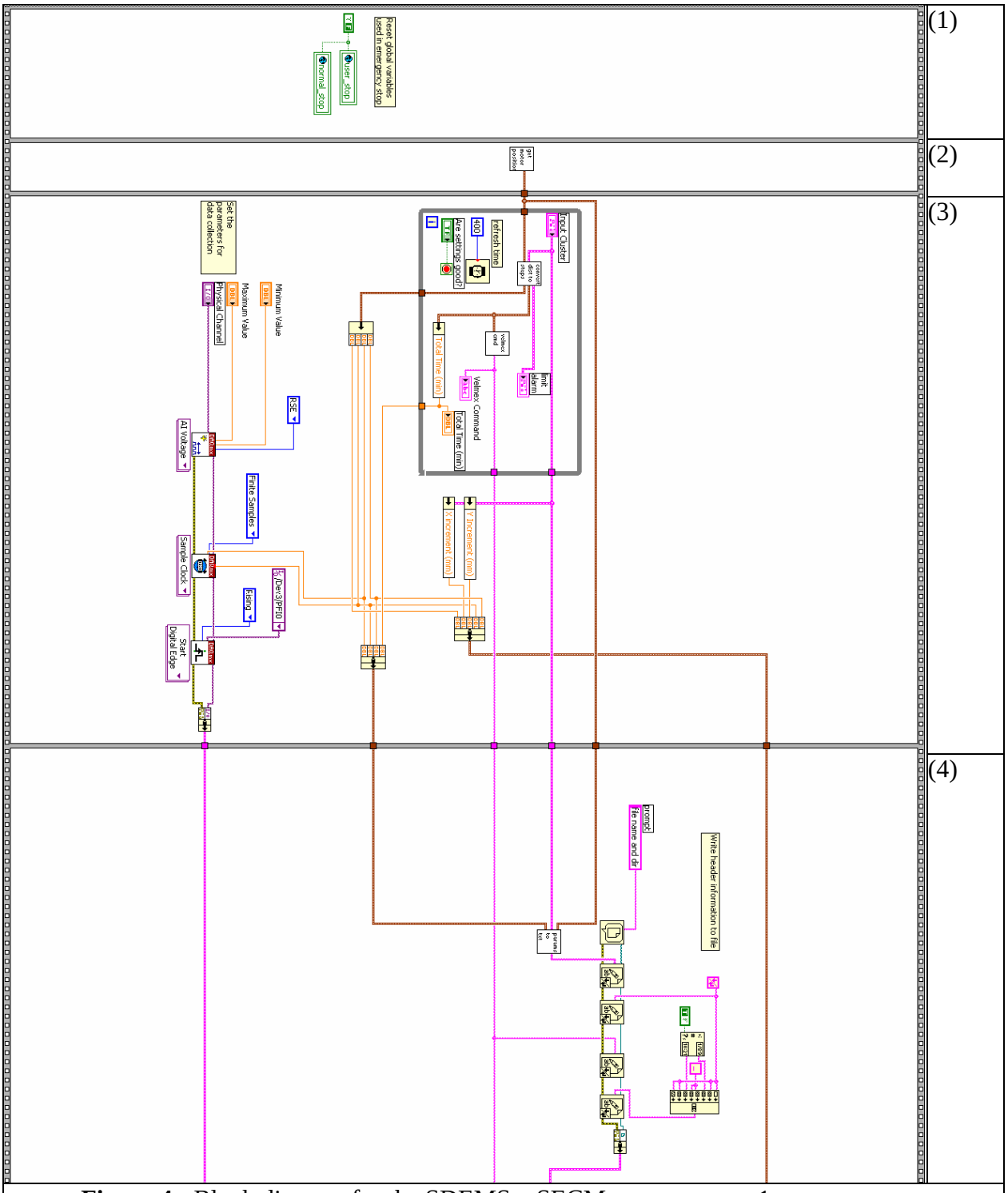

Figure 4: Block diagram for the SDEMS – SECM program, part 1.

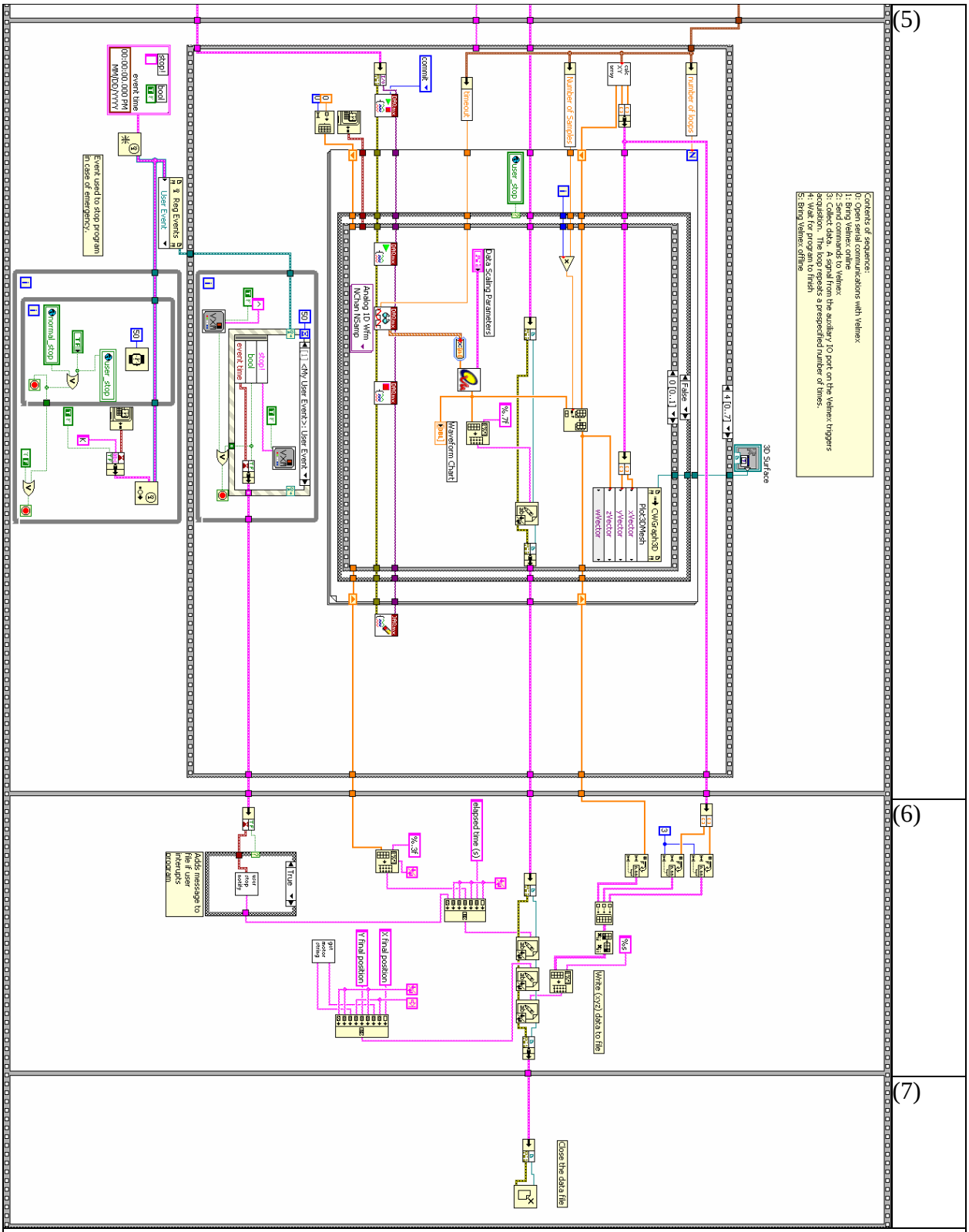

Figure 5: Block diagram for the SDEMS – SECM program, part 2.

Table 2: Sub – vi's (subroutines) in the SDEMS program, and descriptions.		
vi name	icon	description
get_motor_positions.vi		Connects to VXM-2, reads the motor positions, and outputs them
calc_steps5.vi		Converts the user – entered scan parameters from millimeters to steps (1 mm = 400 steps)
to_vlmx.vi		Converts scan parameters into code string for the VXM-2
parameters_to_text2.vi		Formats the scan parameters into text to be written to the data file
calc_xy3.vi		Generates an array of XYZ values based upon the scan – parameters. The Z values are initially set to 0, but are overwritten as the data is entered.
convert_quadera_linear_option.vi		Converts mass spectrometric data from logarithmic scale to linear scale, and puts it in units of nA or pA. In the case that the SECM tip is used, the linear option is used, and data is not transformed.
user_stop_file_notify.vi		If the user activates the emergency stop, this sub-vi generates text to write to the file, indicating the stop and the time.
Vxmdriverlv8.vi		Driver for the VXM-2 from Velmex.
stop_global.vi		Global variable containing "user_stop" and "normal_stop," with the former indicating the user has hit the emergency stop and the latter that the scanning has stopped as planned. These are needed to stop the data acquisition loop if requested by the user, and to stop the emergency stop loop when the scanning ends as planned.

3. SECONDARY VELMEX PROGRAMS

Two other LabVIEW programs were prepared to facilitate use of the XY translation table. One, zero_motor_positions.vi causes the stepper motors to move until the limit switch is reached. The direction is then reversed, and the motor moves until it is at the mid point of the lead screw. This is done for both motors to center them. The VXM-2 should be restarted after this so that the center positions are referred to as 0.

The other program, simple_controler_no_stop.vi provides a user friendly interface for the VXM-2, where displacements and speeds can be entered in terms of millimeters. The program then translates these to command strings for the VXM-2.